Title

Bragg Coherent Diffractive Imaging of Energy Storage and Conversion Materials

Author

Cela, Devin

Publication Date

2019

UNIVERSITY OF CALIFORNIA SAN DIEGO

Bragg Coherent Diffractive Imaging of Energy Storage and Conversion Materials

A dissertation submitted in partial satisfaction of the
requirements for the degree
Doctor of Philosophy

in

Physics

by

Devin Cela

Committee in charge:

Professor Oleg G. Shpyrko, Chair
Professor Richard D. Averitt
Professor David P. Fenning
Professor Zhaowei Liu
Professor Thomas W. Murphy
Professor Tenio Popmintchev

2019

The dissertation of Devin Cela is approved, and it is acceptable in quality and form for publication on microfilm and electronically:

Chair

University of California San Diego

2019

DEDICATION

To my mother.

EPIGRAPH

I try all things, I achieve what I can.

—Herman Melville, Moby-Dick, or, the Whale

TABLE OF CONTENTS

Signature Page iii

Dedication iv

Epigraph v

Table of Contents vi

List of Figures ix

List of Tables xii

Acknowledgements xiii

Vita xiv

Abstract of the Dissertation xv

Chapter 1 Introduction 1
- 1.1 Why use X-rays? 2
- 1.2 Lithium-ion batteries 3
  - 1.2.1 Issues limiting batteries 5
  - 1.2.2 Measurement with Bragg coherent diffractive imaging . . . 6
- 1.3 Perovskite solar cells (PSCs) 7
  - 1.3.1 Functional hybrid materials 7
  - 1.3.2 The growth of hybrid photovoltaics 8
  - 1.3.3 Crystal structure and phases 10
  - 1.3.4 Current challenges 12

Chapter 2 Coherent X-ray scattering theory 16
- 2.1 Fundamentals of lensless imaging 16
  - 2.1.1 Far field imaging 17
  - 2.1.2 The phase problem 18
  - 2.1.3 Resolution and limitations 19
- 2.2 Coherence requirements 20
  - 2.2.1 Temporal coherence 21
  - 2.2.2 Spatial coherence 21
- 2.3 Solving the phase problem with iterative algorithms 22
  - 2.3.1 Error reduction (ER) phase retrieval algorithm 23
  - 2.3.2 Other popular algorithms 25
  - 2.3.3 Shrink wrap 26
  - 2.3.4 Assessing accuracy of reconstructed objects 26

2.4 Understanding strain in coherent diffractive imaging 27

Chapter 3 Long-range displacement field in a lithium-rich layered oxide material $Li_{1.2}Ni_{0.133}Mn_{0.534}Co_{0.133}O_2$ 30
3.1 Abstract 30
3.2 Introduction 31
3.3 *Operando* 3D Imaging of three-fold symmetric displacement field . 32
3.4 Discussion 38
3.5 Acknowledgements 40
3.6 Supplementary Information 40

Chapter 4 Nanoscale differences in strain and defect density as a function of annealing conditions in $LiNi_{0.8}Co_{0.15}Al_{0.05}O_2$ 54
4.1 Abstract 54
4.2 Introduction 55
4.3 Bragg coherent diffractive imaging 56
4.4 Conclusion 61
4.5 Supporting Information 63

Chapter 5 Determining lithium dynamics through ensemble powder diffraction of lithium-ion battery cathodes 72

Chapter 6 Visualizing phase transformations in Li_2RuO_3 (LRO) with ensemble powder diffraction and coherent diffractive imaging 76

Chapter 7 Hybrid perovskite solar cells 80
7.1 Bragg coherent diffractive imaging of Cs-based perovskites 80
  7.1.1 Strain change in perovskite nanocrystals due to voltage . . . 85
  7.1.2 A study of thermal and moisture stability 88
7.2 Time-resolved study of ion dynamics using X-ray photon correlation spectroscopy (XPCS) 92
  7.2.1 Introduction to XPCS 92
  7.2.2 Theoretical justification 96
  7.2.3 Experimental results 99

Appendix A $CH_3NH_3PbBr_3$ hybrid perovskite solar cell synthesis and cell design . . . 104
A.1 Synthesis of CH_3NH_3I 104
A.2 Device Fabrication 105
  A.2.1 Itemized fabrication procedure 106
A.3 Device Characterization 108

Appendix B Proposed inelastic neutron scattering experiment of $CH_3NH_3PbI_3$ with phonon mode simulations 110
B.1 Goal of Experiment 110

B.2 Theoretical justification: Density functional theory (DFT) and density functional perturbation theory (DFPT) of hybrid perovskites 111
  B.2.1 Geometrical relaxation 111
  B.2.2 Phonon calculations using density functional perturbation theory 114
B.3 Vibrational properties of $CH_3NH_3PbI_3$ 115
B.4 Precedent for experiment and expected results 121
B.5 Preparation (before experiment) 122
B.6 Experimental Plan 123
B.7 Questions and Challenges 123

Appendix C General advice for *operando* BCDI measurements of battery cathodes at Sector 34-ID-C of the Advanced Photon Source 125
C.1 Detectors 126
  C.1.1 Software commands to switch to CCD detector 126
  C.1.2 Software commands to switch to Medipix detector 127
  C.1.3 CCD 128
  C.1.4 Medipix 128
C.2 Tips for beamline control 129
C.3 Alignment of the sample rotation axis 129
C.4 Searching for particles 130
C.5 Estimate BCDI scan parameters 131
C.6 *Ex situ* sample mounting 132
C.7 Coin cells 132
  C.7.1 How to mount the coin cell 134
C.8 AMPIX cells 135
  C.8.1 Preparing AMPIX cells 135
  C.8.2 Cleaning AMPIX cells 136
  C.8.3 Sample holder for AMPIX cells: 137
C.9 MACCOR battery cycler 137
C.10 Useful links 138

Bibliography 139

LIST OF FIGURES

Figure 1.1: Shares of global primary energy consumption by fuel 1
Figure 1.2: Moore's Law for computer speed vs. X-ray source brilliance 2
Figure 1.3: Operation of lithium-ion battery 4
Figure 1.4: Ragone plot of energy sources for electric vehicles 4
Figure 1.5: Using the Bragg condition to isolate nanoparticles 6
Figure 1.6: Mayan artwork 7
Figure 1.7: Solar cell efficiencies 9
Figure 1.8: The three hybrid perovskite phases along longest axis. 10
Figure 1.9: The three hybrid perovskite phases along shortest axis. 11
Figure 1.10: Maintaining stable perovskite solar cells 13

Figure 2.1: The phase problem 18
Figure 2.2: Resolution 19
Figure 2.3: Coherent vs. incoherent speckle pattern 20
Figure 2.4: Sketch of generic phase retrieval algorithm 23
Figure 2.5: Sketch of error reduction phase retrieval algorithm 24
Figure 2.6: Schematic of Bragg scattering with labeled displacement field $u(\mathbf{r})$ 27
Figure 2.7: Collecting a rocking curve 29

Figure 3.1: Structure of layered oxide materials 33
Figure 3.2: Symmetry of displacement and strain fields in a pristine lithium-rich particle 35
Figure 3.3: *Operando* cycling 37
Figure 3.4: Understanding the symmetry of the diffraction patterns. 41
Figure 3.5: Confirming long-range displacement field throughout entire particle 42
Figure 3.6: Lack of symmetry of NMC cathode nanoparticles 43
Figure 3.7: Rotational symmetry of Li-rich cathode nanoparticles 43
Figure 3.8: Extracting period of rotation from 2D rotational cross-correlation images . 44
Figure 3.9: Long-range displacement field as a function of charging time 45
Figure 3.10: Three-dimensional view of cycled *in situ* lithium-rich layered oxide nanoparticles 46
Figure 3.11: Changes in surface surface area of measured LRLO particle as a function of lithium concentration during cycling 47
Figure 3.12: Changes in surface strain, symmetry, and dislocation density of measured LRLO particle as a function of lithium concentration during cycling 48
Figure 3.13: *Operando* diffraction data. 49
Figure 3.14: Symmetries of long-range displacement field for nine distinct pristine LRLO crystals 50
Figure 3.15: The increase in strain energy and dislocation density as a function of voltage in LRLO cathode nanoparticles 50
Figure 3.16: Removal of phase wrapping artifacts 51

Figure 3.17: 3D visualization of long-range displacement field in LRLO. Rotating an LRLO crystal to view the displacement field 51
Figure 3.18: 3D visualization of smaller displacement field in CLO. Rotating an NMC333 crystal to view the displacement field 52
Figure 3.19: 2D cross-correlation as a function of rotation angle 52
Figure 3.20: Visualization of using phase offsets to eliminate incorrectly labelled dislocations 53

Figure 4.1: Experimental setup for battery CDI 57
Figure 4.2: Dislocation cores for both anneals 59
Figure 4.3: Reconstruction and strain features for both annealing times 61
Figure 4.4: Microscopy images of 12-hr anneal 64
Figure 4.5: Microscopy images of 24-hr anneal 64
Figure 4.6: Phase retrieval error 65
Figure 4.7: Stability of reconstruction 66
Figure 4.8: Powder X-ray diffraction 67
Figure 4.9: Dislocation density 68
Figure 4.10: Collection of single-particle diffraction patterns and their associated reconstructions 69
Figure 4.11: Resolution of BCDI measurements 70
Figure 4.12: Resolution of BCDI measurements 71

Figure 5.1: Ensemble X-ray diffraction of thin CLO cathode cycled at C/10 73
Figure 5.2: Ensemble X-ray diffraction of thick CLO cathode cycled at C/10 73
Figure 5.3: Ensemble X-ray diffraction of thick CLO cathode cycled at C/3 74
Figure 5.4: Thick cathode Li-ion dynamics 75

Figure 6.1: BCDI reconstruction of Li_2RuO_3 cathode particle 77
Figure 6.2: Ball-milled and sintered Li_2RuO_3 cathode nanoparticles 77
Figure 6.3: Fitting of ensemble powder diffraction of Li_2RuO_3 emphasizing different phases 78
Figure 6.4: Ensemble powder diffraction of Li_2RuO_3 79

Figure 7.1: Tetragonal $CH_3NH_3PbI_3$ 81
Figure 7.2: Optical images of synthesized $CsPbBr_3$ nanocrystals 82
Figure 7.3: SEM of $CsPbBr_3$ in central portion of sample 82
Figure 7.4: SEM of $CsPbBr_3$ near edge of sample 83
Figure 7.5: Reconstructed pristine $CsPbBr_3$ 84
Figure 7.6: Multiple $CsPbBr_3$ crystals show strain at narrow particle edges 85
Figure 7.7: Preliminary characterization of $CsPbBr_3$ 85
Figure 7.8: $CsPbBr_3$ BCDI diffraction patterns and SEM for two different sample preparations 87
Figure 7.9: Temperature-dependent XRD on $CsPbBr_3$ 88
Figure 7.10: $CsPbBr_3$ BCDI diffraction pattern as a function of temperature 89
Figure 7.11: Gas flow cell 90

Figure 7.12: Locating desirable crystals during the experiment 91
Figure 7.13: Distilled water bubbler used for humidity control 91
Figure 7.14: $CsPbBr_3$ BCDI diffraction pattern as a function of humidity level 93
Figure 7.15: $CsPbBr_3$ BCDI stability scans after increasing humidity level 94
Figure 7.16: $CsPbBr_3$ powder diffraction as a function of humidity level 95
Figure 7.17: Hysteresis in hybrid perovskites 95
Figure 7.18: $CsPbI_3$ X-ray speckle pattern 97
Figure 7.19: $CsPbBr_3$ XPCS sample information 100
Figure 7.20: $CsPb_2Br_5$ and $CsPbBr_3$ XPCS sample information 100
Figure 7.21: Preparing perovskite samples for voltage application in XPCS 102
Figure 7.22: X-ray fluorescence linescan of Pt finger electrodes 103
Figure 7.23: Locating perovskite nanocrystals for XPCS 103

Figure A.1: Fabrication procedure for $CH_3NH_3PbI_3$ 105

Figure B.1: Perovskite solar cell architectures used in impedance study 110
Figure B.2: *k*-point and cutoff energy convergence 111
Figure B.3: Free energy of the three relaxed phases 112
Figure B.4: Methylammonium relaxation for orthorhombic phase 113
Figure B.5: DFT simulation performance and scaling 116
Figure B.6: Crystal structure of lead iodide 117
Figure B.7: Simulated phonon bandstructure and density of states of lead iodide 118
Figure B.8: Orthorhombic $CH_3NH_3PbI_3$ atomic phonon density of states 118
Figure B.9: Orthorhombic $CH_3NH_3PbI_3$ phonon density of states, separating the organic and inorganic vibrational components 119
Figure B.10: Inelastic neutron scattering spectrum of hybrid perovskite 119
Figure B.11: SEM of perovskite solar cell layers 120
Figure B.12: SEM of double perovskite solar cell layers 121

Figure C.1: CCD detector 128
Figure C.2: Detector setup at the APS Sector 34-ID-C 130
Figure C.3: Prepared *ex situ* sample 132
Figure C.4: Mounting coin cells at APS Sector 34 133
Figure C.5: 3D rendering of coin cell holder used for BCDI measurement 133
Figure C.6: Connecting a coin cell holder 134
Figure C.7: Diagram of AMPIX cell holder 135
Figure C.8: Photograph of AMPIX cell holder 135
Figure C.9: Mounted AMPIX cell 137

LIST OF TABLES

Table 3.1: Classifying the type of cathode 42

Table B.1: Experimental and simulated lattice parameters 112
Table B.2: Experimental and simulated Pb-I-Pb bond lengths and angles, with relaxed MA cation 113
Table B.3: Experimental and simulated Pb-I-Pb bond lengths and angles, with fixed MA cation. 114

ACKNOWLEDGEMENTS

Thanks to my research group for being a constant resource. Thanks to my advisor for always being supportive. Thanks to my family and friends for always encouraging me.

Chapter 3, in full, is currently being prepared for submission for publication of the material. The dissertation author was the primary investigator and author of this paper. Thanks to my co-authors A. Singer, S. Hy, A. Shabalin, C. Fang, M. Zhang, A. Ulvestad, J. Wingert, N. Hua, S. Hrkac, H. Liu, R. Harder, E. Maxey, J. Masser, Y. S. Meng, and O. G. Shpyrko.

Chapter 4, in full, is currently being prepared for submission for publication of the material. The dissertation author was the primary investigator and author of this paper. Thanks to my co-authors A. Singer, B. M. May, S. Hy, J. Wingert, A. Shabalin, S. Hrkac, R. Harder, E. Maxey, J. Masser, J. Cabana, Y. S. Meng, and O. G. Shpyrko.

Chapter 5, in part, is currently being prepared for submission for publication of the material. The dissertation author was the primary investigator and author of this material. Thanks to my co-authors A. Singer, A. Shabalin, M. Zhang, C. Fang, J. Wingert, S. Hrkac, E. Maxey, R. Harder, J. Masser, Y.S. Meng, and O.G. Shpyrko.

Chapter 6 is not currently being prepared for publication. Thanks to my collaborators A. Singer, C. Fang, S. Hrkac, N. Hua, J. Wingert, A. Shabalin, R. Harder, E. Maxey, J. Masser, Y.S. Meng, and O.G. Shpyrko.

Chapter 7 is not currently being prepared for publication. Thanks to my collaborators G. Luo, P. Parekh, S. Wang, A. Shabalin, J. Wingert, J. Ruby, N. Hua, S. Hrkac, S. Hy, R. Harder, E. Maxey, J. Masser, D. Fenning, Y.S. Meng, and O.G. Shpyrko.

VITA

2013	Bachelor of Science in Physics, Massachusetts Institute of Technology
2014	Master of Science in Physics, University of California San Diego
2019	Doctor of Philosophy in Physics, University of California San Diego

ABSTRACT OF THE DISSERTATION

Bragg Coherent Diffractive Imaging of Energy Storage and Conversion Materials

by

Devin Cela

Doctor of Philosophy in Physics

University of California San Diego, 2019

Professor Oleg G. Shpyrko, Chair

Nanoscale disorder plays an essential role in guiding material properties which promise to solve many global challenges. Two such challenges are renewable energy generation and storage. Among lithium-ion batteries, lithium rich layered oxides (LRLO) are one of the most promising classes of cathode materials, delivering more than 50% capacity over leading commercial battery cathodes. In solar cells, a class of absorbers called hybrid organic-inorganic perovskites promise printable solar cells as efficient as the best silicon-wafer cells and at a fraction of the cost. A variety of challenges at the nanoscale, however, prevent the rapid commercialization of either. With imaging techniques limited in terms of sample environments, averaging over large ensembles of particles, or lacking adequate spatiotemporal resolution for studying the relevant physical processes, characterization has also remained a challenge. The majority of this thesis is on the use of *operando* Bragg coherent diffractive imaging (BCDI) for energy storage and conversion materials. Some figures and analysis also make use of powder X-ray diffraction, ”ensemble” or multi-particle coherent X-ray diffraction, density functional theory (DFT), and X-ray photon correlation spectroscopy (XPCS). The main findings are related to the properties of lithium-ion battery cathodes. In Chapter 3 I discuss a striking three-fold rotational symmetry of the displacement field in LRLO cathodes. This effect is drastically reduced or eliminated in two different compositions of classically layered oxides (CLO), respectively, as well as being strongly effected by the charge/discharge process. This result illuminates the effects of surface strain on the bulk cathode physical structure and its effect on the overall battery performance. In Chapter 4 I show that different annealing conditions of one CLO chemistry (called NCA) have counter-intuitive effects on the overall strain energy landscape and dislocation density. Chapter 5 reviews measurements of thick CLO cathodes, and Chapter 6 summarizes work on a different LRLO chemistry. In Chapter 7, I discuss measurements of different solar cell absorbers and the challenges they pose for BCDI.

Chapter 1

Introduction

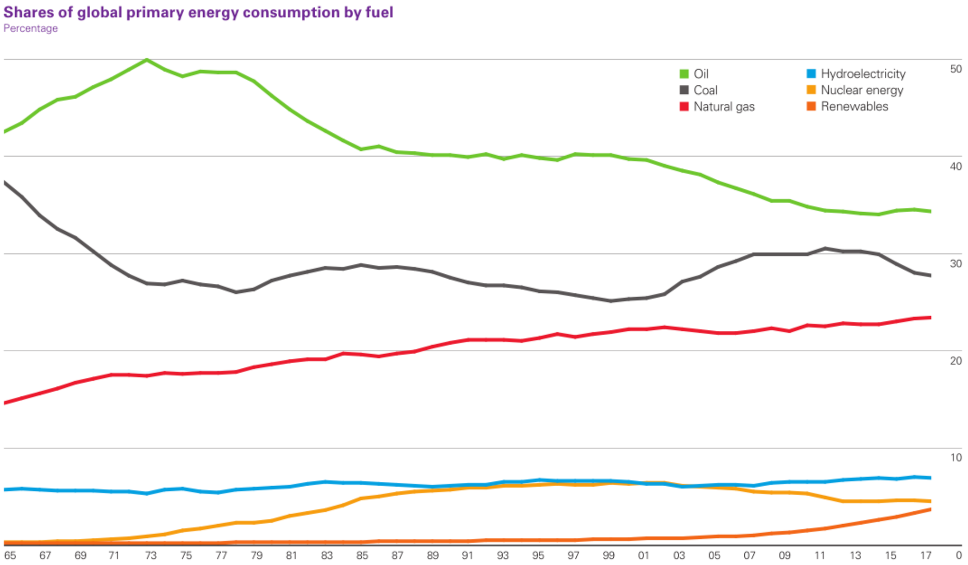

Figure 1.1: The shares of global energy consumption by fuel, as a percentage.[1]

In 2012 alone, approximately seven million people died due to air pollution from the burning of fossil fuels, making it now the world's largest single environmental risk. We are currently facing a rapidly changing global climate, an exploding human population, as well as what many biologists agree will be the greatest mass extinction in our planet's history.[2] As the need for energy rises, supplies of fossil fuels dwindle.[3–5] Our requirement for a cheap, clean, and sustainable source of energy as well as a good way to store it is now greater than ever.[6]

1.1 Why use X-rays?

X-ray techniques have many advantage over other imaging modalities. One major benefit is at X-ray energies (normally between 5–10 keV), there is a much higher penetration depth. This allows for a multitude of *in situ* or *operando* experiments. Electron microscopy, in comparison, requires thin slices of material, limiting the variety of possible experiments and their relation to actual materials. A second benefit is that the potential resolution is higher with shorter wavelengths, at the scale of Angstroms for X-rays. Yet a third benefit is the element specificity due to differing absorption of elements. This opens up the possibility of experiments that map particular elements or oxidation states in a material.[7] Lastly, X-ray sources have increased in

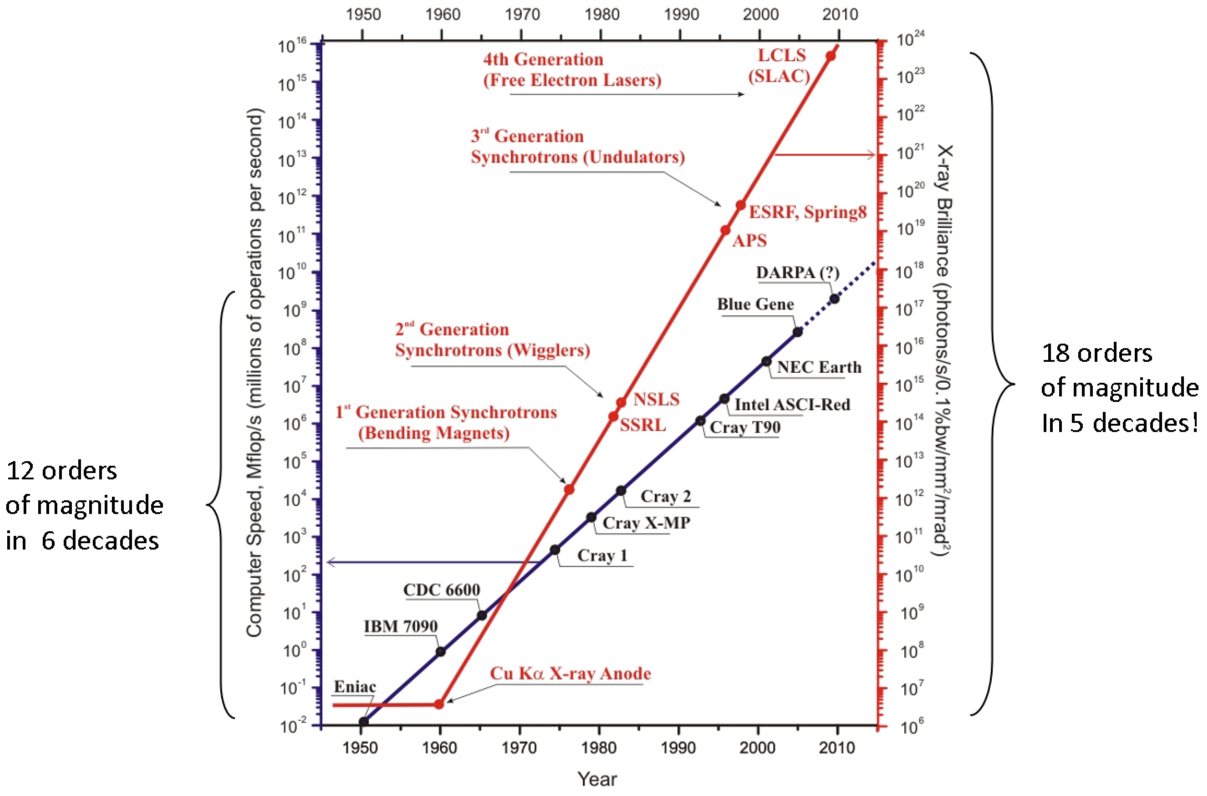

Figure 1.2: A comparison between Moore's Law for computer speed and X-ray source brilliance over the same time interval. The brilliance is defined as the photon flux/(divergence × size) per 0.1% bandwidth.

peak brilliance by 18 orders of magnitude since their inception. The brilliance is defined as the photon flux/(divergence × size) per 0.1% bandwidth. As seen in Figure 1.2, this exceeds the rate of Moore's law over the same time interval. Below is a summary of the types of X-ray sources named in Figure 1.2, with a few examples of each:

- 1st Generation Sources - Ran parasitically on accelerations for high- energy physics (CHESS and SSRL originally)
- 2nd Generation Sources - Built to optimize synchrotron radiation from bending magnets, called wigglers (NSLS)
- 3rd Generation Sources - Built to optimize synchrotron radiation from insertion devices, called undulators (ALS, APS, NSLS-II, ESRF, Spring8)
- 3.5 Generation Sources - Based on multi-band achromat (MBA) storage ring lattices to go towards a diffraction-limited source (ALS-U, APS-U)
- 4th Generation Sources - fully coherent sources. X-ray free electron lasers or X-FELs (such as LCLS), and Diffraction Limited Storage Rings (DLSRs)

1.2 Lithium-ion batteries

Lithium ion batteries are ubiquitous in a wide range of technologies, including cell phones, electric vehicles, and the energy grid, and are indispensable in the transition toward sustainable energy technology. One of the critical challenges in transitioning to a renewable-energy economy is the move away from fossil fuel-powered vehicles. There were estimates of over 1 billion motor vehicles in use in 2010, with predictions of over 2 billion by 2020. Li-ion batteries provide one of the best bets for making this transition.[8]

$LiMO_2$ (M= Ni, Co, Mn, Al) pertains to a family of layered battery cathode materials with alternating layers of lithium and transition-metal (TM) layers (see Figure 1.3). Variants of the

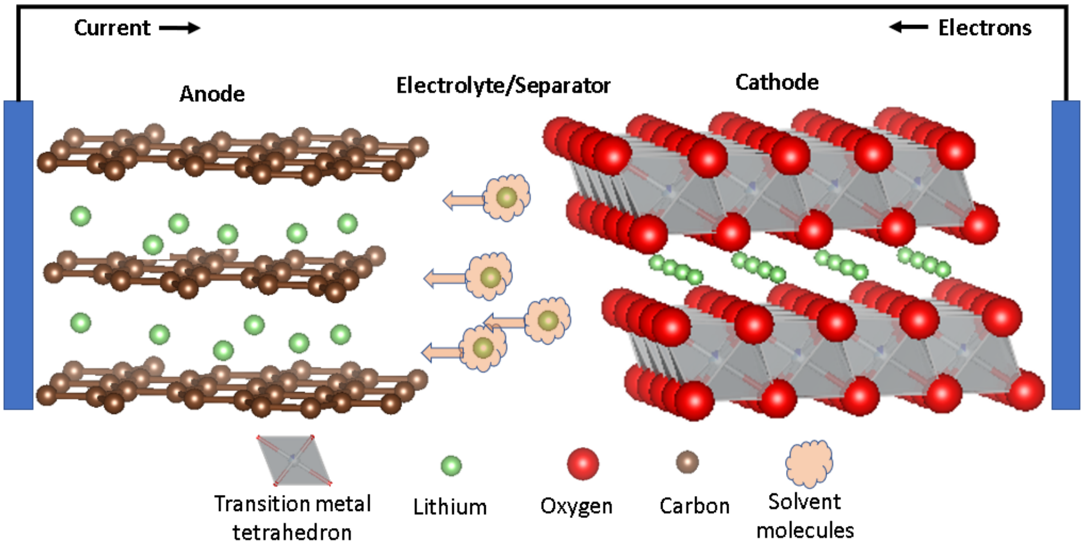

Figure 1.3: Shown is a schematic of a discharging lithium-ion battery producing electric current. The anode is typically graphite, and the cathode in this case is a layered transition metal oxide. Electrolyte allows for Li^+ ions to move freely along the chemical potential gradient and minimize the Gibbs free energy of the system. A physical separator (normally a glass fiber mesh) keeps the anode and cathode from directly contacting and shorting the system.

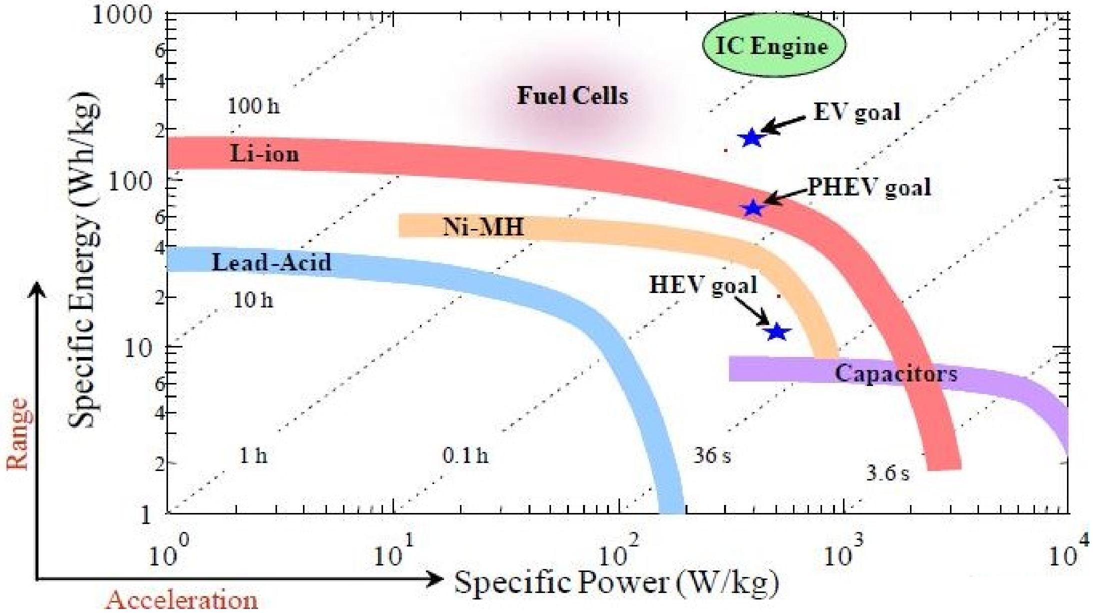

Figure 1.4: Ragone plot of energy sources for electric vehicles. We can never hope to match the specific energy of fossil fuels, the overall energy output due to higher conversion efficiency can. Adapted from a presentation by Y.S. Meng.

material have been successfully commercialized, such as in Panasonic batteries for Tesla electric vehicles. However, as electric vehicles still face issues with range, power, and cost, it is necessary to continue to optimize the material properties.[9–11] Figure 1.4 is a Ragone plot stipulating roughly where we are in the current state of the art, as well as general goals for electric vehicles in terms of specific energy and specific power.

The battery performance is inherently connected to the capability of lithium ions to reversibly intercalate with the electrodes. One of the most promising candidates for the next generation of lithium ion battery cathode materials is the lithium-excess layered oxide (LRLO). It has an extraordinary high capacity of up to 320 mAh/g versus a practical capacity of 1̃50 mAh/g for the commercial $LiCoO_2$ whose increase is a subject of active research in the battery community.[12–15]

1.2.1 Issues limiting batteries

In a battery cathode lithium is repeatedly intercalated and deintercalated in a variety of ways, straining the system and eventually causing the system to fail. Causes include surface reactions forming an surface-electrolyte interface (SEI), forming of dislocations leading to premature cracking of particles, or corrosion of the cathode into an electrochemically inert structure.[16,17]

The promising LRLO material has several issues preventing commercialization. This material undergoes voltage fading and instability that is rooted in structural failure, and despite their importance, the community has not yet gained a fundamental understanding of the structural transformations that occur. With *in situ* studies on single nanoparticles of this material one can shed light on the structure evolution during charge/discharge and ultimately identify and mitigate obstacles for improved cycling performance.[16,18]

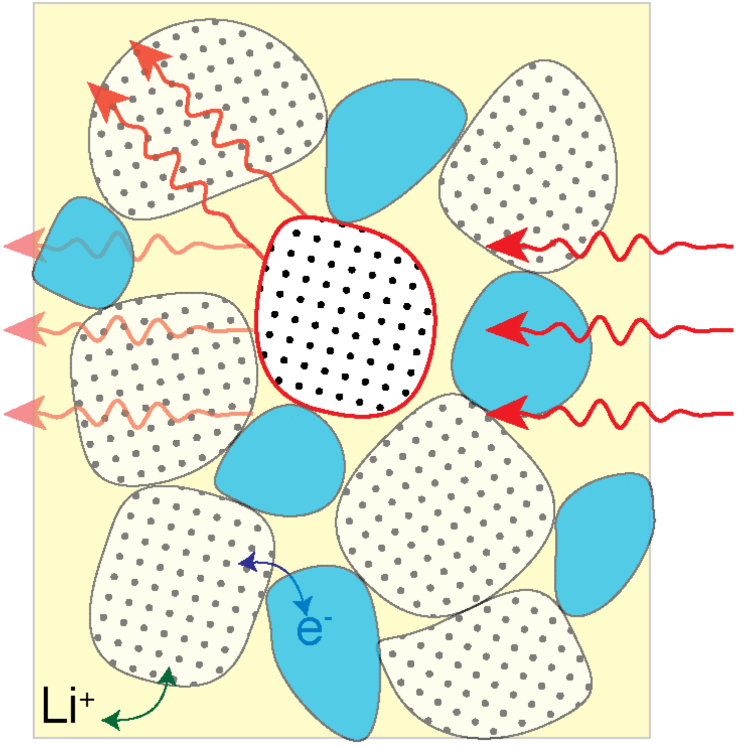

Figure 1.5: Sketch of a battery nanoparticle in the Bragg condition. Many particles might be illuminated in an incident X-ray beam, but very few will match the condition for Bragg diffraction to within a degree of rotation. This allows me to only measure signal from a single crystal, a necessary prerequisite for BCDI. In this image, crystals (white with dotted grids) are surrounded by organic binder (blue) gluing them together and increasing the electrical conductivity. The electrolyte (yellow background) transports Li^+ ions into and out of the crystal, depending on the direction of charging.

1.2.2 Measurement with Bragg coherent diffractive imaging

My aim was to understand the structural dynamics in a nanoparticulate electrode in an *in situ* battery. The random orientation of crystals within a cathode allows me to image only a single nanocrystal at a time which is in the Bragg condition. The sample morphology is sketched in Figure 1.5. I concentrated on a scientifically and technologically relevant lithium excess oxide $Li_{1.2}Ni_{0.133}Mn_{0.534}Co_{0.133}O_2$, as well as a number of other cathode chemistries. Unlike the stoichiometric lithium layered oxides that relies solely on the topotactic reaction with the transition metal redox pairs, the lithium-excess oxide also undergoes oxygen activation at high voltages. The activation of oxygen induces structural rearrangement and transformation which has not been observed under non-equilibrium conditions at these length scales.[19]

Experiments were completed at the APS Sector 34-ID-C. Results of a number of experiments on lithium-ion batteries are discussed in Chapter 3, 4, 5, and 6.

1.3 Perovskite solar cells (PSCs)

1.3.1 Functional hybrid materials

Figure 1.6: A piece of Mayan artwork, with the Maya blue the only remaining vivid color.[20]

In 1946 a site in Mexico was found to contain ancient Mayan frescoes containing startlingly vivid shades of blue, a pigment which came to be known as Maya blue. The blue color was memorable, but even more impressive is the durability. While all the other colors had faded, that blue had remained strong for well over a hundred years (see Figure 1.6). After more than fifty years, analytical techniques have uncovered the secret of the color. Maya blue is a hybrid organic-inorganic material with molecules of blue indigo trapped within a clay mineral called palygorskite. It is a synthetic material that combines the color of the organic pigment with the resistance of the inorganic host, with properties that go beyond those of a simple mixture of its components.[20–22]

We have come a long way in our understanding of hybrid materials since the Mayan empire. Some of the earliest hybrid materials were mixtures of inorganic pigments or fillers dispersed in organic components to improve optical and mechanical properties in paints and polymers. However, true ”hybrid inorganic-organic” materials are more complex than that. As the size of the interacting particles gets reduced, the interactions at the interface become more important, and at the nanoscale with molecular interactions, the chemistry between components becomes much more important. They were first developed as intercalation materials, but a burst of progress came with the use of soft inorganic chemistry processes with mild synthesis conditions which allowed for design of chemical properties.

There is currently a growing field of research focusing on functional hybrid materials, which combine nanoscale components to create multifunctional materials. The chemical and physical nature of these materials, as well as their potential applications, varies widely. Functional hybrids have applications in diverse fields such as optics, electronics, coatings, catalysis, sensors, and biology. Despite the large variety of possible materials and synthesis methods, they are all prepared at the same relatively low temperatures (normally room temperature). This work will focus on the use of functional hybrid materials for use in photovoltaics.[21]

1.3.2 The growth of hybrid photovoltaics

Solar power is perhaps the only feasible technology with the potential to provide for the energy needs of the entire world.[6]

The transition towards renewable energy is one of the most profound challenges of today’s science and technology and requires the discovery of novel phenomena and materials. Solar

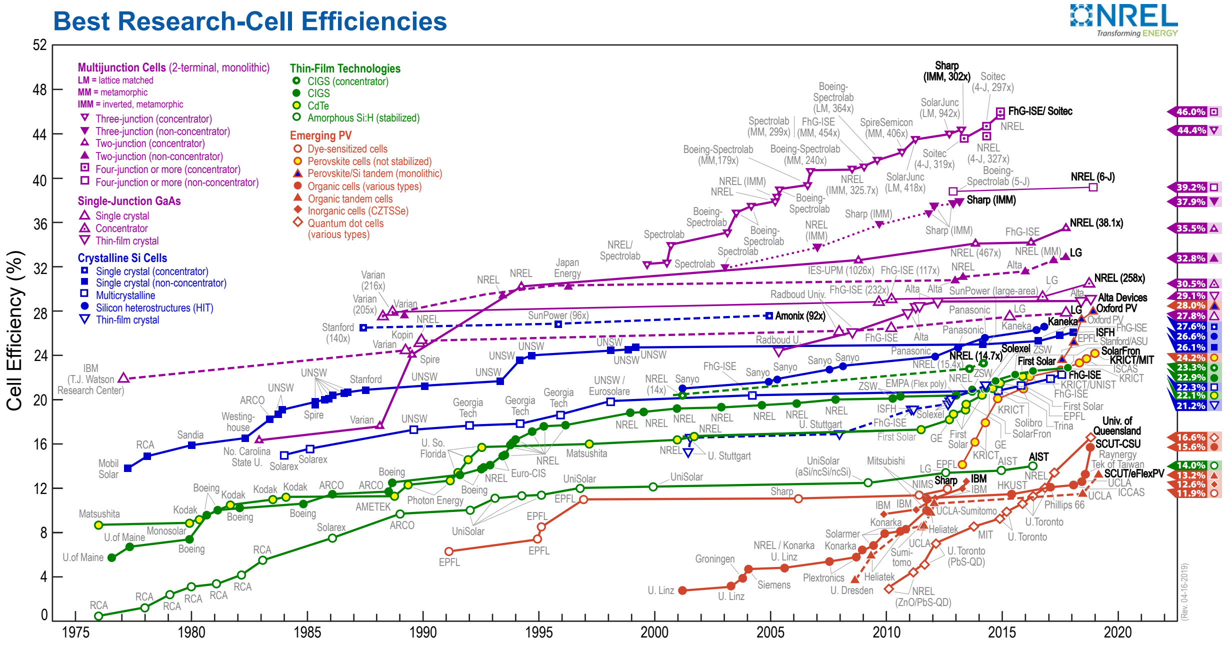

Figure 1.7: The growth of perovskite solar cell efficiencies relative to all other thin-film technologies[23]

power has the potential to provide for the energy needs of the entire world. Hybrid perovskite solar cells (PSCs) are a cheap, easy-to-make alternative to more traditional silicon and GaAs-based photovoltaics and have already equaled or surpassed the efficiency of established thin-film technologies such as cadmium telluride (CdTe), copper indium gallium selenide-based cells (CIGS), organic photovoltaics (OPV), and amorphous silicon (Si). In a few short years, PSC efficiencies has shot up to over 24% (see Figure 1.7). A high absorption coefficient, allowing the use of less material, coupled with low temperature solution processing, enables high efficiency, low cost solar cells to be fabricated on a large scale. Their method of fabrication allows for roll-to-roll printing of "solar paint" on paper-thin plastics, and their tunable properties means that they could be used as a transparent layer in windows in what are called building-integrated photovoltaics.

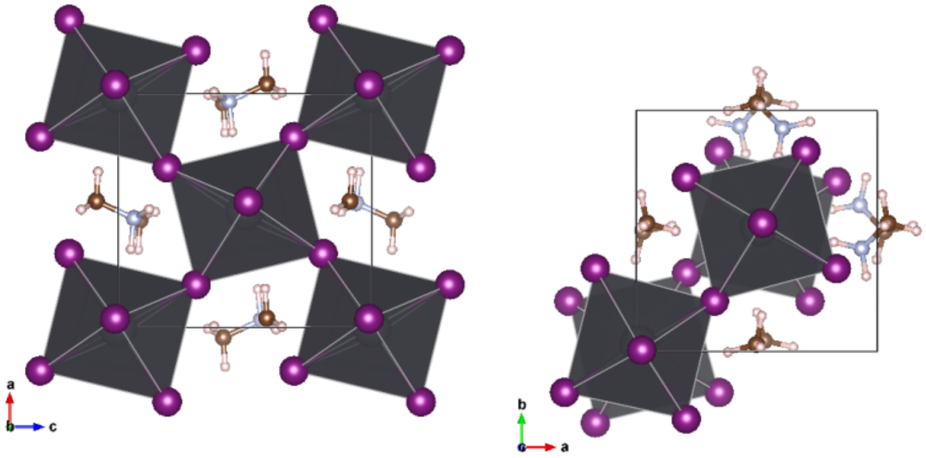

(a) Orthorhombic (b) Tetragonal

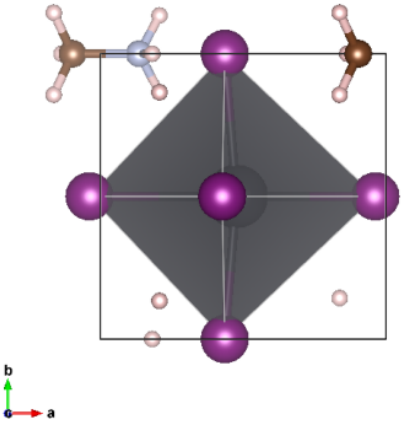

(c) Cubic

Figure 1.8: The three phases shown along the direction of their longest axis. Pb is gray, I purple, N blue, and C red, with tan hydrogen. iodide atoms.[24]

1.3.3 Crystal structure and phases

Perovskites are a class of semiconductors with the chemical formula ABX_3 . This structure consists of a network of corner-sharing BX_6 octahedra, in which the metal cation B, often Pb^{2+} or Sn^{2+}, is in the center. X represents a monovalent anion (Cl^- , Br^- , or I^-) and A, a monovalent cation such as the organic molecule $[CH_3NH_3]^+$, neutralizes the overall charge. The geometrical structure of hybrid cubic perovskites is shown in Figures 1.8, 1.9.[25]

As the temperature is increased from below 165 K to above 327 K the lead-halide

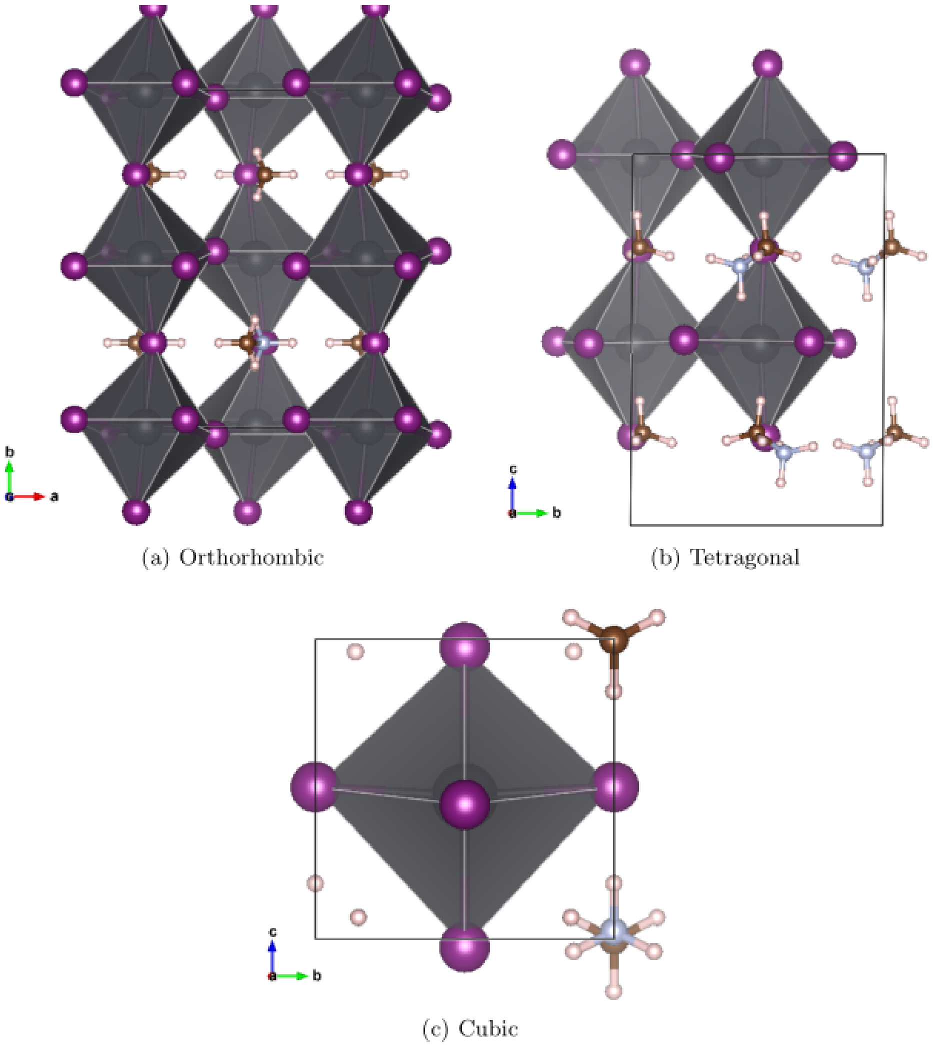

(a) Orthorhombic

(b) Tetragonal

(c) Cubic

Figure 1.9: The three phases shown along the direction of their shortest axis. Pb is gray, I purple, N blue, and C red, with tan hydrogen. iodide atoms.[24]

perovskite structure $CH_3NH_3PbI_3$ changes from an orthorhombic phase below 165 K to a tetragonal phase stable between 165 K and 327 K, to a cubic phase stable above 327 K.

In the orthorhombic phase (Figures 1.8a, 1.9a), the cations are fixed, as rotation of the C-N axis is restricted due to strong hydrogen bonding between the NH_3 groups and the framework.

As the temperature is increased the thermal motion of the cation increases and the hydrogen bonds are not sufficient to hold it in place. At the transition to the tetragonal phase at 165 K (Figures 1.8b, 1.9b), there are a number of orientations that are possible and the cation can move between any of these. The MA cation is slightly off-center from the unit cell with weak hydrogen bonding occurring between N-H and I. The -NH_3 and CH_3 groups can essentially freely rotate about the C-N bond.

As the temperature is further increased, the cation moves towards the octahedral cavity center (the A-site cavity of the perovskite structure) and the perovskite material enters a cubic phase (Figures 1.8c, 1.9c). The Pb-I-Pb bonds straighten and the c/a ratio is reduced towards unity. In the cubic phase the MA^+ cation seems to remain directed towards the cubic faces in six possible orientations, with significant positional and thermal disorder. The MA ion is able to freely rotate on the picosecond time scale.[24]

The high level of orientational motion of the cation at room temperature seems to be related to the photovoltaic performance of the material, but also the hysteresis effects that have been reported. Walsh et al. have proposed that the internal electrical fields associated with microscopic polarization domains contribute to the hysteresis due to variations in electron-hole recombination.[26]

The phase transition is important due to the fact that the average solar panel will typically be operating at temperatures very close to the tetragonal→cubic phase transition. The constant changing in crystal structure as the material heats and cools may lead to a reduced stability.[27]

Perovskites such as methyl ammonium lead iodide ($CH_3NH_3PbI_3$) and formamidinium lead iodide ($CH(NH_2)_2PbI_3$) have been the major focus of study among various groups. An efficiency of over 24% has been reported for this class of materials, and yet a clear understanding of the device interfaces is demanded to further improve its performance and stability.

1.3.4 Current challenges

A typical cell consists of a perovskite active layer sandwiched between an electron transport and a hole transport layer. These are followed on either side by a charge collection layer to complete the external circuit. Though widely accepted that the perovskite material

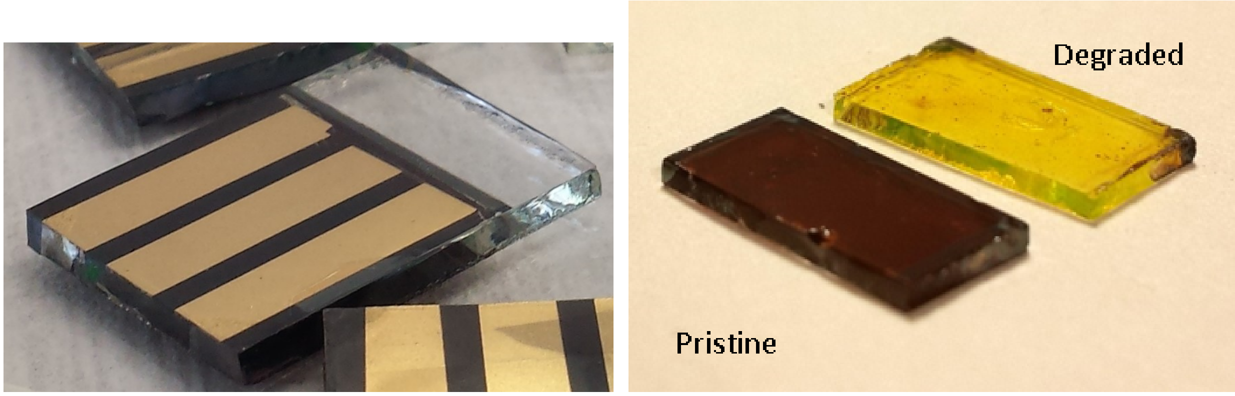

(a) A fabricated hybrid perovskite solar cell

(b) Moisture degradation of hybrid perovskites occurs rapidly. Here, the dark (pristine) hybrid perovskite is shown next to an adjacent yellow (degraded) lead iodide that remains after exposure to water.

Figure 1.10: Maintaining the stability of perovskite solar cells.

($CH_3NH_3PbI_3$ as well as $CH(NH_2)_2PbI_3$) degrade in the presence of moisture, in a solar cell device, encapsulation by the hole transport layer prevents its direct contact with moisture in the air. A number of reports have studied the effect of moisture directly on the perovskite layer but there have been no reports on understanding how the moisture percolates to the perovskite, through the hole transport layer.

One of the major criteria to commercialize perovskite solar cells is long-term stability and reliability. In order for devices to be stable, the degradation pathway for the entry of moisture into the solar cell (see Figure 1.10b) needs to be understood.[28,29]

Current photovoltaic technology is dominated by silicon cells with over 5 decades of intensive research and optimization. High efficiencies of over 26% and lifetimes of 30 years have enabled successful commercialization, but high manufacturing costs and expensive installation costs have prompted research in new directions. Emerging photovoltaic technologies such as organic, dye-sensitized, quantum dot and perovskite solar cells show great promise, but each one suffers its own issues. Hybrid organic-inorganic perovskite solar cells offer advantages that rival the Si cells in terms of efficiency and cost, making it a highly viable candidate for commercial use. With certified efficiencies of over 24%, their performance can be attributed to long charge carrier lifetimes, large carrier diffusion lengths, large light absorption coefficient and minimal influence of defects on the band gap

Typical device architecture consists of an intrinsic perovskite layer; prepared by spin coating a layer of lead iodide PbI2 dissolved in DMF (dimethyl formamide) followed by dip coating in a solution of methyl ammonium iodide (CH_3NH_3I) dissolved in IPA (isopropanol). A chemical reaction between PbI_2 and CH_3NH_3I through a solvent mediated process enables the formation of the perovskite material ($CH_3NH_3PbI_3$). This perovskite layer is encapsulated on one side by an electron transport layer (TiO_2), and on the other side with an organic hole transport layer (spiro-OMeTAD with additives). A number of different device architectures and processing techniques that employ solvent engineering have been reported to prepare high efficiency device but the stability of all such devices is still poor (a few days to weeks).

The stability is affected by two factors: (1) The perovskite material decomposes back to its precursors on exposure to moisture; (2) encapsulation of the perovskite by the organic spiro-OMeTAD hole transport layer would affect moisture ingress pathways. Our studies suggest that the morphology of the organic hole transport layer significantly affects the moisture ingress pathway. However, many key questions remain unanswered. Specifically, which ions prefer to interact with moisture in the hole transport layer? How does the interface act to dynamically advance the degradation of the perovskite layer? What role do the grain boundaries play during the degradation? Answers to these questions can help researchers find effective new solutions to the stability bottlenecks inhibiting these materials from full commercial realization. In this study we will aim to greatly enhance the understanding of interface chemistry and grain boundaries.

Michael Grätzel and collaborators have created a cell architecture that maintains a reasonable stability at an efficiency near 13%. Instead of having a hole-transport layer and evaporated metal contact, they use a porous zirconium oxide layer and a carbon back electrode. This $TiO_2/ZrO_2/C$ structure is infiltrated with perovskite. The cells were tested outdoors in the summer sun, as well as in two indoor tests.[30]

The first was at 85° C in dark conditions for 90 days, testing the thermal stability. In this test the cells lost about 10% of their initial efficiency. The lifetime of a solar cell is defined as the time it takes for a 20% efficiency loss, so this corresponds to a lifetime of about 180 days, if we assume a linear decay rate. The International Electrotechnical Commission has a damp heat test (85° C, 85% relative humidity) which requires a maximum 10% efficiency loss in 1,000 hours, which is about 40 days. These cells therefore easily pass the temperature portion of this test.[28, 30] The second test was under illumination at 45° C for 44 days in an inert argon atmosphere. In these favorable conditions, the cells maintained their stability. Although PSCs have not yet reached the long-term stability of crystalline silicon solar cells, this evidence suggests that they may be intrinsically stable. It is clear that rapid progress is quickly leading to commercialization.

My own experiments and results are discussed in Chapter 7 and Appendices A and B.

Chapter 2

Coherent X-ray scattering theory

The Bragg coherent diffractive imaging (BCDI) was the primary technique used in my thesis, and therefore I will go over its theory and implementation in some detail.

2.1 Fundamentals of lensless imaging

One benefit of lensless imaging with X-rays is that the theoretical resolution can be much higher than with a physical objective lens.[31] The smallest distance to resolve two points is determined by the Rayleigh criterion: the central peak of the Airy pattern formed from one circular aperture of size d and a distance from the detector z is located at the first minima of the Airy pattern from a second hole at a distance δ_t. This yields the relation

$$\nabla_t = \frac{1.22\lambda z}{d} = \frac{0.61\lambda}{N.A.} \tag{2.1}$$

where $N.A$ is the numerical aperture.

2.1.1 Far field imaging

In free space, the wave propagation equation can be written as the Helmholtz equation

$$\triangle^2\psi(\mathbf{r}) + k^2\psi(\mathbf{r}) = 0. \tag{2.2}$$

Taking the Fourier transform in the transverse plane, one obtains

$$(-\mathbf{q}_\perp^2 + \partial_z^2 + k^2)\bar{\psi}(\mathbf{q}_\perp;\mathbf{z}) = 0, \tag{2.3}$$

with the general solution having the form

$$\bar{\psi}(\mathbf{q}_\perp;\mathbf{z}) = \bar{\psi}(\mathbf{q}_\perp;\mathbf{0})e^{i\kappa z} \tag{2.4}$$

with $\kappa = \sqrt{k^2 - \mathbf{q}_\perp^2}$. If the wave at the sample exit ψ_0 serves as our boundary conditions,

$$\psi(\mathbf{r}_\perp;\mathbf{z}) = \mathcal{F}^{-\infty}[\tilde{\psi}_0(\mathbf{q}_\perp^2)e^{i\kappa z}]. \tag{2.5}$$

In the paraxial approximation, one can perform a Taylor expansion around κ to the first non-zero order in $\mathbf{q}_\perp$ to rewrite the above equation as

$$\psi(\mathbf{r}_\perp;\mathbf{z}) = \mathcal{F}\left[\psi_0(\mathbf{R}_\perp)\exp(i\frac{k\mathbf{R}_\perp^2}{2z})\right] \tag{2.6}$$

with $\mathbf{R}_\perp$ the spatial coordinate in the sample plane. In the Fraunhofer approximation, the phase modulation in the exponential term is assumed to be small, with the Fresnel number $n = \frac{a}{\lambda z} << 1$ with a being the average size of the sample. So in the far-field condition, with $z >> \frac{a^2}{\lambda}$, the scattered X-ray beam can be written as simply the Fourier transform of the sample transmittance:

$$\psi(\mathbf{r}_\perp;\mathbf{z}) = \mathcal{F}[\psi_0(\mathbf{R}_\perp)] \tag{2.7}$$

2.1.2 The phase problem

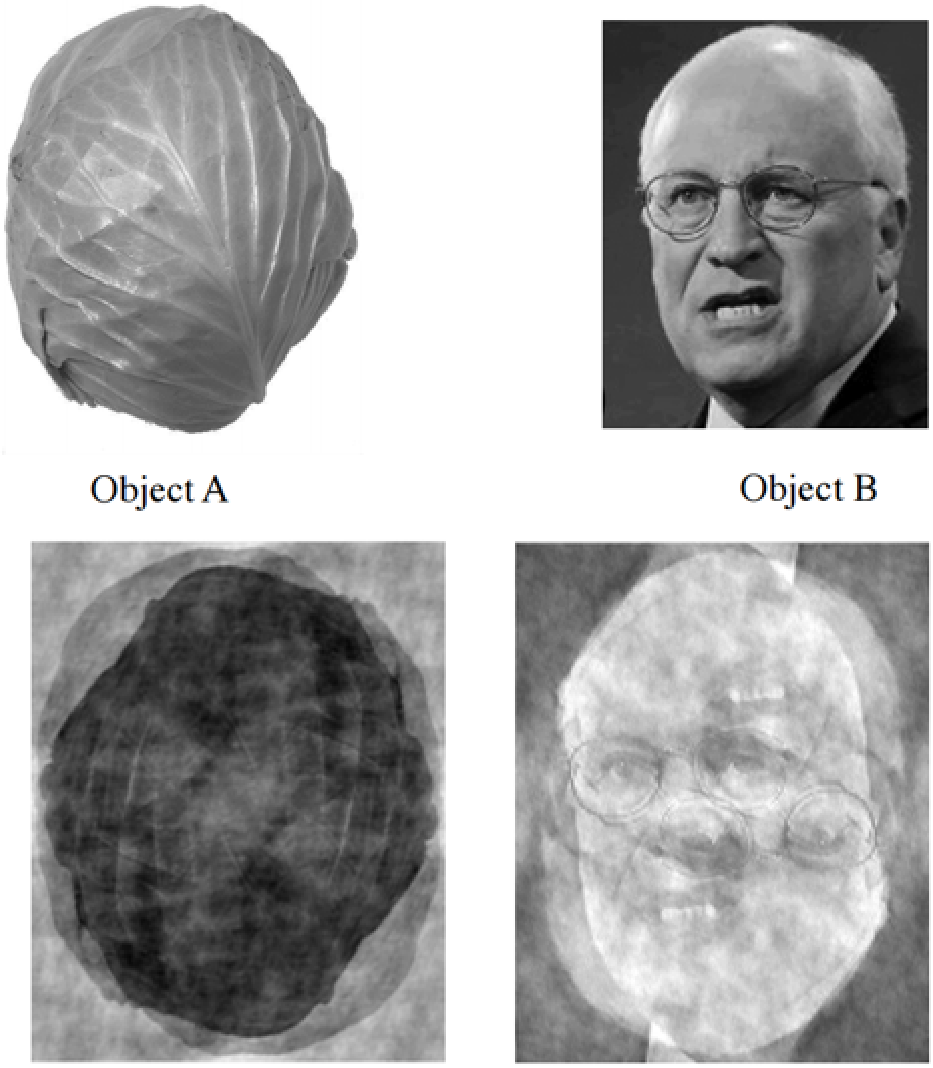

Figure 2.1: In the bottom left panel is the Fourier reconstruction with phases of Object A and amplitudes of Object B. In the bottom right panel is the Fourier reconstruction with phases of Object B and amplitude of Object A. The phase tells us where the different parts of the object are located. Adapted from S.K. Sinha.

We only measure the diffracted intensity $|\mathcal{F}[\psi_0(\mathbf{R}_\perp)]|^2$. The phase of the sample $\phi(\mathbf{k}_\perp)$ is lost. The main challenge of different X-ray imaging techniques is in trying to recover these phases. Written another way, we measure the modulus squared of the electron density:

$$I = |E(\mathbf{q})|^2 = \left| \int_{-\infty}^{+\infty} \rho(\mathbf{r}) e^{-i\mathbf{q}\cdot\mathbf{r}} d\mathbf{r} \right|^2 \tag{2.8}$$

2.1.3 Resolution and limitations

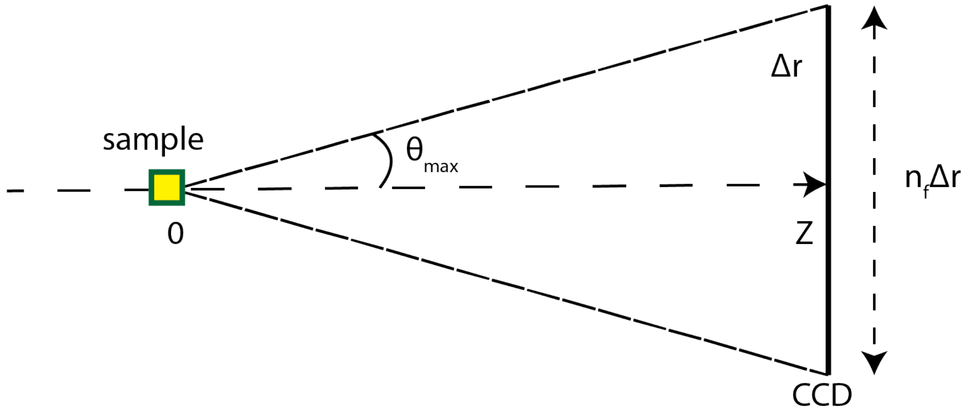

Figure 2.2: Important parameters for determining maximum transverse and longitudinal resolutions, defined in Equations 2.9 and 2.10, respectively.

The maximum transverse resolution for the diagram shown in Figure 2.2 is given by

$$\sigma_t = \lambda \frac{Z}{n_F \Delta r} \tag{2.9}$$

and the longitudinal resolution is given by

$$\sigma_l = 2\lambda \left(\frac{Z}{n_F \Delta r} \right)^2 \tag{2.10}$$

where λ is the wavelength, Z is the sample-to-detector distance, n_f is the number of pixels, and Δr is the pixel size.

Realistically, the resolution will be limited by the signal-to-noise (SNR) ratio. The Rose criterion states that an SNR of at least 5 is needed.[32] Sources of noise include diffuse light from the focusing optics, fluctuations in the beam properties, photon noise (which scales as $\sqrt{number\ of\ photons}$), detector inefficiencies, and partial coherence. Some of these sources can be minimized by improving the experimental setup, binning of images, pre-reconstruction image processing, or the collection of additional statistics with additional scans.

2.2 Coherence requirements

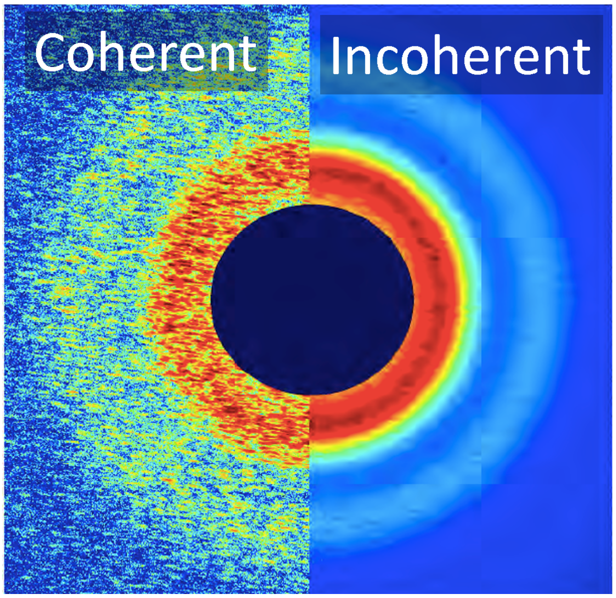

Figure 2.3: Coherent light is able to detect disorder with spatial resolution. Incoherent light, on the other hand, averages over the sample's spatial structure.

Coherence describes the statistical similarity of a field (such as an electromagnetic field) at two points in space or time. Mathematically, the coherence functions between two functions $x(t)$ and $y(t)$ is defined as

$$\gamma_{xy}^2(f) = \frac{|S_{xy}(f)|^2}{S_{xx}(f)S_{yy}(f)} \tag{2.11}$$

where $S_{xy}(f)$ is the cross-spectral density of the signal, and $S_{xx}(f)$ and $S_{yy}(f)$ are the power spectral density functions of $x(t)$ and $y(t)$, respectively. The cross-spectral density and power spectral density are defined as the Fourier transforms of the cross-correlation and autocorrelation signals, respectively. $\gamma_{xy}^2(f)$ varies from 0 to 1, with 1 being perfect correlation and 0 totally uncorrelated.[33]

2.2.1 Temporal coherence

Temporal coherence is the measure of the average correlation between the signal and itself delayed by a time τ, at any pair of times. A wave containing only a single frequency (monochromatic) is perfectly correlated with itself at all time delays. For coherent diffractive imaging, the requirement is given by

$$\frac{\lambda}{\Delta\lambda} \geq \frac{a}{\sigma_t} \tag{2.12}$$

where λ is the wavelength of light, $\Delta\lambda$ is the bandwidth, a is beam spot-size, and σ_t is the transverse resolution defined in Equation 2.9.

2.2.2 Spatial coherence

Although free-electron laser sources are fully spatially coherent, synchrotrons are not. Typically, to perform BCDI at synchrotrons, one makes use of a slit, as the illumination with the half radius of the Airy pattern can be considered as coherent, according to the van Cittert-Zernike theorem.[34] The limitation is thus

$$l_t = \frac{0.61\lambda D}{\phi_{hole}} \tag{2.13}$$

with D the hole-to-sample distance.

Unfortunately, this means one must throw away the majority of the photon flux. Thankfully, in a few years many synchrotron sources are receiving upgrades to boost the relative fraction of coherent light.[35]

2.3 Solving the phase problem with iterative algorithms

There are two initial constraints for this non-convex optimization problem. In Fourier or reciprocal space, we only know the measured intensity as shown in Equations 2.7,2.8. In real space, we know (and make sure to measure) an isolated object. The constraint here will be that the object fits into a region known as a support. The initial support is that the object fits inside its autocorrelation.

By the Nyquist-Shannon theorem, the sampling frequency should be at least twice the highest frequency of the input signal. In other words, with N_F measured amplitudes and N_S sampled points, the oversampling ratio $\sigma = \frac{N_F}{N_S} \geq 2$.[36]

Interestingly, if the dimension $d = 1$, there is no unique solution. However, if $d \geq 2$, then there is almost always a unique solution.

In 3D the oversampling requirement is that the oversampling ratio = 1 in each dimension. The oversampling ratio is given by the ratio of the number of points measured per oscillation of the transform (a fringe) to the number of points necessary to define an oscillation, which is the Nyquist sampling rate.[36]

The phasing of an oversampled diffraction pattern may be accomplished through the use of an iterative method, utilizing known information to find a set of phases consistent with the measured data. The fitting begins by assigning a set of random phases to the support and evaluating (2) using a fast Fourier transform, which yields a first ”guess” at the diffraction pattern in reciprocal space. The amplitude of the guess is then overwritten with the measured amplitude and back transformed to yield a complex density in real space. After applying an appropriate real space constraint – for example, enforcing a finite support and converting the density to a real, non-negative function – it is transformed back to reciprocal space. This cycle is repeated until the search converges to a solution. This is known as the error reduction method and is the simplest formulation (sketched out in Figures 2.4, 2.5).[36, 37]

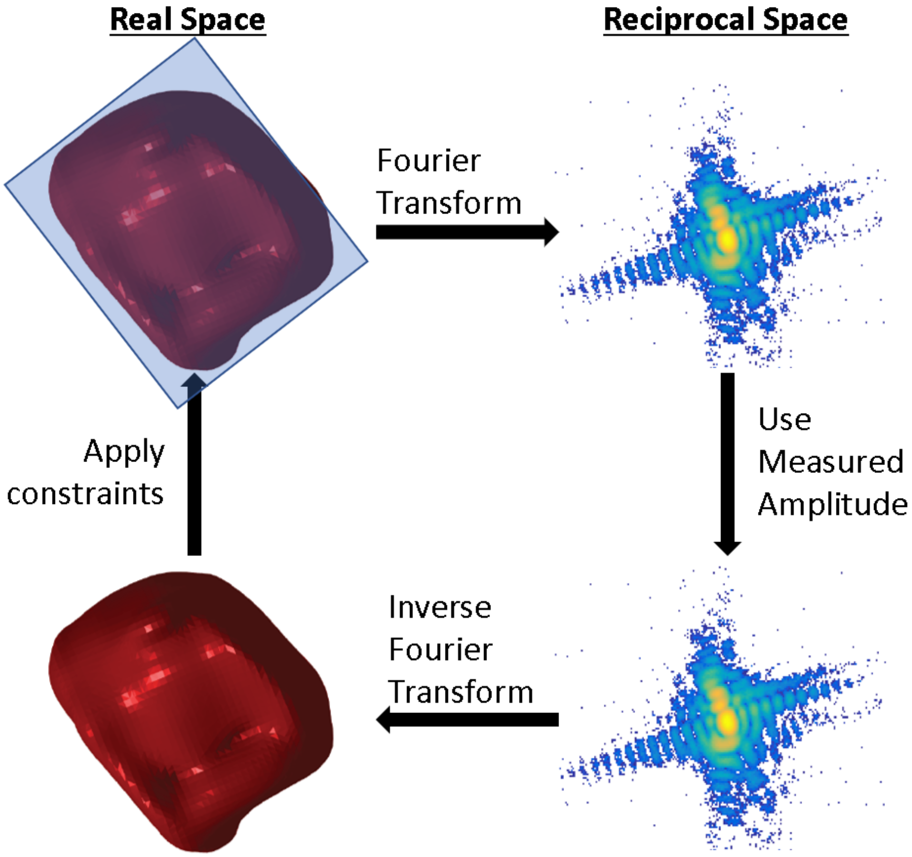

Figure 2.4: Sketch of generic phase retrieval algorithm using actual reconstructed particle shape and diffraction pattern.

The reconstruction error metric (χ-squared) is given by the square of the differences of the measured and fitted amplitudes per pixel, normalized by the measured amplitude. This is the error minimized in each iteration.

2.3.1 Error reduction (ER) phase retrieval algorithm

The error reduction (ER) algorithm (sketched out in Figure 2.5) attempts to find a solution fulfilling the previously mentioned constraints for real space,

$$P_S \rho(\mathbf{r}) = \begin{cases} \rho(\mathbf{r}), & \text{if r} \in \text{Support} \\ 0, & \text{otherwise} \end{cases} \tag{2.14}$$

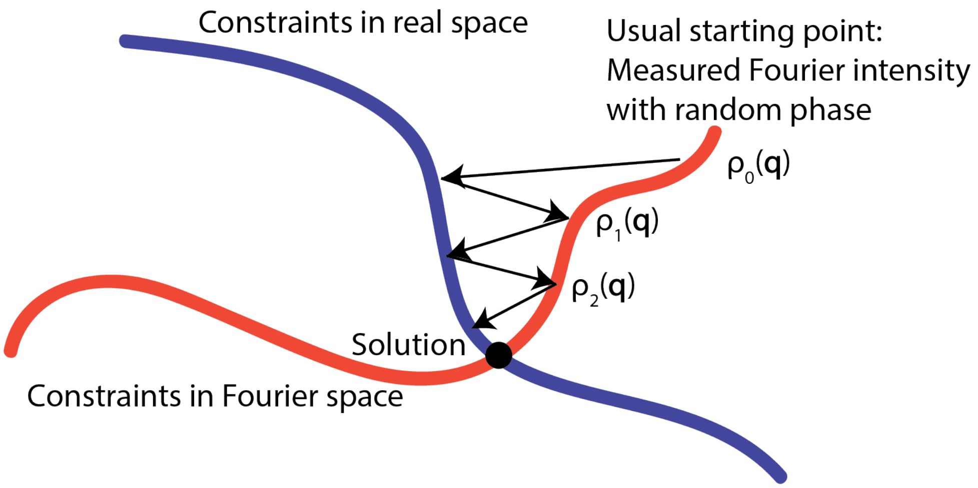

Figure 2.5: Sketch of error-reduction phase retrieval algorithm. The error reduction algorithm tends to be accurate but converge slowly compared to other phase retrieval algorithms.

and in Fourier space,

$$\tilde{P_F}\tilde{\rho}(\mathbf{q}) = \sqrt{I(\mathbf{q})}e^{i\phi(\mathbf{q})} \tag{2.15}$$

with $P_F\rho(\mathbf{r}) = \mathcal{F}^{-1}(\tilde{P_F})\mathcal{F}$. This leads us to the relation

$$\rho_{n+1}(\mathbf{r}) = P_S P_F \rho_n(\mathbf{r}) \tag{2.16}$$

One can modify the two constraints on the real and reciprocal space projections for particular problems.

In real space:

- If the object is real: Positivity
- The absorption cannot be negative
- Pure phase object

In reciprocal space:

- When data are missing (e.g. from detector lines or a beam block)

- Noisy data (filtering)

One problem with the error reduction algorithm is that, although it will always converge, it tends to become stuck at local minima and take a very long time.[38]

2.3.2 Other popular algorithms

There are a number of other algorithms that have been created. These variations on the ER algorithm make use of feedback parameters from previous reconstructions. Three of the most common are outlined below. For all, the optimal parameters will depend on the specific problem being solved.

The hybrid input-output (HIO) method incorporates a parameter, β, defining a fraction of the previous cycle's result to combine with the current result. Additionally, the real space constraint is relaxed by allowing a small amount of amplitude to exist outside the support.

$$\rho_{n+1} = \rho_n + \beta[P_S((1+\beta^{-1})P_F\rho_n - \beta^{-1}\rho_n) - P_F\rho_n] \tag{2.17}$$

HIO is often used in alternation with ER (known as the alternating projection scheme). The key idea is that HIO can converge much faster to a global minimum, and that ER still works best for converging to the bottom of that minimum.The hybrid input-output algorithm outlined in Equation 2.17 is identical to 2.16 if $\beta = 0$.[39]

$$\rho_{n+1} = \rho_n + \beta[P_S(2P_F\rho_n - \rho_n) - P_F\rho_n] + (1-\beta)(P_F\rho_n - \rho_n) \tag{2.18}$$

The relaxed average alternating reflector (RAAR) algorithm outlined in Equation 2.18, with suitable choice of parameters, can also be distilled down to a version of ER.[40]

$$\rho_{n+1} = \rho_n + \beta P_S[(1+\gamma_S)P_F\rho_n - \gamma_S\rho_n] - \beta P_F[(1+\gamma_F)P_S\rho_n - \gamma_F\rho_n] \tag{2.19}$$

The difference map algorithm (see Equation 2.19) reproduces the “hybrid” form of HIO when a particular choice is made for two of the parameters. It attempts to avoid stagnation problems of alternating projection schemes.[38,39]

2.3.3 Shrink wrap

If the support is too large, convergence to a solution will be slow, and there can be problems due to symmetric reconstructions (this is known as the twin image problem, and refers to the fact that the same intensity pattern allows for two unique solutions due to the imaginary component). Thus one needs a method to reduce the support size.

In the shrinkwrap method, one updates the support according to the amplitude of the nth reconstruction, where n is less than the number of iterations per reconstruction.[41]

2.3.4 Assessing accuracy of reconstructed objects

The actual resolution will always be lower than the theoretical one, and there are different competing definitions and criteria that are used to measure it. One commonly-used possibility is to make use of the phase retrieval transfer function (PRTF).[42]

$$PRTF(q) = \frac{\langle|\mathcal{F}(\rho(\mathbf{r}))|\rangle}{\sqrt{I_{measured}(q)}} \tag{2.20}$$

where averaging is done over multiple reconstructions. Equation 2.20 gives a degree of confidence that the correct phases were retrieved. If they were, the values add together, otherwise it will tend towards zero. The actual resolution is given by the value of q when $PRTF(q) < 1/e$.

2.4 Understanding strain in coherent diffractive imaging

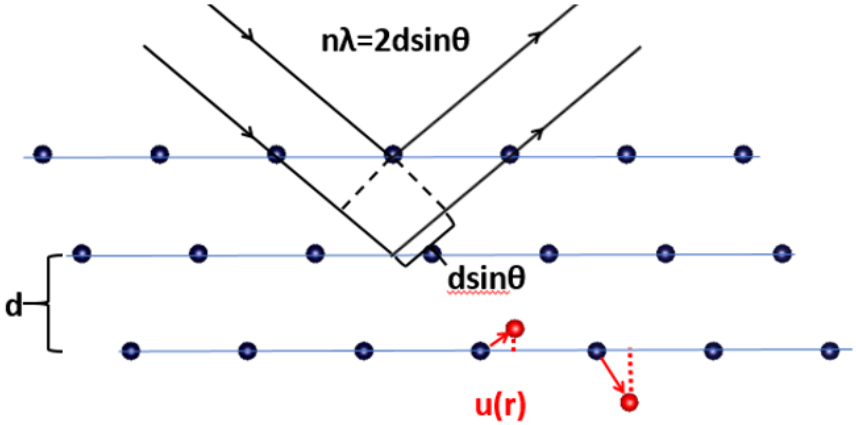

Figure 2.6: Schematic of Bragg scattering with labeled displacement field $u(\mathbf{r})$. Only changes from the ideal lattice positions along the direction of the scattering vector can be measured (this projection is noted by the dotted red line).

Phase shifts in the reconstructed complex density arise from strain (internal deformation) in the crystal lattice. The phase is proportional to the vector displacement field, $u(\mathbf{r})$, of the atoms from their ideal lattice points and the scattering vector $\mathbf{Q}$ via $\phi(\mathbf{r}) = \mathbf{Q} \cdot u(\mathbf{r})$.

It is important to note that since the displacement field is a vector field, we are only measuring the component projected along the wave vector So for example, measuring the (003) Bragg peak, which probes the **c** lattice spacing, means we will be measuring the displacement field projected in this direction (see Figure 2.6). In actuality we cannot measure the exact phase, only the *relative* phase, *i.e.* its derivative. The derivative of the projected displacement field yields a component of the strain field tensor.

The Lamé parameters are two material-dependent quantities (λ and μ) used in describing strain and stress. In the context of elasticity, μ is called the shear modulus and is sometimes denoted as G. In a homogeneous and isotropic material these define Hooke's law:

$$\sigma = 2\mu\varepsilon + \lambda \mathrm{tr}(\varepsilon)\mathbf{I} \tag{2.21}$$

where σ is the stress, ε is the strain tensor, and I the identity matrix. These two parameters parameterize the elastic moduli for homogeneous isotropic materials, and can be related to the other elastic moduli, e.g. the bulk modulus:

$$K = \lambda + 2/3\mu \tag{2.22}$$

The Poisson's ratio ν is the negative ratio of transverse to axial strain. It is the percent expansion divided by the percent compression for a small change.

For a cube stretched in the x-direction with a length increase ΔL in the x-direction and a length decrease of ΔL' in the y and z directions, the infinitesimal diagonal strains are given by:

$$d\varepsilon_x = \frac{dx}{x}, d\varepsilon_y = \frac{dy}{y}, d\varepsilon_z = \frac{dz}{z} \tag{2.23}$$

Integrating these expressions and using the definition of Poisson's ratio yields

$$-\nu \int_L^{L+\Delta L} \frac{dx}{x} = \int_L^{L-\Delta L'} \frac{dy}{y} = \int_L^{L-\Delta L'} \frac{dz}{z} \tag{2.24}$$

Solving this for very small values, to first-order, one obtains $\nu \sim \Delta L'/L$. The relative volume change of a cube can now be calculated using Lamé's relation $\nu \sim 1/2 - E/6K$ where K is the bulk modulus.

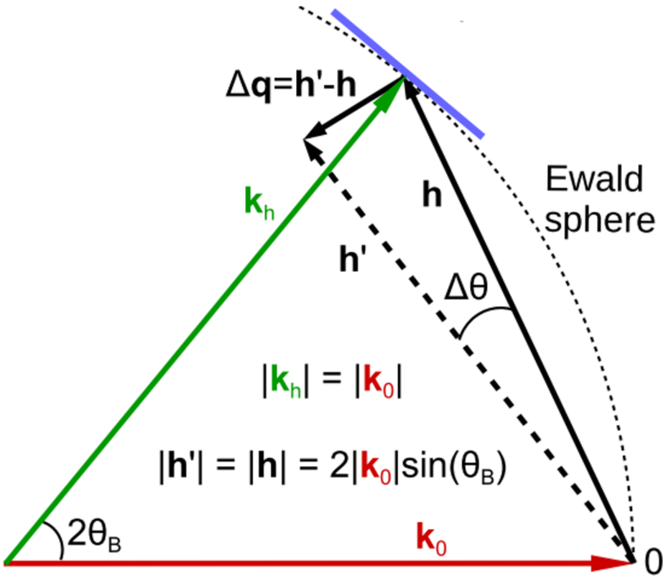

Figure 2.7: Collecting a rocking curve. By varying angular deviation from the Bragg condition different cross-sections through reciprocal space are accessed.

Chapter 3

Long-range displacement field in a lithium-rich layered oxide material $Li_{1.2}Ni_{0.133}Mn_{0.534}Co_{0.133}O_2$

3.1 Abstract

Surface disorder plays an essential role in guiding material properties, including in lithium-ion batteries. Lithium rich layered oxides (LRLO) are one of the most promising classes of cathode materials, delivering more than 50% capacity over leading commercial battery cathodes. However, progress has been hampered due to the voltage fading and capacity loss that occurs during the first cycle, and one of the main challenges is to understand how surface disorder and reactions affect battery performance. Here we use *operando* Bragg coherent diffractive imaging (BCDI) to reveal a striking three-fold rotational symmetry of the displacement field, corresponding to an average bending of the layers of 0.50 ± 0.25 Å. We find that this effect is drastically reduced or eliminated in two compositions of classically layered oxides (CLO), respectively. This finding illuminates the effects of surface strain on the bulk cathode physical

structure, and thus its effect on the overall battery performance.

3.2 Introduction

Presently, one of the most promising candidates for the next generation of lithium-ion battery cathode materials is the lithium-rich layered oxide $Li_{1.2}Ni_{0.133}Mn_{0.133}Co_{0.133}O_2$ (LRLO). It has an extraordinary high capacity of up to 320 mAh/g versus a practical capacity of ˜150 mAh/g for the commercial $LiCoO_2$ whose increase is a subject of active research in the battery community.[14,15,43,44] It has been pointed out recently that the enhanced capacity of the material stems from charge-compensation through the generation of localized electron holes on oxygen sites.[45,46]

The layered oxide structure consists of alternating transition metal (TM), oxygen and lithium layers. LRLO is a composite of $LiTMO_2$ and Li_2TMO_3 (see Figure 3.1a, b). The cathode surface plays an important role in rechargeable battery performance and lifetime.[47,48] The surfaces of pristine LRLO materials usually contain structural disorder such as antisite defects, transition metal segregation, surface reconstruction, and dislocations.[49–52] These types of disorder are strongly influenced by the exact composition and synthesis methods used.[43,53] Antisite defects such as Li/TM intermixing, for example, are the most prevalent form of disorder in layered cathode materials containing two-dimensional diffusion channels.[16,54–61]

All real materials contain structural defects which could significantly alter their properties, and whether that is a benefit or hindrance depends on the application and material in question. This only becomes more important as the length scale decreases. Much work has been done to characterize the surface of LRLO cathodes, and to explore the effects of surface phenomena on battery performance, but there is an open question as to how the bulk crystal structure is affected. We use *operando* Bragg coherent diffractive imaging (BCDI) to reveal a long-range rotationally symmetric bending of the displacement field in lithium-rich layered oxides which permeates the entirety of the crystal perpendicular to the crystal layers. This phenomenon is present during and after cycling, and drastically reduced in the classically layered oxide (CLO) $LiNi_{1/3}Mn_{1/3}Co_{1/3}O_2$. We connect the appearance and behavior of this symmetry to strain at the particle surface. This work clarifies the structural relationship between surface disorder and bulk battery performance, providing one more step towards understanding lithium rich layered oxide materials for next generation lithium ion batteries.

3.3 *Operando* 3D Imaging of three-fold symmetric displacement field

We performed *operando* Bragg coherent X-ray diffractive imaging (BCDI) to study long-range displacements and their dynamics in single lithium-ion battery cathode nanoparticles.[12,62,63]The method relies on measuring diffraction patterns while slightly rocking the crystal around the Bragg condition (see Figure 3.1h). A 3D diffraction pattern of a single Bragg peak is recorded and, when a coherent X-ray beam is used, the relative positions of the atomic planes are captured by the interference between coherently illuminated parts of the particle. The extreme sensitivity of Bragg diffraction to deviations from a perfect lattice allows the study of long-range displacements with sub-angstrom resolution. This technique is complementary to electron microscopy which yields images with high spatial resolution but tends to be unable to track variations in displacement field across large distances ($>$100 nm). All the data presented here was recorded with *in situ* cells similar to a number of our previous experiments.[53,64–66]

We measured 45 distinct crystals of CLO and LRLO cathodes in 7 *in situ* coin cells and 2 *ex situ* samples. Figure 3.1 shows typical recorded data of pristine CLO and LRLO nanocrystals as well as a 3D real-space reconstruction. In Figure 3.1c, e is the diffraction pattern as seen on the detector from a single point in the rocking curve measurement of CLO and LRLO, respectively. Taking an orthogonal slice and transforming to the lab frame as in Figure 3.1d, f corresponds to

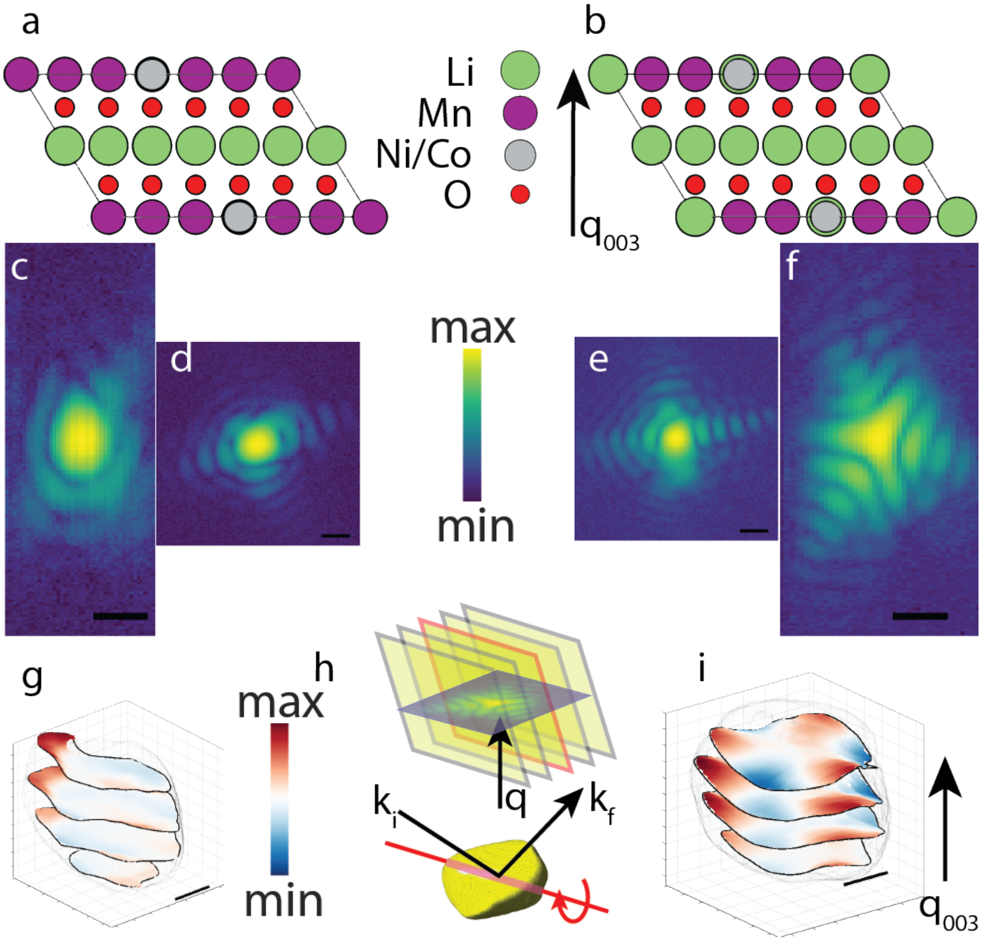

Figure 3.1: (a, b) The arrangement of atoms in lithium-poor (a) and lithium-rich (b) layered oxide materials. In (a) lithium is present only in the lithium layers while in (b) it also replaces a little less than half of the manganese sites. The unit cell is outlined in black. The directions of the measured scattering vector is also shown. (c, f) Rotated 3D diffraction data corresponding to a view perpendicular to the layers (and thus sensitive to interlayer spacing), for both CLO and LRLO, respectively. (d, e) Typical diffraction data as recorded on the detector for both CLO and LRLO, respectively. (g, i) 3D reconstruction of the CLO and LRLO diffraction patterns, respectively. The slices are of the displacement field, and the bending is exaggerated for greater visibility. See Supplementary Movies 1 and 2 to see them from different angles. The scale bars are 100 nm. (h) Sketch of experimental geometry, with the orientation of the slice (f) shown relative to the collected rocking curve and scattering wavevector. The scale bar is 0.05 nm^{-1}.

a view perpendicular to the crystal layers. In the case of LRLO it reveals rotational symmetry of the diffraction patterns suggesting minute distortions from an ideal crystal lattice. In general, perfect strain-free crystals produce symmetric diffraction patterns due to Friedel's law, with the number of truncation rods equal to the number of crystal facets. In the pristine state the

CLO diffraction patterns resemble nearly perfect crystals (see Figure 3.1c).[67] Only after looking closely at the reconstruction is there a discernible bending. The diffraction pattern from a pristine LRLO nanocrystal (see Figure 3.1f) is dramatically different. It lacks inversion symmetry, and instead shows a clear three-fold rotational symmetry in a direction parallel to the layers. The lack of inversion symmetry indicates substantial long-range displacement fields (see Supplementary Figure 3.4). The geometry of the different slices through the diffraction pattern is sketched in Figure 3.1h.

To understand the origin of the asymmetry or lack thereof of the diffraction pattern shown in Figure 3.1c, f we performed an iterative phase retrieval with a genetic breeding algorithm to determine the 3D displacement field of the measured LRLO nanoparticle (see Figure 3.1g, i and Figure 3.2a, c as well as Supplementary Movies 3.17, 3.18).[40,68] The complex valued representation of the particle is given by:

$$s(\mathbf{r}) = e^{i\mathbf{q}\cdot u(\mathbf{r})} \tag{3.1}$$

where $s(\mathbf{r})$ is the shape of the particle, $u(\mathbf{r})$ is the local displacement of the layers along the scattering vector $\mathbf{q}$, and $\mathbf{r}$ is the position within the particle. Due to the experimental geometry here, $u(\mathbf{r})$ describes the local displacement of the crystal normal to the layers of the crystal structure (along the direction of the measured (003) Bragg peak).

The shape of the particle $s(\mathbf{r})$ resembles a platelet with a height of 200 nm and a width of 400 nm (see Figure 3.1i and Supplementary Movie 3.17), consistent with observations in scanning electron microscopy from our previous work.[53] The 3D displacement field $u(\mathbf{r})$ inside the particle is also shown in Figure 3.2a, c. As already expected from the data, the displacement field is not uniform and shows a striking three-fold rotational symmetry reminiscent of a monkey saddle shape and akin to that observed in the measured diffraction pattern (see Figure 3.1i).[63,69] In Supplementary Figure 3.5, multiple slices through the particle reveal that the displacement field does not vary significantly as we move along the (003) direction. Consequently, the strain field (local spacing between layers) is relatively small, on the order of 0.02% (see Figure 3.2b). It is worth noting that the strain field does not show the same symmetry, but rather shows domains with alternating compressive (green) and tensile (purple) strain.

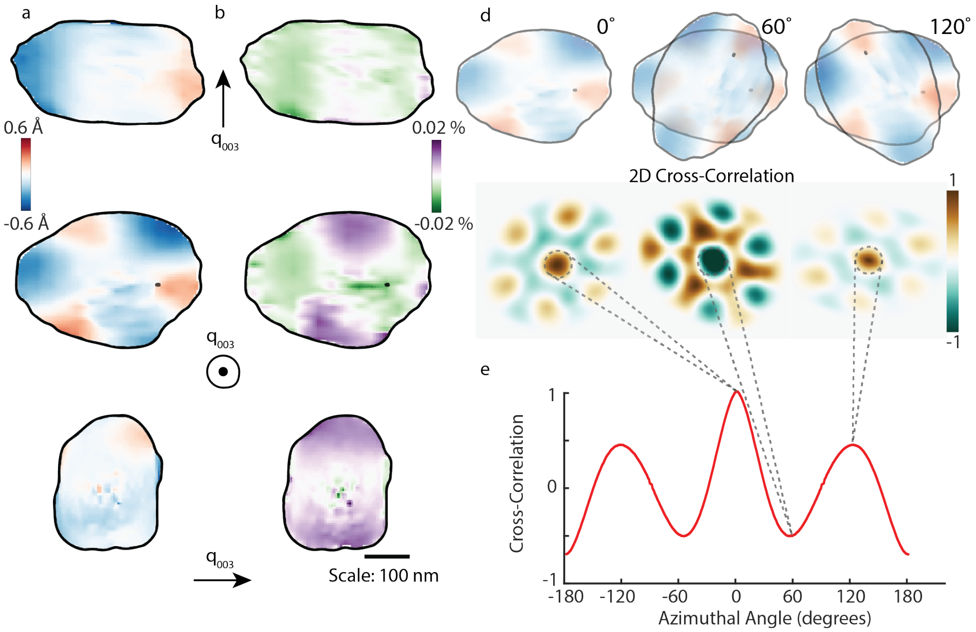

Figure 3.2: (a,b) Slices through the 3D representation of a single LRLO battery crystal in three orthogonal slices through the center of the particle. Each slice is an average of 5 images, or approximately 10% of the particle. The direction of **q** is indicated for each slice. Black lines represent the boundaries of the particles as determined by the amplitude, and the scale bar is 100 nm. (a) The displacement and (b) strain field for the ε_{zz} component of the strain tensor. (c) The central slice of (a), which is perpendicular to the layers of the crystal lattice, was used to create the 2D rotational cross-correlation. (d) The central peak of each 2D cross-correlation pair was plotted as a function of rotation angle. The origins of three data points are shown for clarity. The periodicity with alternating high levels of correlation and anti-correlation indicates a strong three-fold structural symmetry.

We performed 2D rotational cross-correlation analysis in order to quantify the level of symmetry in the 63 separate rocking curves of both CLO and LRLO that were measured and reconstructed. For each 3D dataset, we took a slice corresponding to an averaged 10% of the central portion of the particle perpendicular to the layers. This was used to perform a cross-correlation as a function of rotation as shown in Figure 3.2d (see Supplementary Movie

3.19). We plotted the central peak of the cross-correlation as a function of azimuthal angle to generate the plot seen in Figure 3.2e. This is shown for a number of CLO and LRLO nanoparticles in Supplementary Figures 3.6 and 3.7, respectively. The change in the central value of the rotational 2D cross-correlation in Figure 3.2d shows three peaks, matching the three-fold rotational symmetry of the displacement field.[70,71] Each plot of central correlation was fit with a sinusoid to quantitatively compare the CLO and LRLO displacement fields and confirm that only LRLO crystals, on average, contain a strong three-fold symmetry (see Supplementary Figure 3.8). However, it should be noted that many of the CLO crystals also have a bending in the displacement field, but with a drastically reduced magnitude.

We utilized the *operando* capabilities of our setup to track the structural evolution of individual particles during electrochemical cycling. Figure 3.3 shows selected scans from a single LRLO nanoparticle cycled at a rate of C/5. For reasons of clarity the remaining scans are shown in Supplementary Figure 3.9. Slices of the displacement field shown in Figure 3.3a clearly indicate that the displacement field pattern persists throughout charge and discharge. *Ex situ* measurements of other LRLO crystals after 1 or 50 cycles demonstrate that this long-range displacement field also remains after cycling (see Supplementary Figure 3.10).

The strain field maintains a relatively low value below 0.1% in the bulk of the structure, only rising to extreme highs and lows near dislocation cores (see Figure 3.3b).[53] We also track the average **c** lattice parameter of the crystal as well the level of symmetry as defined in Figure 3.2d. These are plotted as a function of lithium concentration along with the voltage profiles (see Figure 3.3c, d). Lastly, we characterize the change in the surface area of the particle, and find that it shows the same pattern as our metric for symmetry (see Supplementary Figure 3.11).[73]

There is an above-average level of strain near the surface of the particle (see Supplementary Figure 3.12a). When charged to 4.44 V, immediately before the voltage plateau, the symmetry is almost fully suppressed. Upon discharging to 3.60 V it has largely recovered (see Supplementary Figure 3.12b). The symmetry-breaking coincides with an increase in dislocation density seen as

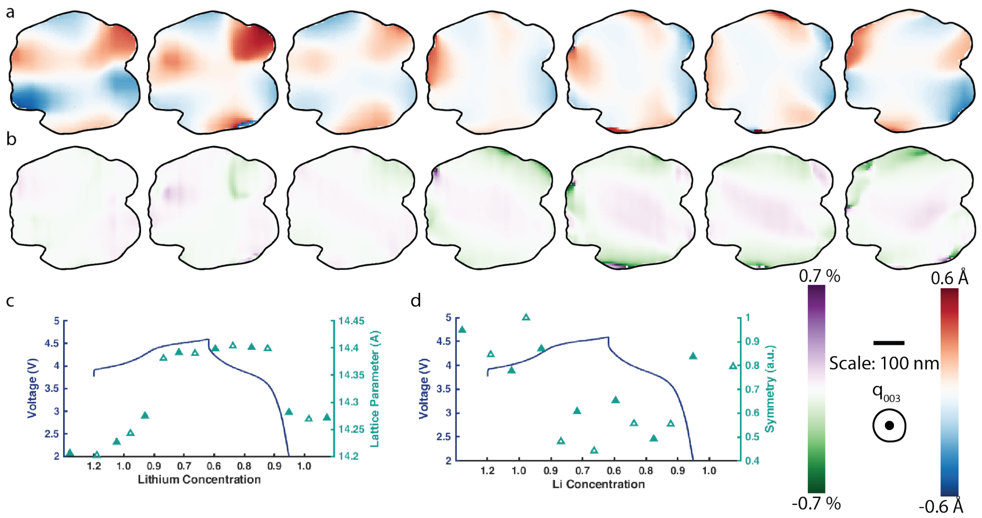

Figure 3.3: A single LRLO battery nanoparticle was measured *operando* during a full charge and discharge. Shown are central slices of the (a) displacement and (b) strain fields perpendicular to **q** as a function of voltage. When one discounts the effects of dislocations, the strain field remains very small in this particle, on the order of 0.1-0.3% throughout the measurements. These scans are shown as filled triangles in (c, d). Not all scans are shown in (a, b) for brevity. See Supplementary Figure 3.9 for the rest. (c) The measured voltage and **c** lattice parameter are plotted as a function of lithium concentration, along with the cycler voltage. The values agree with bulk neutron diffraction data on the same material.[72] (d) The absolute sum of the correlation is plotted vs. lithium concentration.

dislocation glide from the particle edge into the bulk (see Supplementary Figure 3.12c).[53] It also coincides with a drop in the surface strain. The dislocation density and mean surface strain do not reset upon discharge and are left at an elevated state. When comparing this material to our CLO, we do not find the presence of any significant long-range displacement field symmetry.

The retrieved displacement fields can be understood as follows: The displacement field $u(\mathbf{r})$ from Equation 3.1 is the relative shift of the local part of the crystal with respect to a perfect crystal lattice, *i.e.* the red (blue) regions in the images of displacement fields are layers shifted towards (away from) the normal to the layers. The pattern of this displacement field means that layers are bent in an alternating manner, shifting up and down along an azimuthal coordinate. A lack of strong strain fields mean that adjacent layers must follow the same displacement path, and that all layers have a similar level of bending. The *operando* reconstruction and diffraction data demonstrate persistence of this displacement field: fully extracting almost all lithium and then intercalating does not change the symmetry of the data and thus the symmetry of the displacement field and layers. The displacement field within LRLO crystals, on average, is 0.5 ± 0.25 Å in magnitude, with a bending of the lattice planes of roughly 1 mrad.

3.4 Discussion

The mechanism by which surface disorder affects bulk electrochemical properties in LRLO is poorly understood. Although defects typically connote low performance or stability in many materials, a number of works have shown that cation intermixing may actually be beneficial in some cases for bulk structural stability and reversible capacity.[43,57,74–76] These antisite defects are believed to concentrate on crystallographic facets perpendicular to the layers, in the direction of lithium diffusion, and play a role in the surface reconstruction.[60,77,78] For example, a stable spinel crystal structure of 1-3 nm has been measured in pristine LRLO matching the chemistry we used in our work. There is no consensus on whether in this case the surface layer plays a role in protecting the surface from corrosion and degradation or has in fact the opposite effect.[76,79–81]

In most LRLO materials, the first charge is accompanied by oxygen gas evolution. This creates many oxygen vacancies at the surface, along with oxidizing Mn^{3+} to Mn^{4+}. The oxygen loss at the surface may be irreversible, and a number of side products are able to form on the surface through reactions between oxygenated species and the organic electrolyte. In discharge, some of the oxygen vacancies and Li vacancies are removed due to TM migration to the vacant sites in what is called structural densification, or the surface structural evolution from a layered structure to a spinel- or rock salt-like structure.[47,49,81,82]

The LRLO displacement field pattern remains present in the pristine state, in all states of charge, as well as after cycling. X-ray beam damage effects are ruled out by comparison to *operando* powder diffraction data (see Supplementary Figure 3.13). The absence of the symmetric layer bending in the lithium-poor CLO, which is synthesized by the same method, suggests that it cannot be due to specific details of the synthesis. This phenomenon is thus likely a fundamental property of the material and its composition. As another major difference between the two types of cathodes was the size distribution of our measured crystals ($1.85 \times 10^7 \pm 0.80 \times 10^7$ for LRLO, vs. $7.82 \times 10^6 \pm 5.19 \times 10^6$ for NMC), we fit a L_1-regularized logistic regression classifier without using volume as an input to ensure we were not seeing a size-related effect (see Supplementary Table 3.1).[83]

We argue that this symmetric wrinkling of the layers is due to the measured strain field localized to the surface. This strain field is on crystal facets perpendicular to the layers, just like the symmetric displacement field. The changes of the surface strain also coincide with changes in total layer bending. Pristine CLO cathode particles contain a lower surface strain, as expected.

BCDI can image the strain fields created by a single point defect in a near-perfect crystal.[84] A concentration of defects of similar type in LRLO can modify the strain landscape to a much larger degree. The surface strain field in LRLO can be explained by the effects of antisite defect segregation. LRLO has been shown to form a concentration of primarily Ni and some Co antisite defects at the (200) crystallographic facets, *i.e.* perpendicular to the layers. CLO, in contrast, has a relatively higher concentration of nickel and is expected to form fewer Li/Ni antisite defects at these facets, thus containing a much-reduced long-range displacement field, also matching our observations.[47,79]

The defects at the crystal surface form a spinel-like structure that may act as a fixed boundary condition during particle growth. In this case the crystal layers must bend out-of-plane in an alternating fashion to prevent in-plane compression, analogous to the growth of a leaf.[85–88] As the bending rigidity is much smaller than their stretching rigidity, the layers can easily buckle or wrinkle into shapes that remove in-plane compression.[89] A similar displacement field phenomenon has been shown to occur in several core-shell structures and has been ascribed to primarily epitaxial strain effects.[63,90]

Given this boundary condition, if the intralayer lattice spacing were to decrease, then the crystal could relax to a new equilibrium with reduced bending of the layers. The measured decrease and subsequent increase in the layer bending while cycling coincides with intralayer lattice contraction and then expansion in our LRLO material.[61]

Previously, it was known that the surface layer effects battery performance, but there was a question as to how it affected the bulk structure. We found that strain at the surface forms a displacement field that extends through the entire particle. The location of the strain matches with the effects of a concentration of facet-dependent antisite defects. This displacement field adds a new aspect to the complicated physics of this technologically relevant material and elucidates the role of surface disorder in the bulk crystal structure.

3.5 Acknowledgements

We thank Dr. Ivan Zaluzhnyy for discussion on statistical analysis techniques, Dr. Daniel Ben-Zion for assistance with the implementation of phase unwrapping methods, Professor Daniel Arovas for discussion on possible atomic deformation mechanisms, and Dr. Peter Sprau for discussion on how to characterize the displacement field bending.

3.6 Supplementary Information

Supplementary Figure 14: Scanning electron microscopy of cathode materials.

Supplementary Figure 15: Phase retrieval transfer function (PRTF). The resolution of a reconstruction can be quanitifed using the PRTF.

Chapter 3, in full, is currently being prepared for submission for publication of the material. The dissertation author was the primary investigator and author of this paper. Thanks to my co-authors A. Singer, S. Hy, A. Shabalin, C. Fang, M. Zhang, A. Ulvestad, J. Wingert, N. Hua, S. Hrkac, H. Liu, R. Harder, E. Maxey, J. Masser, Y. S. Meng, and O. G. Shpyrko.

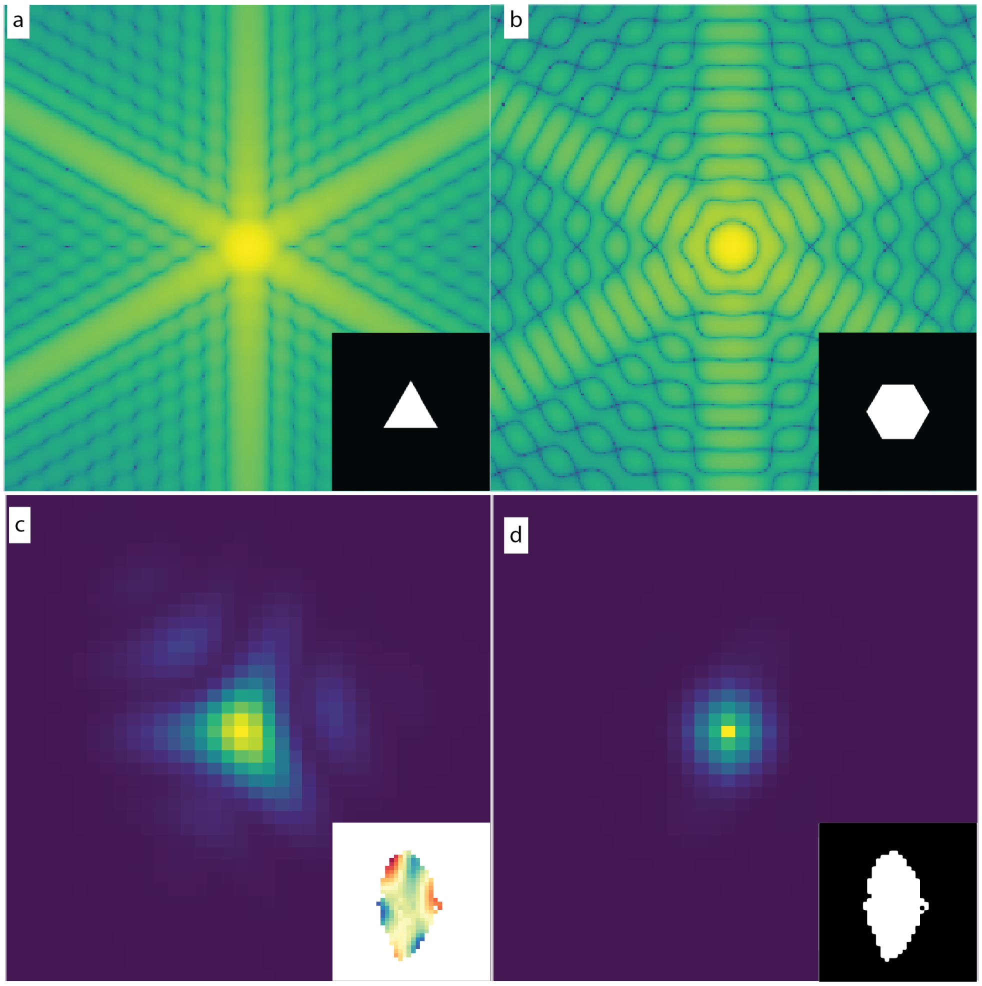

Figure 3.4: A strong symmetry in the diffraction pattern translates directly to a symmetry (whether in shape or in phase) in real space. Normally, a strain-free crystal with hexagonal facets would have six truncation rods (one for each facet) emanating from the central Bragg peak. However, in the case of a three-fold symmetric phase that passes through the crystal, its diffraction pattern would have a three-fold rotational symmetry. (a) The Fourier transform of a triangle, with the triangle shown as inset. (b) The Fourier transform of a regular hexagon, with the shape shown as inset. (c) The Fourier transform of an individual reconstruction slice of the same LRLO particle shown in Figures 3.1 and 3.2. (d) The Fourier transform of the same particle slice after setting the phase to zero, with the shape shown as inset. Note how the diffraction has lost its three-fold symmetry from (c).

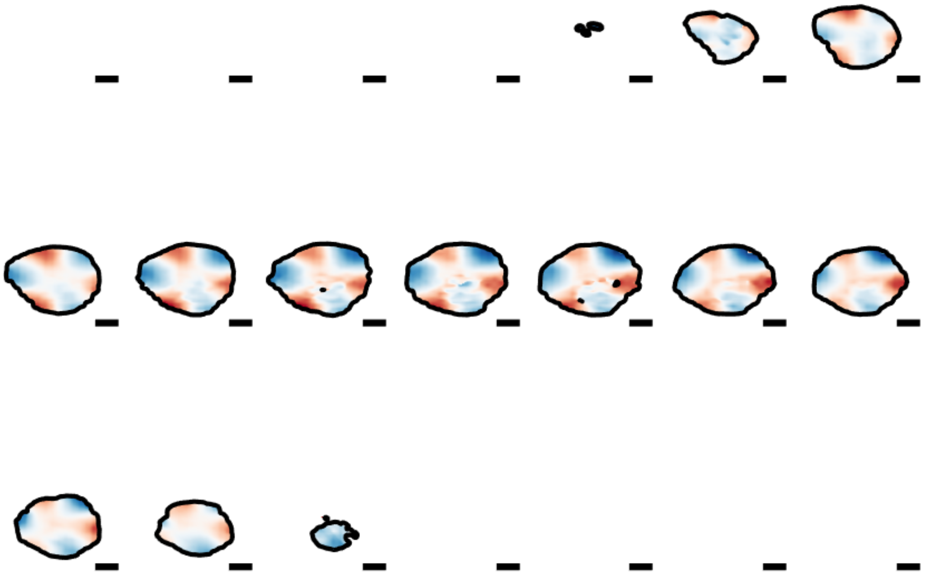

Figure 3.5: Shown are every fifth slice of the 100×100×100 displacement array of the particle measured *operando*. These are from the first scan (in the pristine uncharged state). The direction of the scattering vector **q** is shown, the scale bar is 100 nm, and the displacement field ranges from -0.6 Å to 0.6 Å.

Table 3.1: Standardized coefficients (Z or β scores) of L_1-regularized logistic regression binary classifier for the type of cathode material. The particle volume was removed from the list of terms as the size distributions for each cathode is quite different ($1.85 \times 10^7 \pm 0.80 \times 10^7$ for LRLO, vs. $7.82 \times 10^6 \pm 5.19 \times 10^6$ for NMC), and we wanted to ensure that this was not a size-induced effect. The variables were normalized prior to fitting.[83] There were 63 different datapoints measured, for 42 unique nanocrystals. The model reaches an accuracy of 93%. A Z-score greater than 2 in absolute value indicates statistical significance at the 5% level.

Term	Z score	Coefficient	Standard Error
Sum of displacement field:	101.07	18.44	0.18
Elastic energy density:	27.30	5.45	0.20
Absolute magnitude of strain:	-24.63	-7.54	0.31
Absolute magnitude of correlation:	12.06	2.86	0.24
Standard deviation of correlation:	9.05	2.14	0.24
Dislocation density:	-3.82	-0.74	0.19
Frequency of correlation curve:	3.64	1.27	0.35

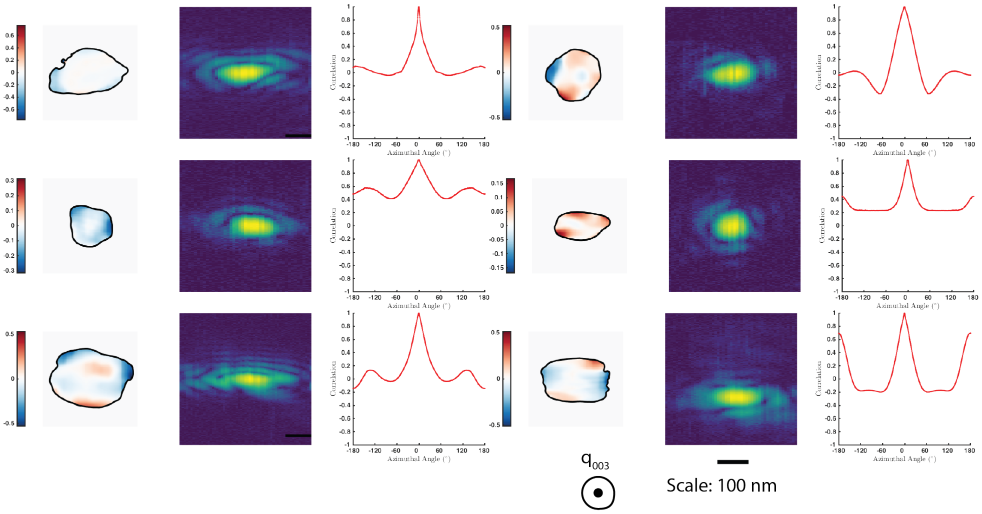

Figure 3.6: Each series of plots shows a reconstruction of a different pristine NMC particle measured *in situ* (the same averaged central slice orthogonal to the layers shown in Figure 3.3) in addition to the corresponding slice in reciprocal space. Also shown is the central peak of the 2D rotational cross-correlation as a function of rotation angle, which is a quantitative measure of the level of symmetry for each crystal. The scale bar for the reconstructions is 100 nm, and for the diffraction patterns 3 nm^{-1}. The cross-correlation is normalized to a maximum of 1.

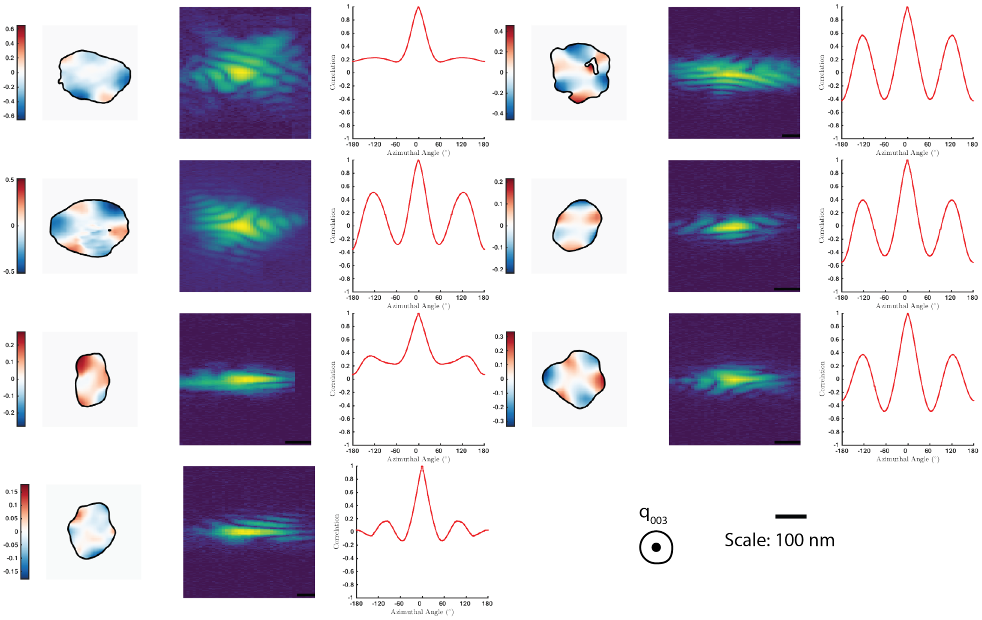

Figure 3.7: Each series of plots shows a reconstruction of a different pristine LRLO particle measured *in situ* (the same averaged central slice orthogonal to the layers shown in Figure 3.3) in addition to the corresponding slice in reciprocal space. Also shown is the central peak of the 2D rotational cross-correlation as a function of rotation angle, which is a quantitative measure of the level of symmetry for each crystal. The scale bar for the reconstructions is 100 nm, and for the diffraction patterns 3 nm^{-1}. The cross-correlation is normalized to a maximum of 1.

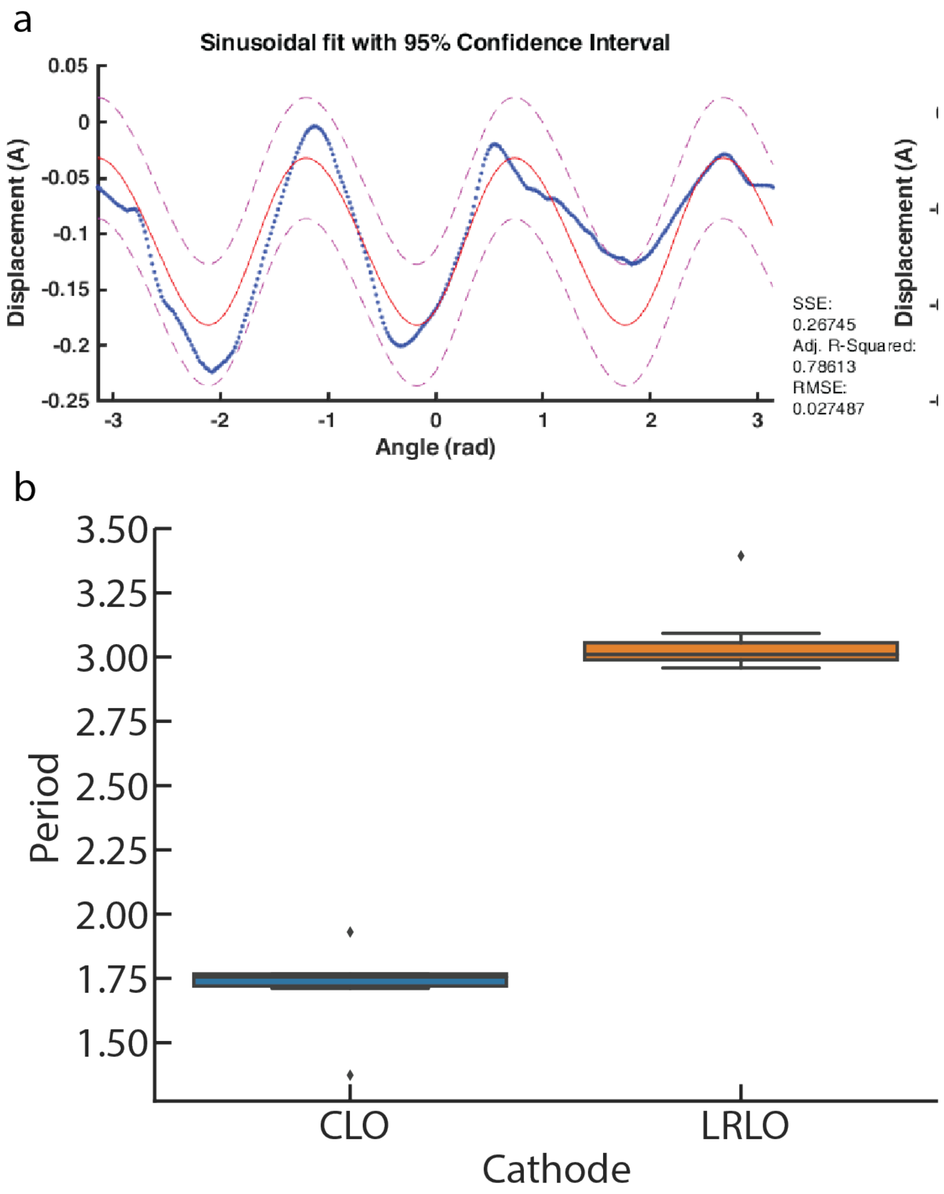

Figure 3.8: (a) The cross-correlation images were averaged along the radial direction, and the resulting curve fit with a sinusoid. (b) The periodicity of the CLO is significantly lower or non-existence, reflecting the reduced strength of the displacement field bending.

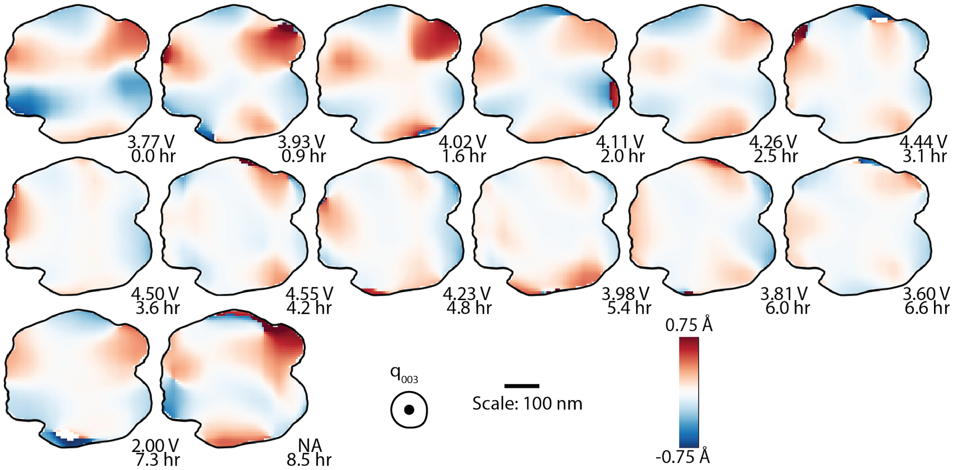

Figure 3.9: The long-range displacement field as a function of charging time. All the measurements for the crystal shown in Figure 3.3, with the voltage and time since the start of charging labeled. The last value is after cycling has ended, and the particle has had a chance to relax.

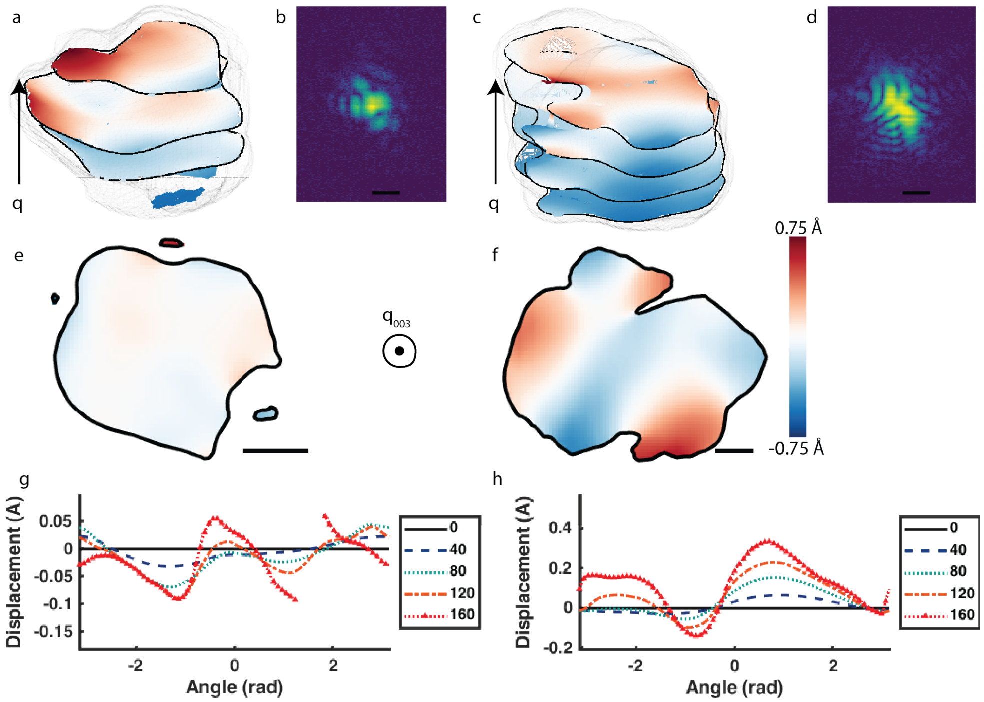

Figure 3.10: We measured several *in situ* 1× cycled and 50× cycled particles, with the best diffraction patterns reconstructed and shown here. The 50× cycled particle is shown in the left column, while the 1× cycled particle is shown in the right column. (a) A 3D view of each crystal along with a slice through the diffraction pattern showing the characteristic symmetry. (b) An averaged 10% of the particle through the center, with the reconstruction corresponding to the diffraction slice in (a). The scale bar is 100 nm and the displacement field ranges from -0.75 Å to 0.75 Å. (c) "Unwrapping" the image in (b). (d) Displacement along circles of successively larger radii about the geometric center of the slice in (b). (e) Two linescans from the particle center to edge, for the largest positive and negative changes in displacement field, respectively.

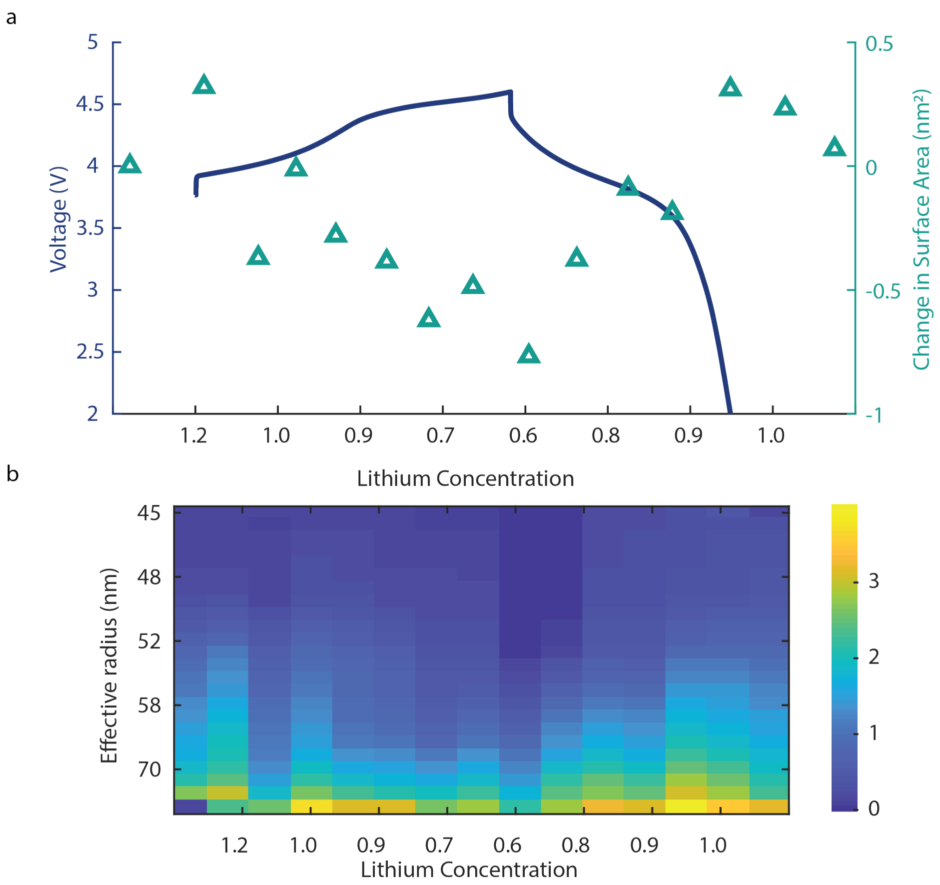

Figure 3.11: A Delaunay triangulation was used to parametrize the surface of a slice containing an averaged 10% of the particle. This was used to calculate the surface area. (a) The change in surface area as a function of lithium concentration. It decreases and then recovers in discharge. Also shown in the voltage profile of the cell containing the measured particle. This image is an average for the range of thresholds 0.05–0.15, which is a range typically used in BCDI experiments to define the particle surface. (b) Each vertical slice of all the image is taken from an individual scan during cycling. The amplitude, which represents the electron density, is used to determine the particle shape. Each "radius" on the y-axis differs by 0.01 in the amplitude threshold and as the particles are not spherical, is only approximate. The colorbar values are in nm.

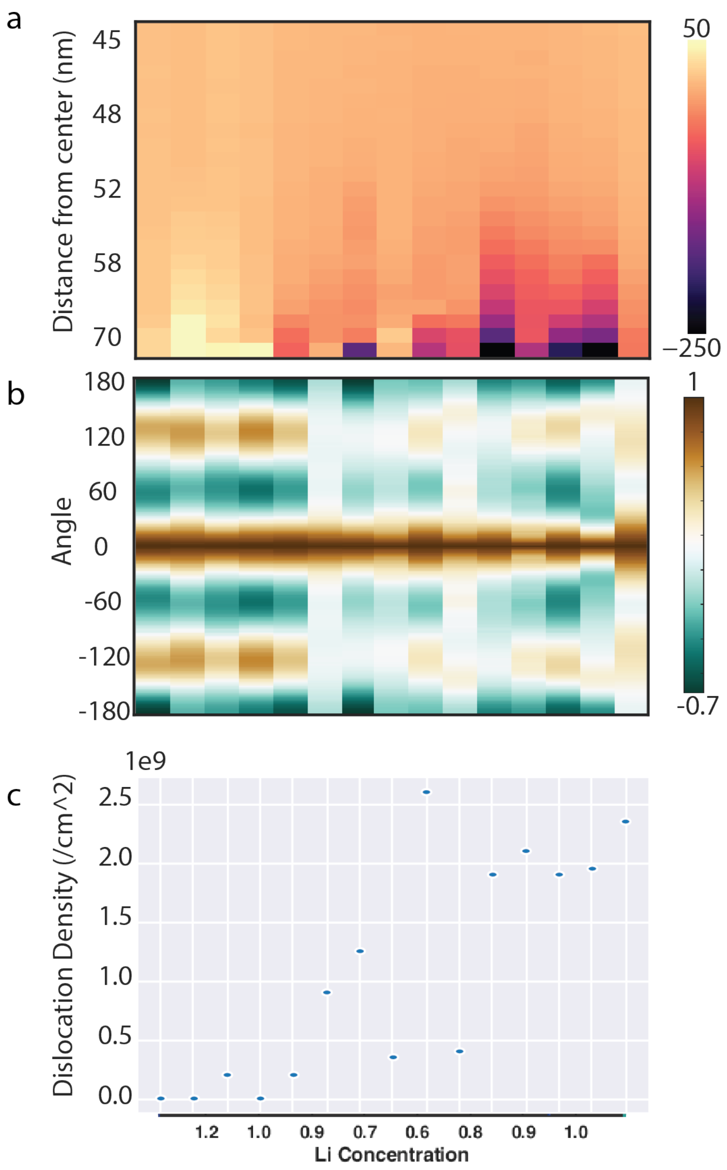

Figure 3.12: Each vertical slice of all three images is taken from an individual scan during cycling. (a) The surface strain depresses shortly before the voltage plateau. The surface strain was calculated by summing the strain for shells of differing amplitude threshold. The amplitude, which represents the electron density, is used to determine the particle shape. Each “radius” on the y-axis differs by 0.01 in the amplitude threshold and as the particles are not spherical, is only approximate. The values are calculated as strain per cubic micron. (b) The magnitude of the displacement field bending is suppressed just before the voltage plateau and recovers in discharge. Each vertical slice is calculated by taking the 2D rotational cross-correlation and averaging it radially. The colorbar values are in nm. (c) The dislocation density also shifts at about the same voltage, although the value remains high at the end of discharge.

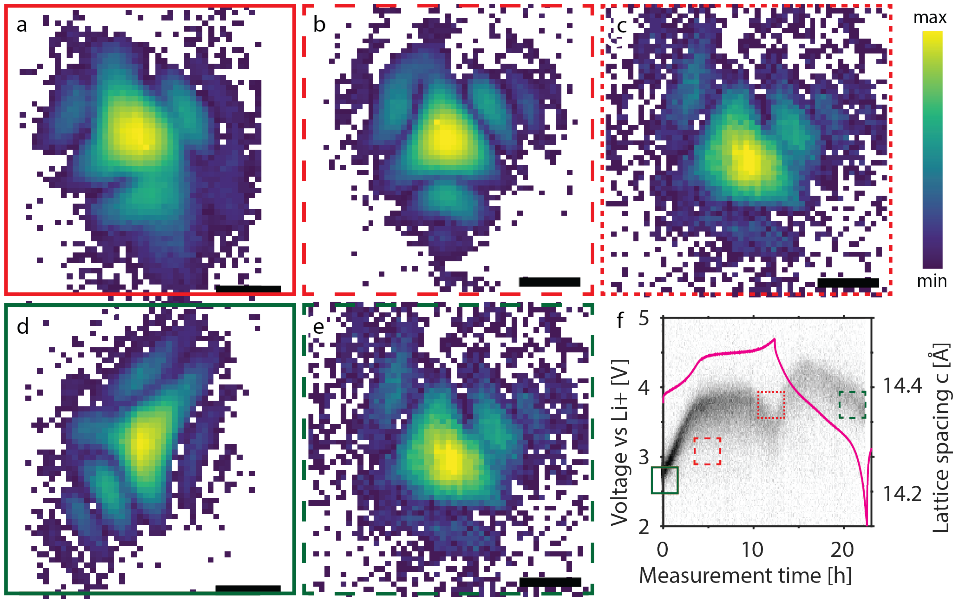

Figure 3.13: 3D diffraction data of two different particles from two separate coin cells, both cycled at C/10. (a-c) A crystal measured (a) in the pristine state, (b) charged to 4.3 V, and (c) at 4.7 V. (d-e) A second particle was measured at the pristine and after a full cycle. (f) Ensemble powder diffraction data showing the evolution of the average lattice constant of an *operando* coin cell is shown in black. The lattice constants of the single particle measurements from (a-e) are also indicated with outlines of matching color and pattern. Voltage profile of the *operando* cell used in the experiment is shown in red. We observed that the structure is extremely robust towards X-ray radiation in the pristine state (we have measured data for 5 hours without noticeable changes in the diffraction). However, it was typical to observe significant radiation damage upon repeated measurements at a high state of charge, particularly for voltages above 4.5 V. The extreme sensitivity of the structure to X-ray radiation above 4.5 V is a measure of the strength of atomic bonds in the structure and is attributed to the loss of oxygen above 4.5 V.[45] Above this potential, continuous measurement of a particle often led to noticeable radiation damage and had to be performed carefully. The corresponding flux is estimated to be on the order of 1e9 photons, whereas in the pristine state more than 1×10^{10} photons did not induce any damage. To confirm that our crystals were undamaged by the X-ray beam, we compared the average lattice constant over time with *operando* powder diffraction measurements and found them to agree.

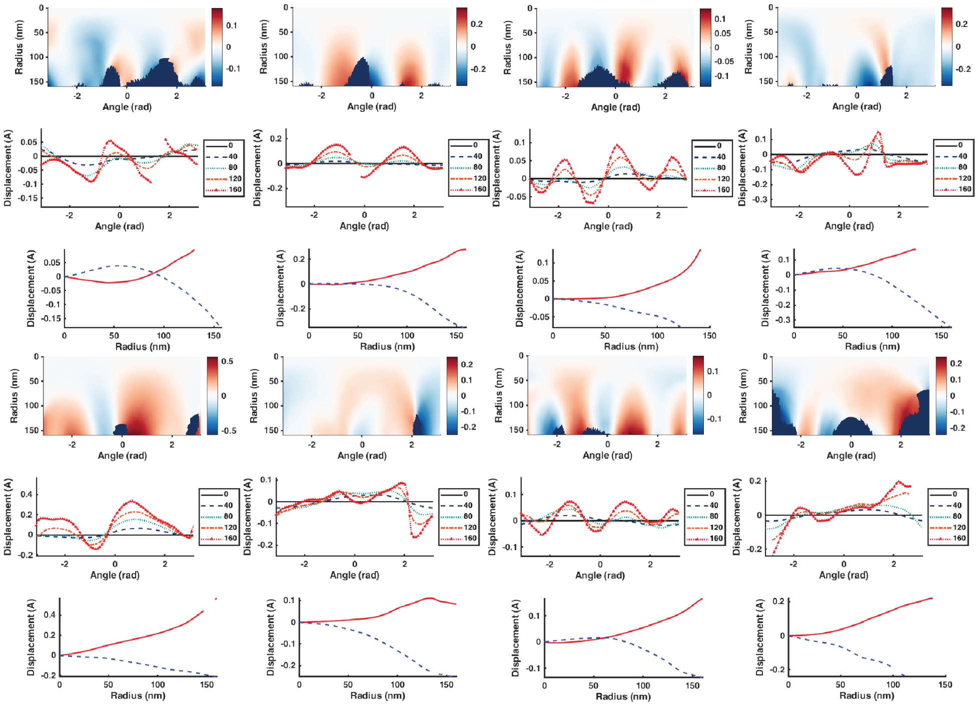

Figure 3.14: Two plots and an image are shown for nine different LRLO nanoparticles. The top image is of the central section corresponding to a direction perpendicular to the crystal layers, but radially "unwrapped" to plot the distance from the center vs. the azimuthal angle around the particle. The central plot shows five horizontal line cuts from the first image.

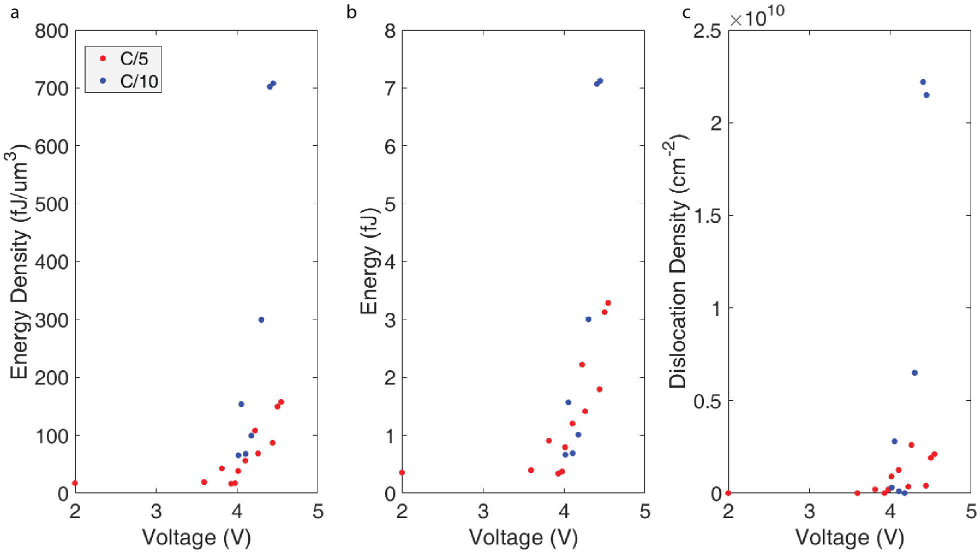

Figure 3.15: These plots all derive from the same series of scans for the crystal shown in Figure 3.3, as well as data from Singer et al.[53] The (a) partial elastic strain energy density, and dislocation density are all plotted. There is a general increase in strain energy as expected. However, at a cycling rate of C/5 lithium diffusion dynamics are too fast to allow the movement of dislocations into the particle, which has been seen only when cycling at a rate of C/10.

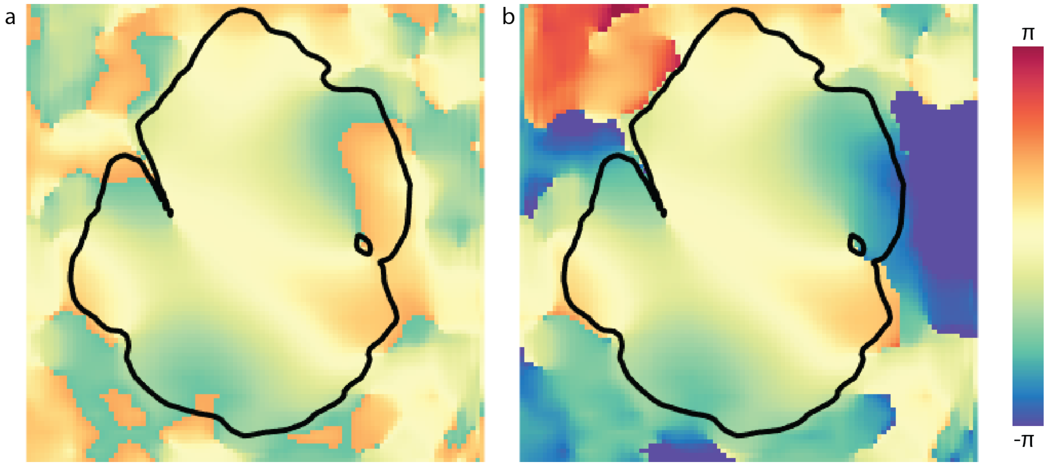

Figure 3.16: We make use of a quality guided phase unwrapping algorithm to remove phase wraps that would incorrectly change our phase abruptly from π to −π due to how phase is defined and visualized.[91] (a) is the original unwrapped phase image, with a particle shape contour shown to note the region of interest, and (b) is the unwrapped final image, where phase now changes continuously within the particle. Note that dislocations such as the one appearing within the phase singularity are not removed, as expected.

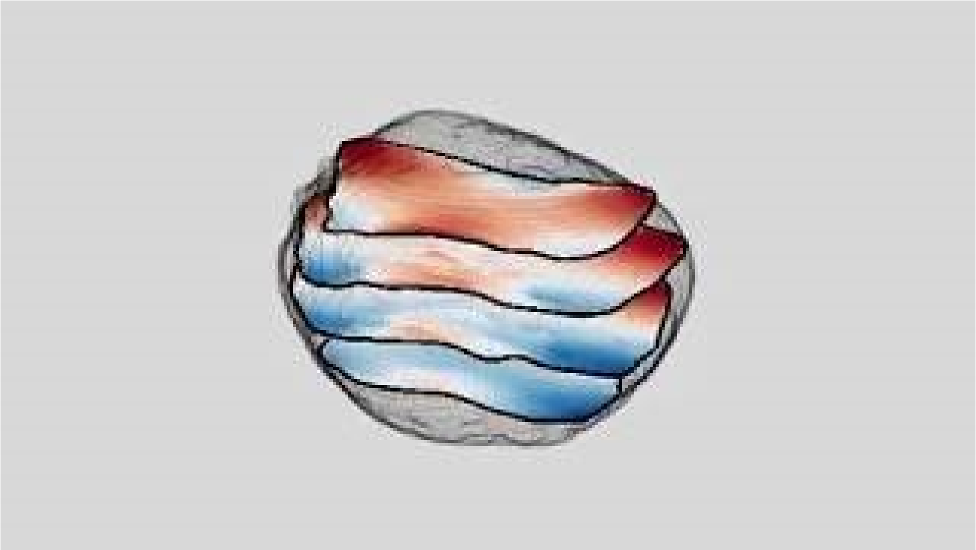

Figure 3.17: https://youtu.be/51B5ZOiUSqo.

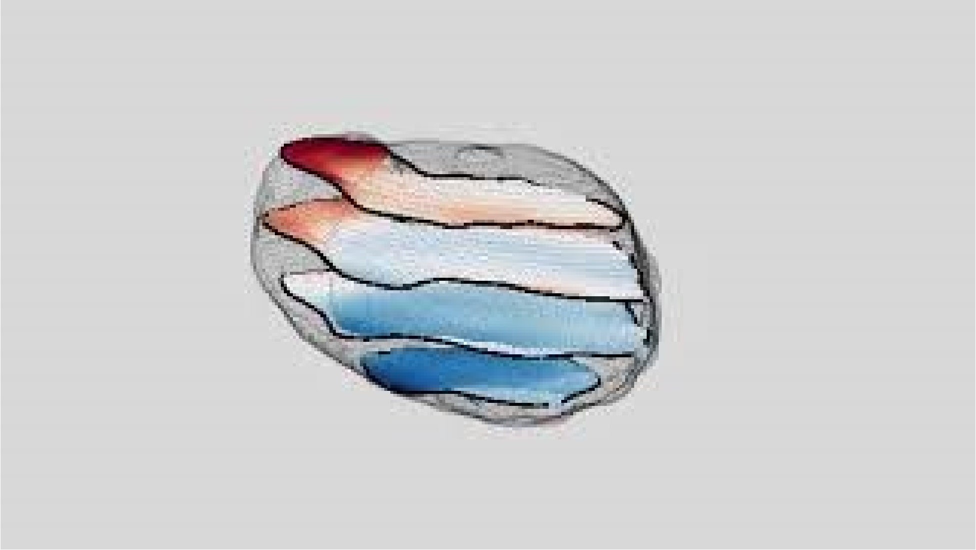

Figure 3.18: https://youtu.be/N9aXbrncUuA

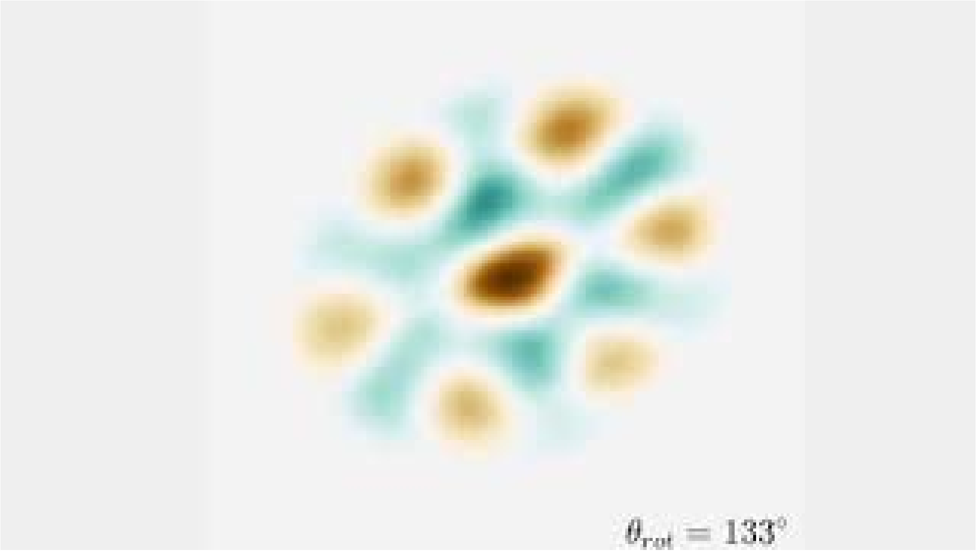

Figure 3.19: The entire 2D rotational cross-correlation matrix, shown one degree at a time https://youtu.be/ddkAqRWVGP4

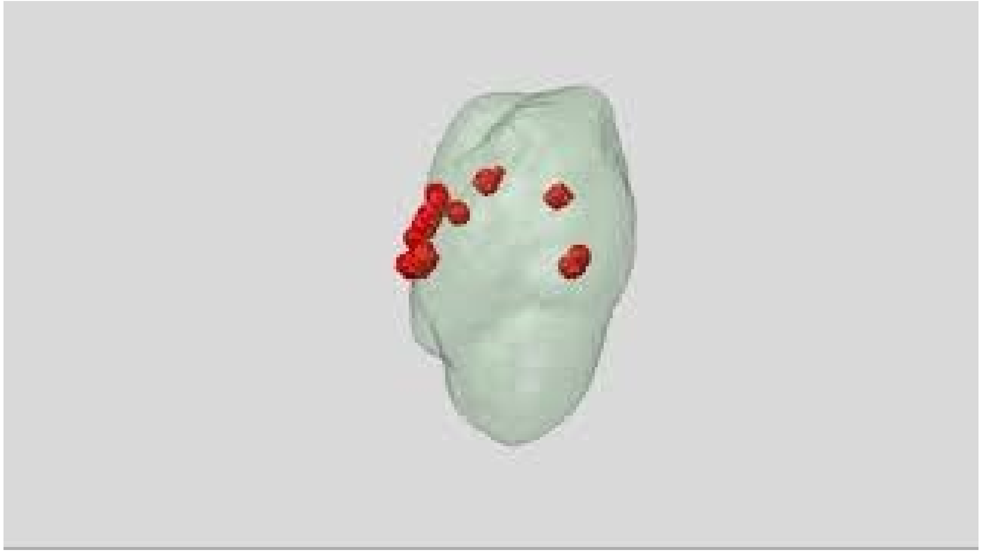

Figure 3.20: We follow the procedure outlined in Clark et al. to identify line dislocations within the crystal.[92] This video shows one step of this process. https://youtu.be/31Bdsnx_RKc

Chapter 4

Nanoscale differences in strain and defect density as a function of annealing conditions in $LiNi_{0.8}Co_{0.15}Al_{0.05}O_2$

4.1 Abstract

Li-ion batteries are highly prevalent in personal electronics, as well as electric vehicles. Layered $LiNi_xCo_yAl_zO_2$ (NCA) with $x+y+z=1$ is a cathode material with very high specific capacity that has yet to reach its theoretical limit. Structural disorder is known to play an important role in its electrochemical properties. In turn, many types of disorder such as microstrain and line and point defects are affected by annealing, and this disorder dictates final device functionality. Bragg coherent X-ray imaging (BCDI) is used to image the strain and displacement fields in pristine nanoparticles made by annealing a hydrothermally-grown hydroxide precursor. We compare the strain features caused by defects as well as dislocations for two different annealing conditions in pristine crystals. We observe that while the overall strain is reduced with a longer anneal time, the density of dislocations remains just as high.

4.2 Introduction

One of the critical challenges in transitioning to a renewable-energy economy is the move away from fossil fuel-powered vehicles. An estimated over one billion motor vehicles were in use in 2010, with predictions of over two billion by 2020.[8] Li-ion batteries with high energy density, good rate capability, long cycle life and low cost will be needed for making this transition.[8,11,93] NCA is a commercialized battery cathode material with a structure composed of alternating lithium and transition metal (TM) layers. Interest in this material is driven by its high theoretical specific capacity of 279 mA h g^{-1}.[94–100] Indeed, variants of the material have been successfully commercialized, such as in Panasonic batteries for Tesla EVs.[101] NCA has been shown to undergo several different degradation mechanisms under various operating conditions.[18] In order to reach higher capacities or energy densities, cycling beyond 4.1–4.2 V vs. Li^+/Li^0 is necessary. However, oxidation of the electrolyte occurs at these higher voltages, which induces the formation of disordered rock-salt domains on the surface of the NCA, causing impedance growth.[102] In addition, cracks within the secondary particles have been observed when charged to a voltage $>$ 4.5 V and/or under the condition of a wide depth of discharge range that induces high strain.[18,103] A better understanding of the strain will help with the design, synthesis and defect engineering of NCA. Observations of differences with modified synthesis conditions and changes that come with increased cycling allow us to identify possible sources of degradation, revealing a path to prolonging the cycle life.

Strain mapping in individual nanoparticles allows for the detection of inhomogeneity in lithium contents, observation of structural phase transitions, verification of cracks, and determination of defects.[12,64–66,104] Coherent X-ray diffractive imaging in the Bragg geometry (BCDI) is well-suited to providing this information with a strain resolution of greater than $\Delta L/L = 10^{-4}$ where L is the lattice spacing that is being probed and ΔL is a fractional change.[105,106] The observation of extended defects such as edge or screw dislocations is often difficult and requires invasive and destructive preparation such as with electron microscopy-based techniques. In BCDI, however, they appear as singularities in the phase field, despite the presence of noise or limited spatial resolution.[107] In this method, a crystal is slightly (approximately 1°) rocked across the Bragg condition under focused, coherent X-rays to capture a 3D representation of the X-ray scattering around the Bragg peak (see Figure 4.1a). A phase-retrieval algorithm then reconstructs the electron density and the displacement from an ideal crystal lattice. We used BCDI to measure the displacement field and strain in pristine NCA cathode nanoparticles synthesized under two different annealing conditions.

4.3 Bragg coherent diffractive imaging

The samples were prepared in a multi-step synthesis. First, a hydroxide precursor containing Ni, Co and Al is made in the desired stoichiometric proportions, followed by thermal treatments at 800° C of their mixtures with lithium hydroxide to form crystalline $LiNi_{0.8}Co_{0.15}Al_{0.05}O_2$.[109] Treatments were carried out for 12 and 24 hr to compare the evolution of strain and defects with respect to annealing time. The average crystal properties retrieved from bulk X-ray diffraction (XRD) showed good agreement with literature values for NCA (see Supplementary Figure 4.8).[110] SEM images revealed that most particles had three-dimensional features, with particle sizes ranging from 300–1000 nm in the longest dimension. Platelets existed in smaller quantities, observed by TEM. Additional TEM and SEM images are shown in Supplementary Figures 4.4, 4.5. The samples were mounted by one of two methods. We mounted the crystals annealed for 12 hr in epoxy sandwiched between two Kapton foils to form a sample with roughly 10% X-ray transmission. In the case of the longer 24 hr anneal, we loaded the crystals as composite cathodes on aluminum foil into the AMPIX holder for measurement.[111] The latter approach allowed for easier mounting of the sample and later *in situ* cycling, and we expect only small differences in the intensity of the scattered signal due to scattering on the

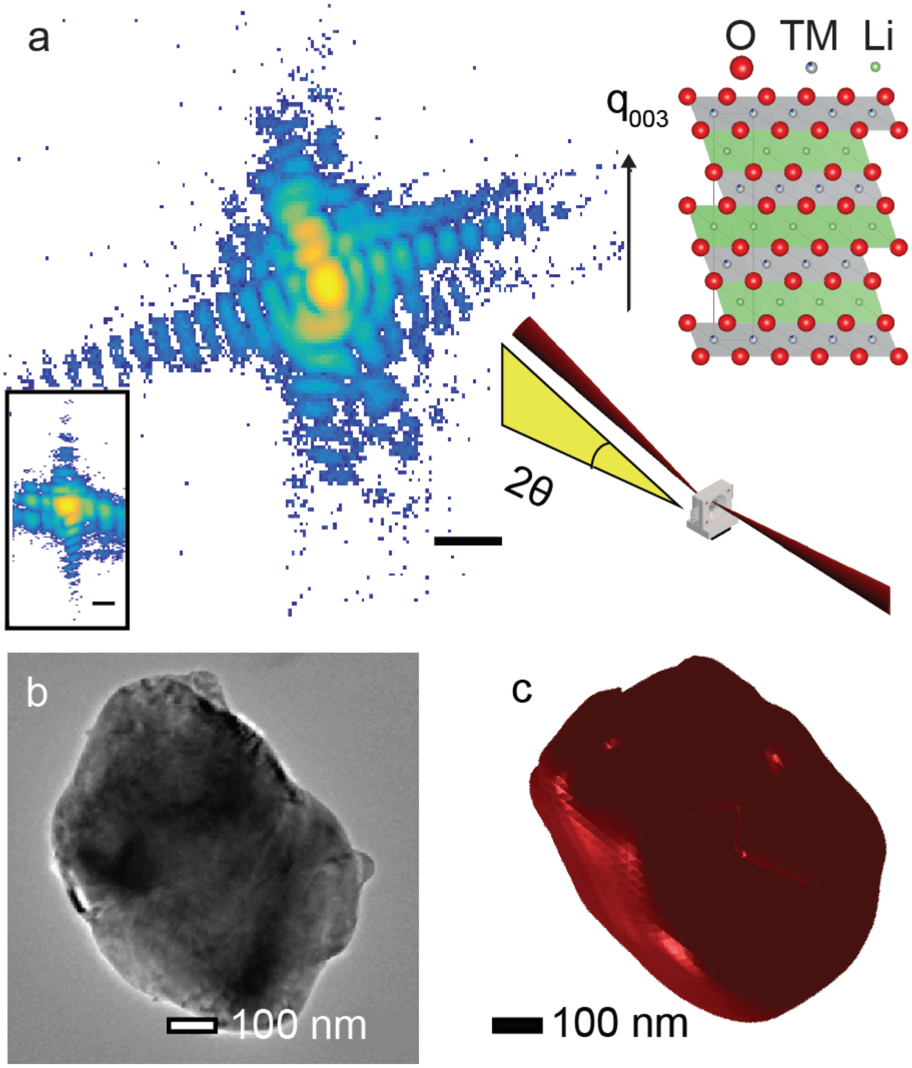

Figure 4.1: (a) Experimental sketch with diffraction pattern from initial synthesis, as seen on the detector with background subtracted (0.01 Å^{-1} scale bar). As we rock the sample, the detector collects different slices through the Bragg peak, capturing a 3D dataset. Shown in the inset is the same diffraction pattern in a direction orthogonal to the original, with 0.001 Å^{-1} scale bar. At the top right is a representation of the crystal structure, with Li in green, Ni/Co/Al gray, and O in red. Al and Co replace a fraction of the Ni ions within the crystal structure.[108] The wavevector is also shown, demonstrating our sensitivity to interlayer strain. (b) TEM of NCA battery cathode nanoparticles from initial synthesis. The particles are roughly cubic in shape and vary between 300 nm and 1000 nm in size. (c) Reconstructed 3D particle shape from the diffraction pattern in (a).

lithium anode and the electrolyte.

The (003) Bragg peak from a single NCA particle, which corresponds to the interlayer spacing (the *c* lattice parameter in Figure 4.1b), was measured over a rocking curve with a width of 0.4°. Asymmetry in the diffraction pattern shown in Figure 4.1a indicates a nonhomogeneous displacement field within the reconstructed particle. The number of intensity maxima (fringes) along the crystal truncation rods are directly related to the final resolution of the reconstructed particle and is similar to past work.[65] Two sets of 12 fringes on either side of the object yield an estimated resolution of 40 nm (500 nm/12 fringes) along the scattered wavevector, with a resolution closer to 100 nm orthogonal to the wavevector. More precisely, we calculate a comparable average resolution of 100 nm using the phase retrieval transfer function (PRTF) in Supplementary Figure 4.11.

For each data point, three-dimensional reciprocal space data was used to retrieve the real space image and displacement field of the nanoparticle. We used a genetic algorithm (GA) to generate five generations of reconstructions.[68, 92] Each generation consisted of 50 separate reconstructions, which were each made up of 406 iterations of alternating hybrid input-output (HIO) and error reductions (ER) phase retrieval algorithms. Two reconstructions with the lowest χ-squared error metric were chosen from each generation as the "parents" for the following generation. (See Figure 4.6 for reconstruction error.) This entire GA process was repeated for later comparison to confirm convergence to a unique solution. We define the edge of the reconstructed crystals at 10% of the maximum electron density, consistent with the average particle size confirmed by SEM and TEM. We selected the highest-quality diffraction patterns from more than 40 measurements. 17 distinct particles were used in our analysis, one from the 12 hr anneal and 16 from the 24 hr anneal. In addition to using the metrics of PRTF and number of fringes, reconstructions had to consistently converge to the same solution to be considered.

We observed the presence of dislocations of mixed edge and screw character for both the short and long annealing times in pristine NCA particles. In both particles shown in Figure 4.2, there is a change in phase of 2π rad around each phase singularity. Many of the measured particles contained dislocations in the pristine state and comparable dislocation density of approximately

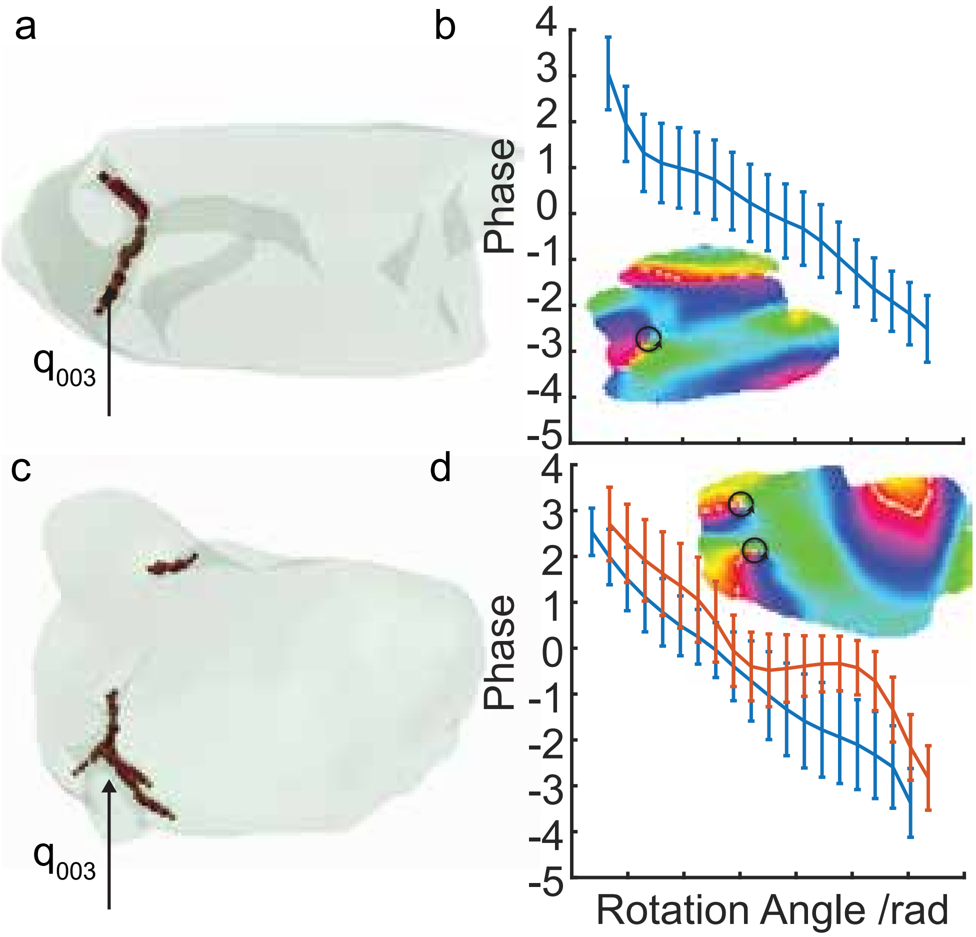

Figure 4.2: (a,c) Electron density isosurface with dislocation in NCA made after 12 hr and 24 hr annealing times, respectively. (b,d) Plot of phase ramp in a circle about the dislocation core in one slice of the particles shown at left.[64]The uncertainty is taken from error in the phase. Insets show the displacement field slice that we used with circles pinpointing dislocations. Annealing thus does not appear to remove dislocations. These dislocations have combined screw and edge character.

10^9 cm^{-2} that agrees with previous BCDI-enabled measurements (see Supplementary Figures 4.10, 4.9).[53] The phase changes linearly in pure screw dislocations, whereas it displays an additional sinusoidal variation in the presence of an edge dislocation.[112] In the three-dimensional images the dislocation path was calculated using the discrete Laplacian of the phase.[92] These dislocation cores curve throughout the structure, indicating a mixed screw and edge character. The Burgers vector is parallel to the dislocation core for screw dislocations, and perpendicular for edge dislocations.

In Figure 4.2a,b, a primarily screw dislocation traces a helical path through the particle. Helical dislocations can form by climb of a straight dislocation with a screw component.[112] Pure screw dislocations can spontaneously assume a helical form with a large chemical stress such as produced by a large temperature change. Such a helical dislocation is unstable upon formation. As this was present in the pristine state, it is a function of the initial synthesis.[113] Dislocations in other material systems have also been correlated with modified elemental concentrations, such as 25% higher Mn concentration in auxetic FeMn.[114]

The particle annealed for 12 hr contains strain located in the form of unique stripe-like platelets (Figure 4.3a-c) as compared with the particles annealed for 24 hr (Figure 4.3d-f). The overall size of these features varies, being 50–100 nm wide and several hundred nanometers long, taking up roughly 11% of the total particle volume as defined by isosurfaces in Figure 4.3b,e. As the size for the shorter dimension is comparable to the spatial resolution, the features may be even smaller. The majority of these features are parallel with the crystal layers (*i.e.* the c direction of the unit cell) and located within the outer region of the particle. Several of these strained regions, however, contain a large component perpendicular to the layers as well. The amount of strain within these features is at an average of 0.3%, corresponding to a change in the c-lattice parameter of 0.04 Å. The number and overall size of these strain features is reduced with a longer anneal time. Using a linear elasticity model one can calculate the elastic energy of the particle $E = \frac{1}{2}Y \int \varepsilon^2 dV$, where Y is the Young's modulus, and ε the particle strain.[112] In Figure 4.3g, a comparison of a particle from the short anneal time (black dotted line) and the longer anneal time (red dots) are shown in a plot of the elastic energy. We use a calculated Young's modulus of $LiCoO_2$, another layered electrode material, making the comparison correct up to a normalization factor.[115] This overall reduction in average strain energy is supported by Williamson-Hall analysis of *ex situ* powder diffraction (see Supplementary Figure 4.12), which is a bulk averaged technique.[116]

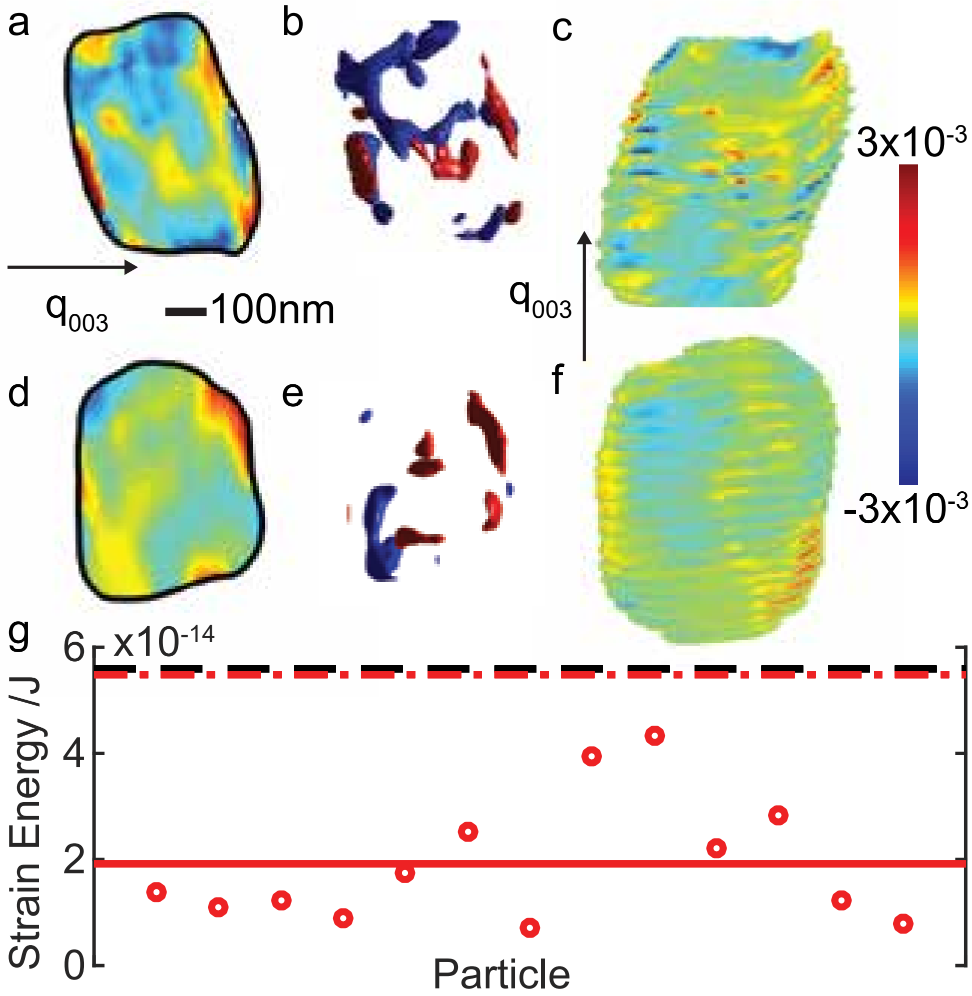

Figure 4.3: (a,d) Central slices of strain through particles after 12 and 24 hr anneals, respectively, with the direction of the wavevector labeled. The scale bar is 100 nm. (b,e) 3D rendering of the strain features with +0.1% and -0.1% in red and blue isosurfaces, respectively (relative to the average *c* lattice parameter). (c,f) 3D particle shape showing multiple slices parallel to the layered crystal, using the same color map, with wavevector shown. (g) Plot of relative elastic energy in 14 pristine NCA particles annealed during 24 hr (in red) with the mean shown as a solid red line and 3σ standard deviation shown as a dot-dashed line. The black dotted line shown is the mean strain energy calculated for the 12 hr anneal.

4.4 Conclusion

We speculate that this striping more strongly seen in at shorter annealing times because the structure has not fully equilibrated. One possibility is a concentration of antisite defects, as predicted by a recent density functional theory study.[117] Indeed, the 12 hr-annealed crystals showed a lower intensity ratio of $I(003)/I(104)$ relative to the 24 hr-annealed (roughly 3.42 vs. 4.08) indicating a greater difficulty to produce an ordered sample.[118] Hoang et al. predicted very low site-exchange energies for intralayer Ni/Co, Co/Al, and Al/Ni pairs, implying a very high level of disorder in real samples. This disorder possibly allows for the formation of elementally rich domains both during preparation and cycling. Interlayer and intralayer defects mean that these domains can be both perpendicular and parallel to the crystallographic layers, as seen in our work. If these features are indeed due to the length of the anneal time, an increased anneal time or cycling would remove them or allow them to come to equilibrium within the structure.[119] Comparison to samples that were annealed for twice as long (24 hr) resulted in a 60% lower average strain energy in the pristine state as shown in Figure 4.3.

Increasing the annealing time in the final synthesis step for NCA layered oxide cathodes is shown to reduce strain features which themselves may be the result of elementally rich domains created via antisite defects. However, this increased annealing time did not remove dislocations, and their role is as yet unclear in the overall performance of the battery. In lithium-excess layered oxides, dislocations may play a role in the enhanced anion redox capacity.[53] On the other hand, in commercial $LiNi_{1/3}Mn_{1/3}Co_{1/3}O_2$ (NMC), dislocations have been shown to lead to cracking of the primary cathode particles over long-term cycling.[17] The NMC and NCA cathode structures are similar enough that dislocations will likely lead to cracking with long-term cycling in both. Increasing the annealing time will modify the specific surface area of the primary particles, also affecting long-term electrochemical performance. The ease with which BCDI can identify distributions of dislocations and three-dimensional strain maps allows for practical suggestions for improving these materials, such as by modifying the annealing time to remove or induce strain features.

4.5 Supporting Information

- Sample preparation
- TEM and SEM images
- Reconstruction error and stability
- Lab source X-ray diffraction
- Calculated dislocation densities
- Images of the other reconstructed battery particles
- Phase Retrieval Transfer Function (PRTF)
- Williamson-Hall analysis comparing two synthesis methods

Sample preparation. $LiNi_{0.80}Co_{0.15}Al_{0.05}O_2$ (NCA) platelets were synthesized in a 2-step process for observation. $Ni(NO_3)_2{\cdot}6H_2O$, $Co(NO_3)_2{\cdot}6H_2O$, and $Al(NO_3)_3{\cdot}9H_2O$ were first mixed in water using the appropriate stoichiometric ratio, followed by addition of NaOH using a molar ratio of 1:2, in a total of 70 mL of solution. The mixture was hydrothermally treated at 160°C for 12 hr, using water in a Teflon-lined stainless vessel, producing the hydroxide precursor. The precursor was washed, dried, and then annealed at 400° C for 4 hr to decompose the layered double hydroxide structure.[109] The resulting oxide was mixed with $LiOH{\cdot}H_2O$ in a stoichiometric amount, and subsequently calcined at 800° C for 1 hr followed by 700° C for 12 hr.

Chapter 4, in full, is currently being prepared for submission for publication of the material. The dissertation author was the primary investigator and author of this paper. Thanks to my co-authors A. Singer, B. M. May, S. Hy, J. Wingert, A. Shabalin, S. Hrkac, R. Harder, E. Maxey, J. Masser, J. Cabana, Y. S. Meng, and O. G. Shpyrko.

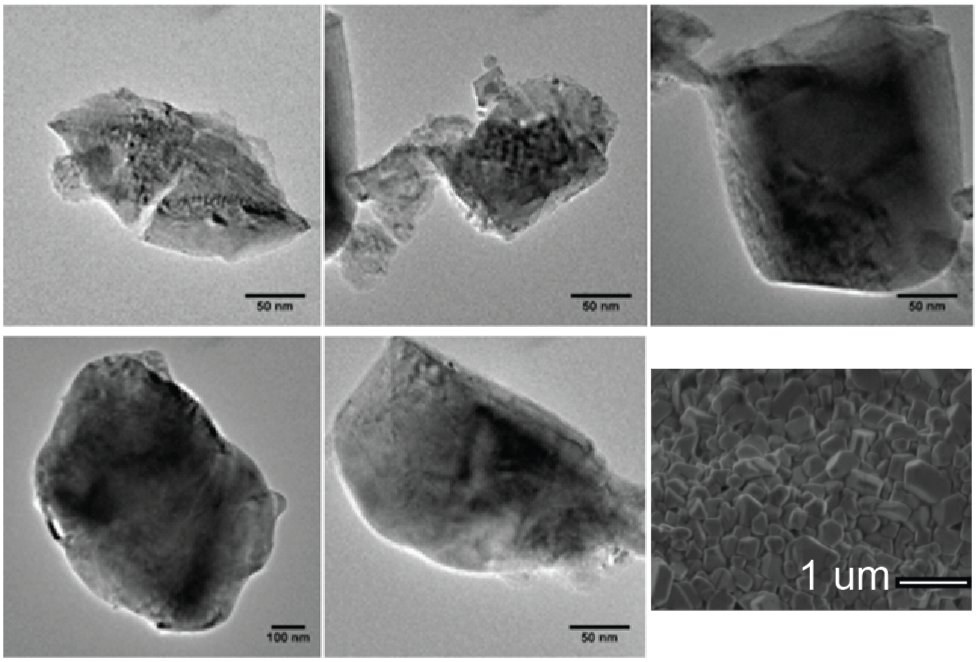

Figure 4.4: Additional TEM images along with SEM of the sample resulting from a 12 hr anneal. Images of the powder were taken on a JEOL JEM-3010 transmission electron microscope (TEM) as well as a JEOL JSM-6320F scanning electron microscope (SEM)

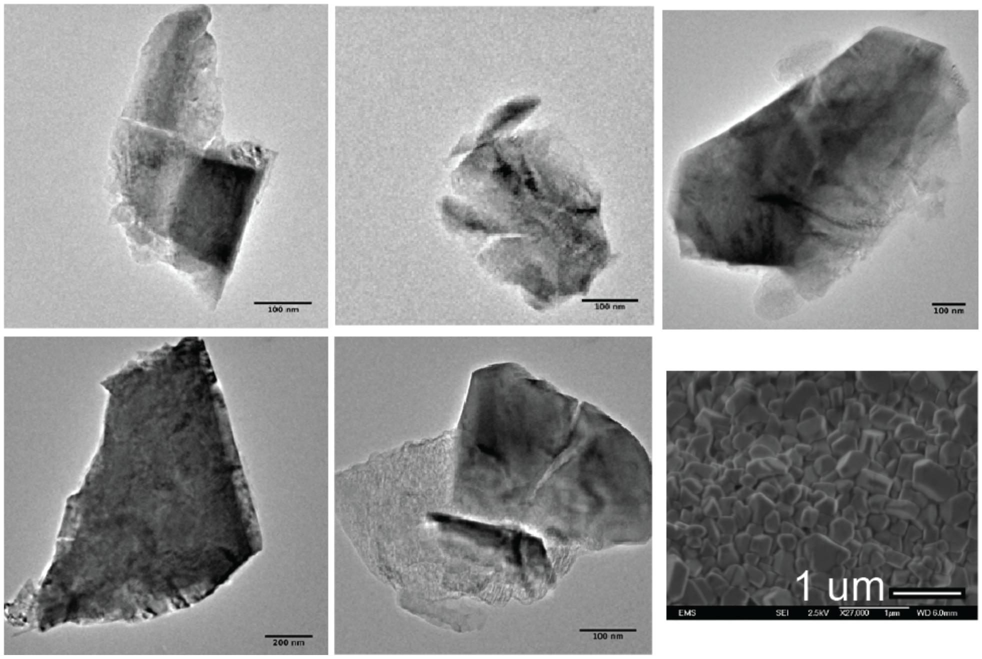

Figure 4.5: Additional TEM images along with SEM of the sample resulting from a 24 hr anneal. Images of the powder were taken on a JEOL JEM-3010 transmission electron microscope (TEM) as well as a JEOL JSM-6320F scanning electron microscope (SEM)

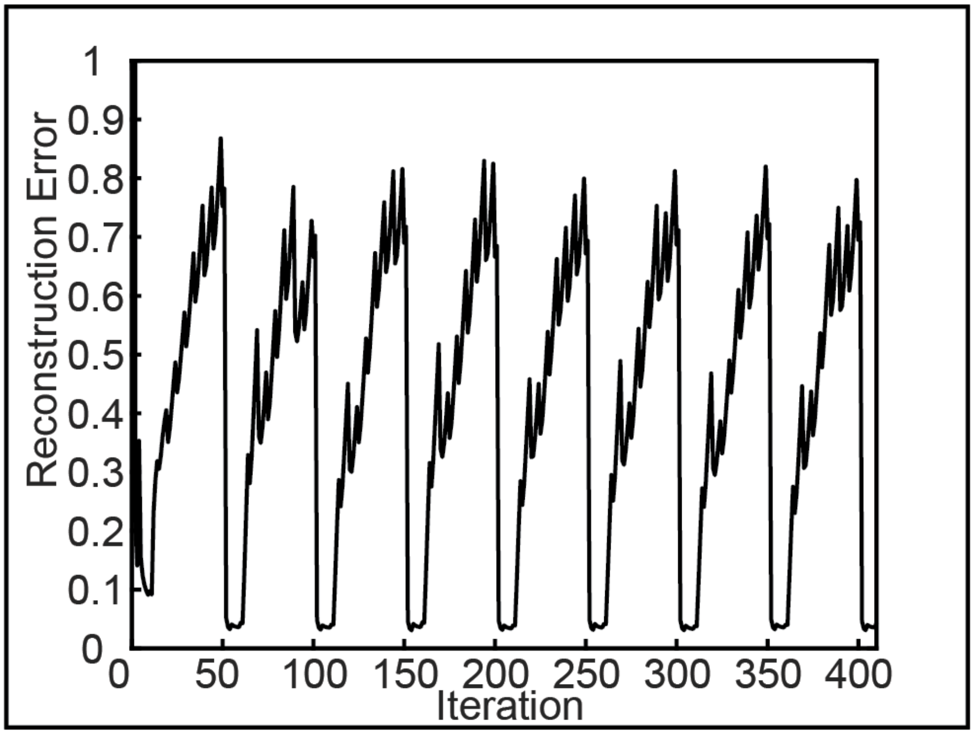

Figure 4.6: Representative reconstruction error χ^2 from a single 410-iteration reconstruction. The size of the error alternates as it switches between the Error-Reduction (ER) and Hybrid Input-Output (HIO) algorithms. The total reconstruction error here settles to below 0.03.

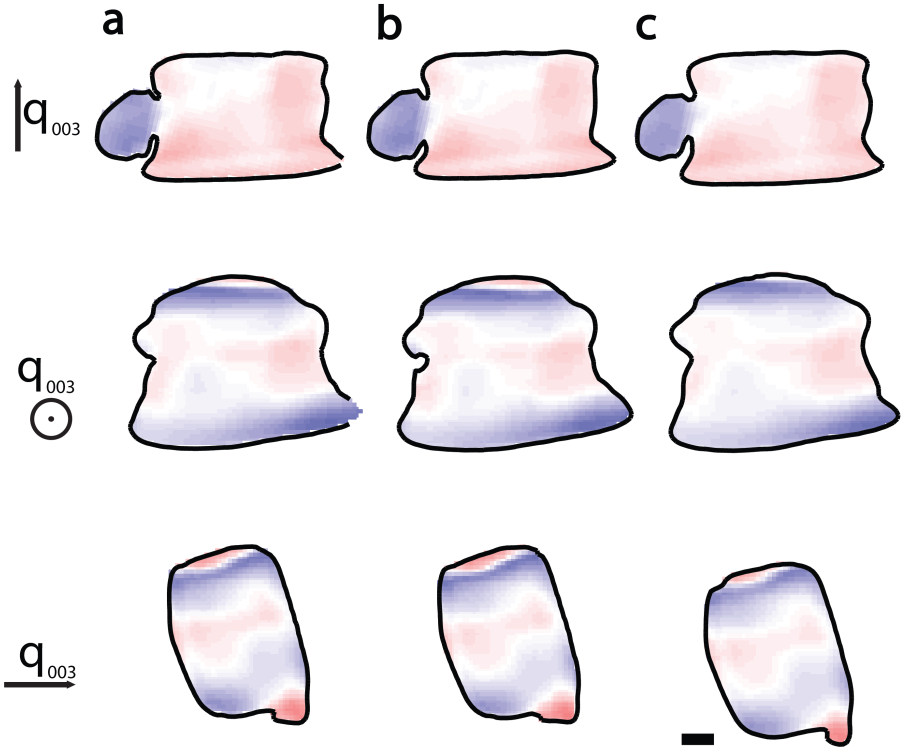

Figure 4.7: Confirming the stability of the reconstruction algorithm. All major features survive when comparing (a) cropped and (b) uncropped diffraction patterns, where editing was done to remove portions of another particle's Bragg peak that entered the detector area in the original scan. In (c) we show a reconstruction based on a Fourier transform of the average reconstruction in (a). Shown for all three are orthogonal central slices through the particle, with the scattered wavevector shown for reference.

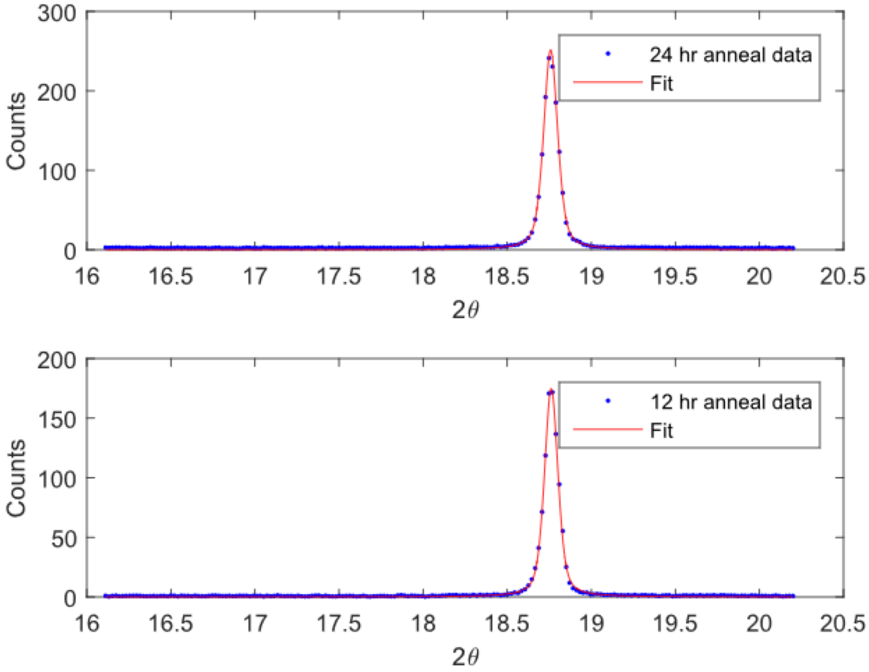

Figure 4.8: XRD of 12 hr (bottom) and 24 hr-annealed (top) cathode material. The cell parameters of the 12 hr (a = 2.86662 Å, c =14.18746 Å) and 24 hr (a = 2.86773 Å, c = 14.19034 Å) samples, were in good agreement with prior literature values.[120] Powder X-ray diffraction (XRD) of the samples was carried out with a Bruker D8 Advance powder X-ray diffractometer (Cu K_{α}).

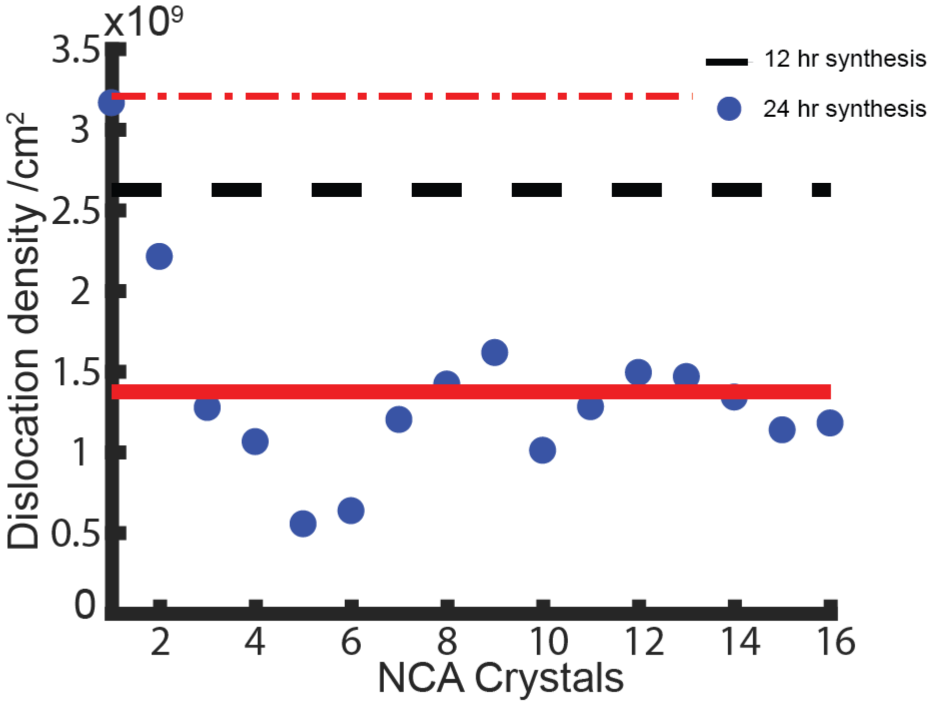

Figure 4.9: Plot of the dislocation density for both annealing times with pristine NCA cathode crystals. Unlike the average strain, there are still dislocations that are present. The blue dots are taken from single-particle BCDI measurements for the 24 hr anneal. The solid red line is an average for these measurements, with the red dotted line being 3σ away from this average. The black dotted line is the calculated dislocation density from the 12 hr anneal.

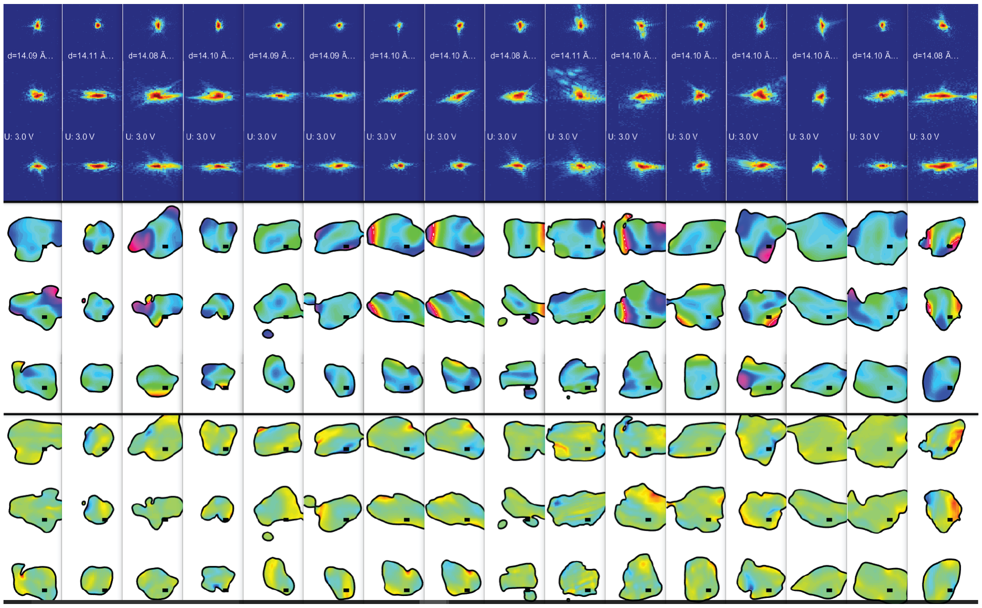

Figure 4.10: (top) Collected diffraction patterns of pristine NCA particles with their associated reconstruction of displacement (middle) and strain (bottom). These particles were used when calculating strain energy. Number 6 from the left was used in Figure 4.2, and number 7 from the left was used in Figure 4.3 in the main text. The direction of the scattered wavevector for each slice matches the convention used in previous Figures.

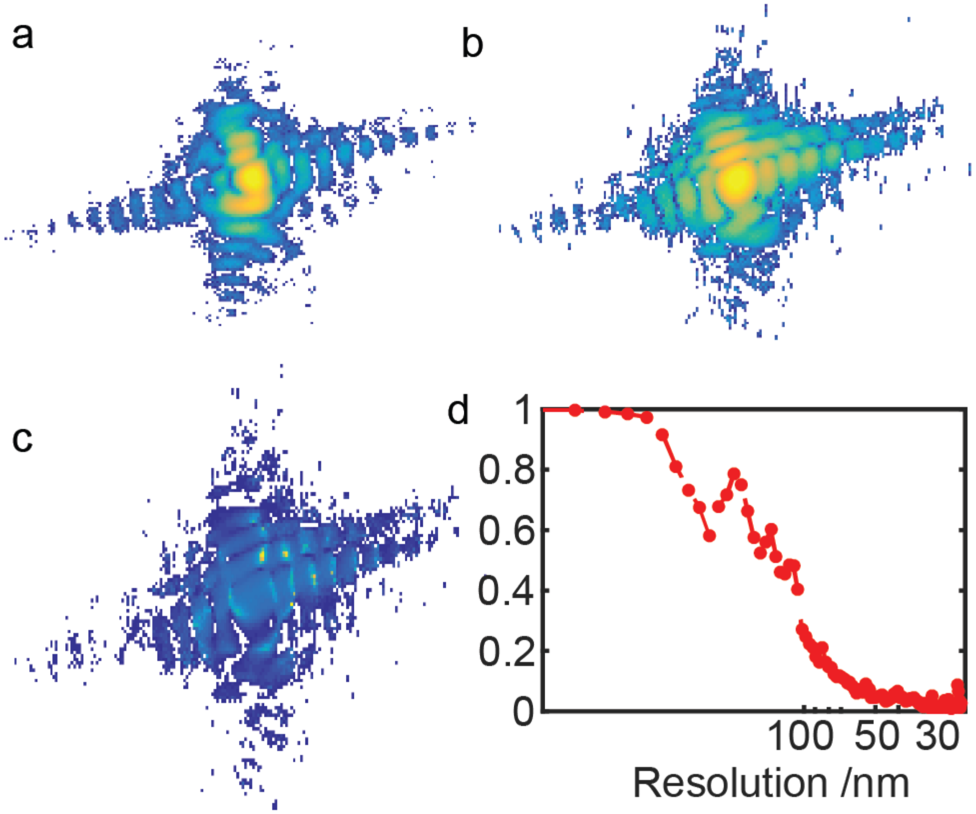

Figure 4.11: Resolution of BCDI measurements. (a) Original diffraction pattern for the particle resulting from a 12-hr anneal. (b) Fourier transform of the reconstruction. (c) Plots the phase retrieval transfer function (PRTF) as an image, shown as a 1D line in (d). The resolution is defined by the value of the PRTF dropping below 0.5 (a conservative estimate) yielding a 100 nm spatial resolution. A more liberal estimate is for the PRTF to fall below $1/e$, yielding an 80 nm resolution[42] The PRTF for the improved synthesis shows comparable resolution.

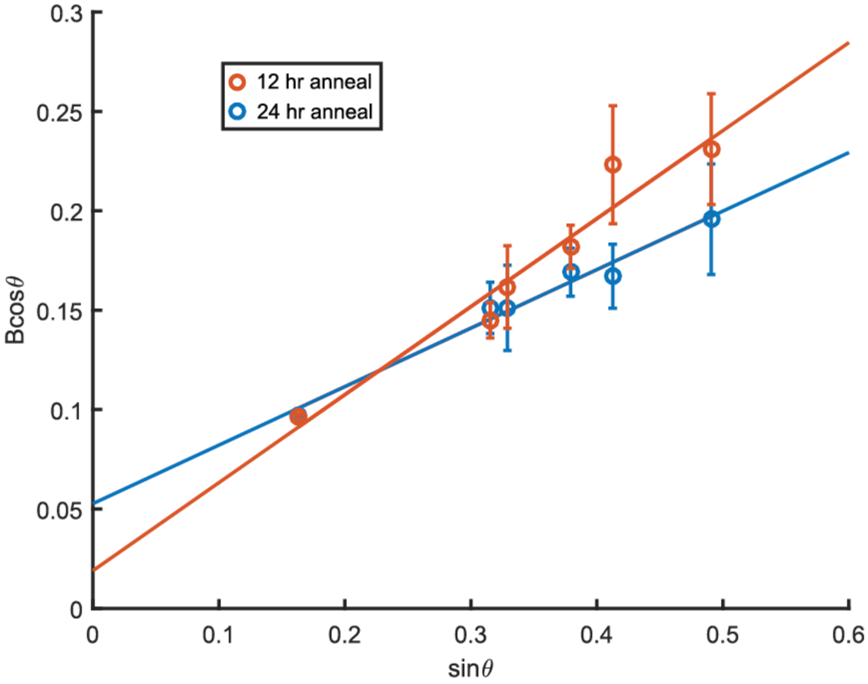

Figure 4.12: Williamson-Hall analysis of *ex situ* powder diffraction data that was background-corrected and fit with pseudo-Voigt peaks.[116, 121, 122] The error bars are taken from a 95% confidence interval of the FWHM from the fit of each peak. This reduction in the slope, which is proportional to the microstrain, confirms the reduction of strain we found in the single-particle measurements. Powder X-ray diffraction (XRD) of the samples was carried out with a Bruker D8 Advance powder X-ray diffractometer (Cu K_α).

Chapter 5

Determining lithium dynamics through ensemble powder diffraction of lithium-ion battery cathodes

Increasing the active material loading amount and electrode thickness is a promising option that could achieve a higher energy density in the near future. Unfortunately, increasing the thickness of the electrode generally results in electrochemical performance deterioration, such as rate and cycle stability.[123] In order to design an optimal thick electrode, understanding how performance loss occurs is necessary. It is well known that both ionic and electronic conductivity are critical factors for electrochemical performance in thick electrode.[124] The porosity, tortuosity, and conductive material distribution in thick electrode vary a lot along the depth direction, which largely determines the overall electrode conductivity (see Figures 5.1-5.3).[125] This variation indicates some diversity in the behavior of nanoparticles at different locations in the thick electrode. The information on the single particle behavior along the depth direction, therefore, would provide unique insights into the conductivity and uniformity of thick electrodes, which can further shed light on the optimization of thick electrode processing.

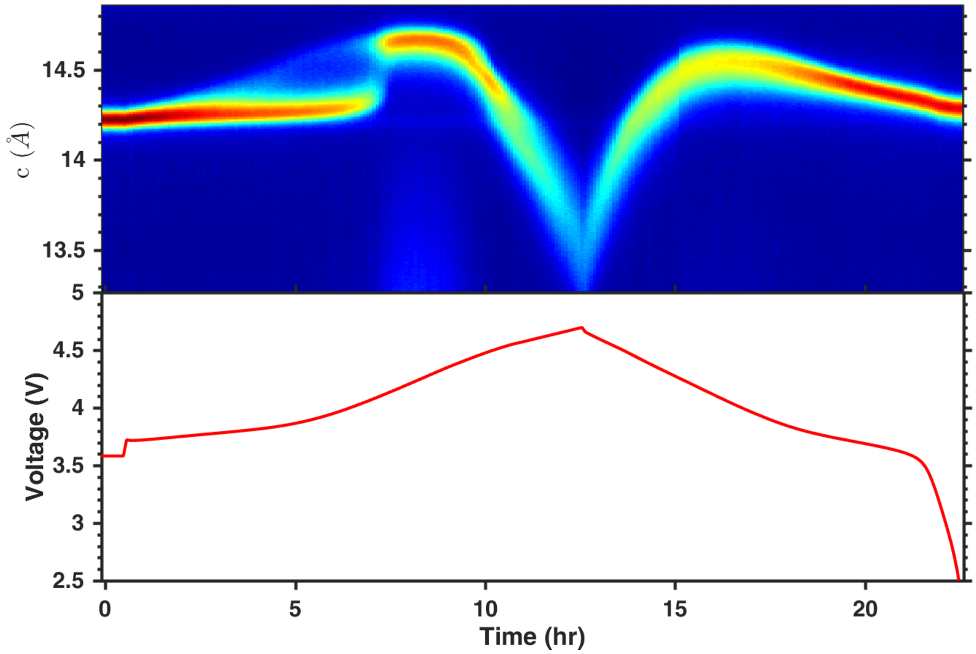

Figure 5.1: (top) Ensemble X-ray diffraction of thin CLO cathode cycled at C/10. (bottom) Voltage curve over time.

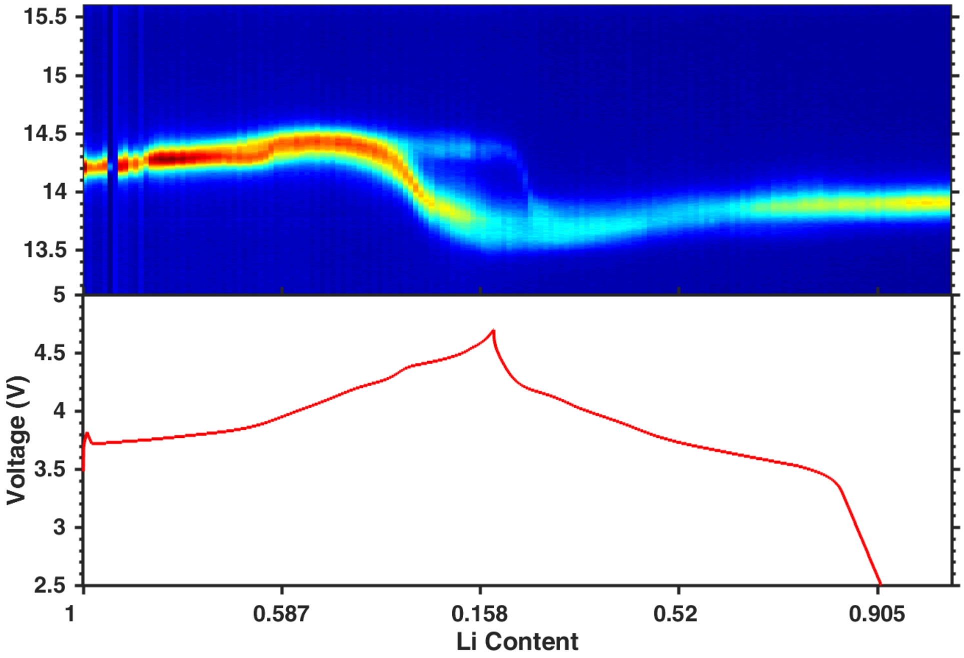

Figure 5.2: (top) Ensemble X-ray diffraction of thick CLO cathode cycled at C/10. (bottom) Voltage curve over time.

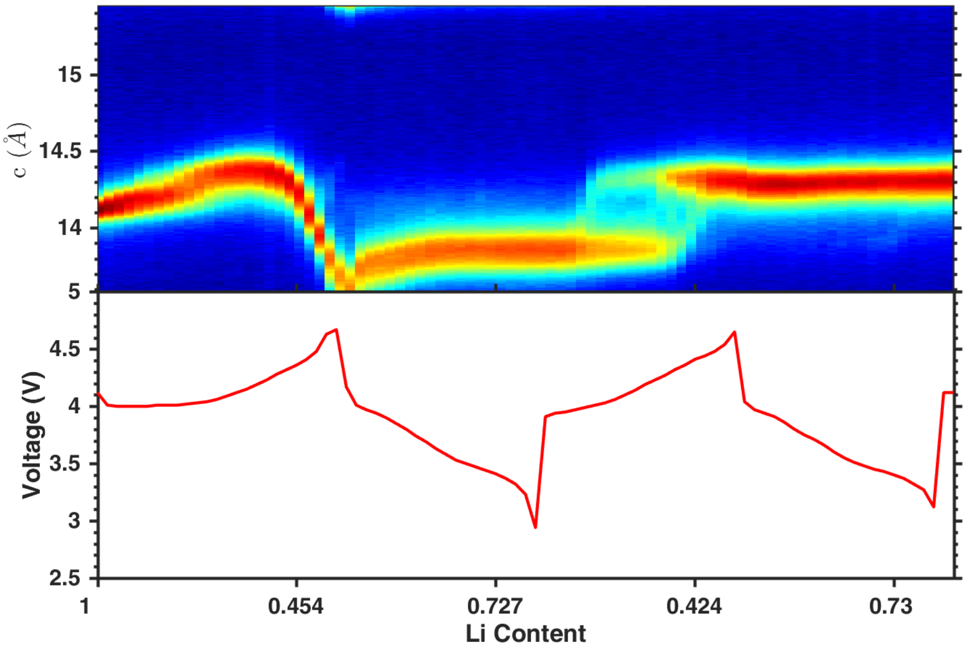

Figure 5.3: (top) Ensemble X-ray diffraction of thick CLO cathode cycled at C/3. (bottom) Voltage curve over time.

While conventional electron and X-ray diffraction measurements provide essential information on the surface and the crystal structure of large ensembles of battery particles, information on the nanomechanics of single particles is lost due to the averaging inherent in these techniques. In this sense, *in situ* Bragg coherent diffraction imaging gives unique insights into the structural dynamics of a single particle during battery operation.

This is an ongoing project. In my contribution I tracked the Bragg peaks' positions from many particles at different locations and observed that for thick electrodes the particles do not undergo the phase transition at the same time (see Figures 5.1-5.3, 5.4a).

In the past, BCDI studies of battery materials have been criticized for insensitivity to the spatial location of particles in the battery cathode. This proposed work aims to solve this problem and enable new functionality for Bragg coherent diffractive imaging. The proposed method is illustrated in Figure 5.4

Chapter 5, in part, is currently being prepared for submission for publication of the

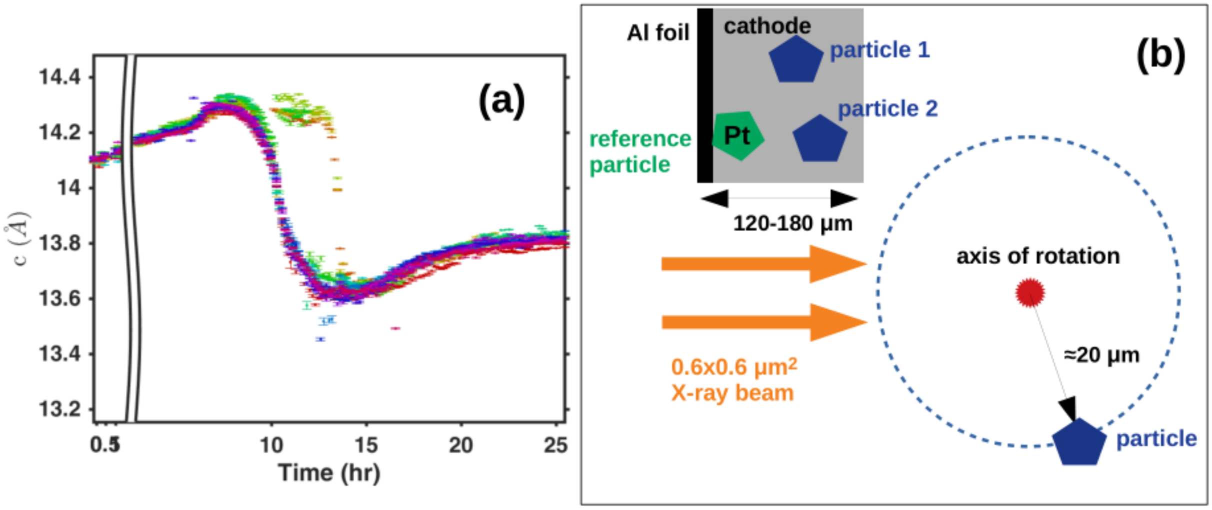

Figure 5.4: (a) Distribution of the charge profiles for ensemble of nanoparticles for a battery cathode of medium thickness (120 μm). There are two separated branches indicating that not all the particles undergo the phase transition at the same time which has not been observed for thin battery cathodes. (b) Schematic of a proposed method to improve on these measurements. Each of the particles will be brought to the center of rotation which can be aligned precisely using a micrometer pin at the beginning of the beamtime. The motor position for each of the measured particles will be compared with the position of the reference particle of different material (Pt) deposited on the cathode surface. The accuracy of the method is expected to be about 20-30 μm along the depth direction and about 2 μm in the directions perpendicular to the beam.

material. The dissertation author was the primary investigator and author of this material. Thanks to my co-authors A. Singer, A. Shabalin, M. Zhang, C. Fang, J. Wingert, S. Hrkac, E. Maxey, R. Harder, J. Masser, Y.S. Meng, and O.G. Shpyrko.

Chapter 6

Visualizing phase transformations in Li_2RuO_3 (LRO) with ensemble powder diffraction and coherent diffractive imaging

Li_2RuO_3 is a lithium-rich layered oxide (LRLO) cathode. Although it does not have great potential for commercialization, its simplicity allows it to serve as a model for other more complex systems such as $Li_{1.2}Ni_{0.133}Mn_{0.534}Co_{0.133}O_2$. To this end I and my collaborators hoped to perform a number of BCDI measurements on cathode nanoparticles.

Two challenges prevented the success of our plan. One, the particle morphology was rarely suitable for BCDI. By this I mean that the particle sizes were either much smaller or much larger than the X-ray beam spot size. In addition, many of the measured cathodes contained crystals with a preferred orientation, which greatly decreases the chance of finding a crystal in an isolated Bragg condition (see Figures 6.2a and 6.2).

The second challenge is that, unexpectedly, there were multiple so-called impurity pseudo-

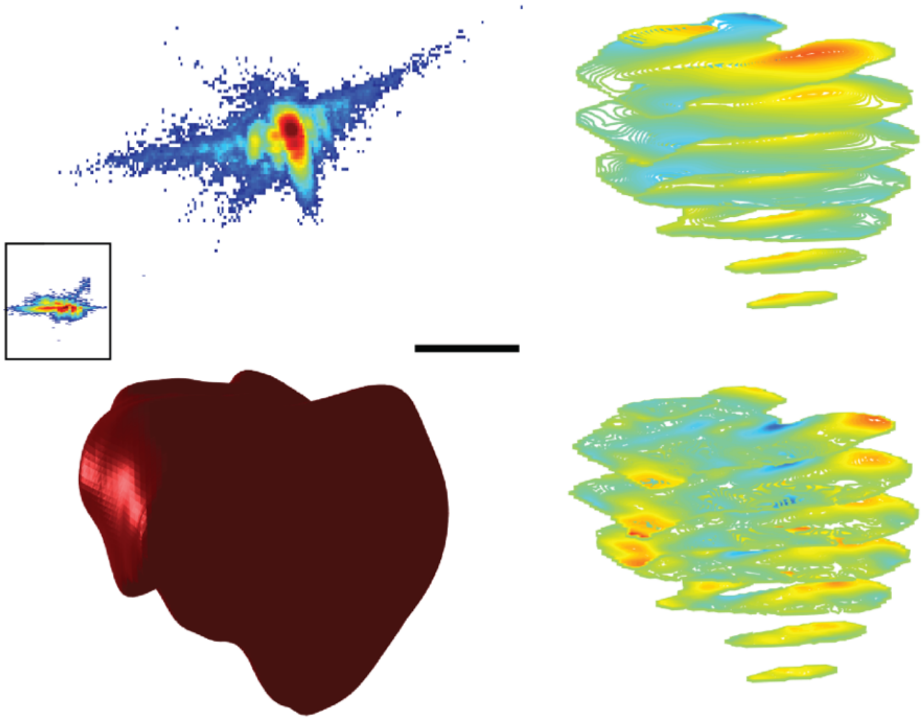

Figure 6.1: One of few BCDI reconstructions of a Li_2RuO_3 cathode particle. (top left) Diffraction pattern as seen on the detector. The inset shows a perpendicular slice through the 3D pattern. (bottom left) The 3D particle shape. (top right) Visualization of the 3D displacement field of the particle. (bottom right) Visualization of the 3D strain field of the particle. The scale bar is 100 nm.

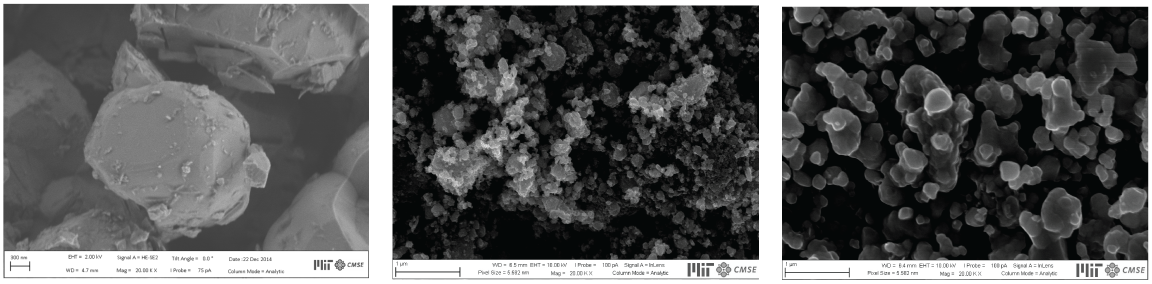

(a) SEM image of Li_2RuO_3 nanoparticles prepared by a solid-state synthesis. Compare the main particle in the field of view with Figure 6.1.

(b) SEM image of ball-milled Li_2RuO_3 nanoparticles

(c) SEM image of sintered Li_2RuO_3 nanoparticles

Figure 6.2: Ball-milled and sintered Li_2RuO_3 cathode nanoparticles have different size distributions, neither of which were suitable for BCDI measurements.

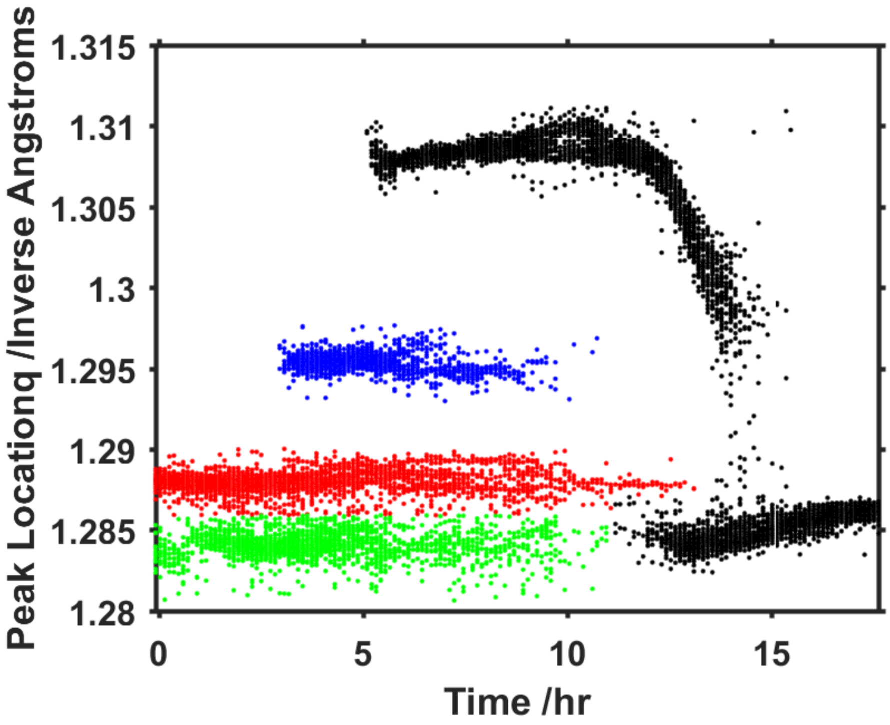

Figure 6.3: Fitting of ensemble powder diffraction of Li_2RuO_3. Each different phase is given a different color.

phases present in the pristine state. The phase retrieval algorithm struggles to reconstruct crystals which contain multiple phases. This is due to the difficulty of collecting the entire 3D reciprocal space map of both distinct Bragg peaks in one measurement.

The majority of single-particle measurements revealed that multiple phases were always present, and remained present for the majority of charging (see Figure 6.3). Changes to the synthesis methods reduced the relative fraction of crystals containing the additional pseudo-phases, but never solved the problem of optimizing the morphology for BCDI. Thus we were only able to measure ensemble powder diffraction.

What we call ensemble powder diffraction is the use of an unfocused or partially focused X-ray beam to scan over a larger portion of the Debye-Scherrer ring, a useful technique to simultaneously observe the behavior of each phase while cycling (see Figure 6.4). With at least partially coherent light, we are able to capture the truncation rods surrounding Bragg

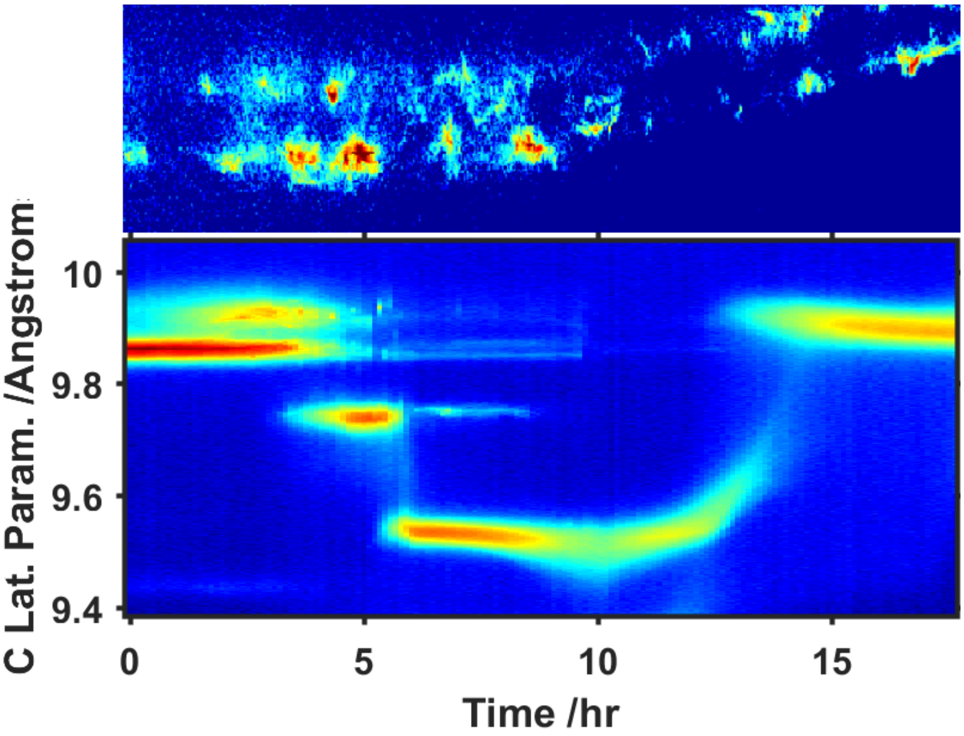

Figure 6.4: Ensemble powder diffraction of Li_2RuO_3. The right panel shows an image as capture by the CCD. The left panel is a time-series showing the average particle lattice parameter as a function of charging time. Worth noting is the appearance of multiple phases (multiple peaks at the same point in time at different lattice parameters).

peaks, indicating whether or not an individual nanocrystal contained one phase or multiple. In an analysis of individual particles we found that crystals did not exhibit multiple phases, and switched between phases all at once.

Although the multiple phases were characterized using this technique, the main research interest in the system called for single-particle reconstructions, and so the project was shelved.

Chapter 6 is not currently being prepared for publication. Thanks to my collaborators A. Singer, C. Fang, S. Hrkac, N. Hua, J. Wingert, A. Shabalin, R. Harder, E. Maxey, J. Masser, R.R. Rao, Y. Yu, P. Karayaylali, Y. Xiao-Horn, Y.S. Meng, and O.G. Shpyrko.

Chapter 7

Hybrid perovskite solar cells

7.1 Bragg coherent diffractive imaging of Cs-based perovskites

There are two main projects that made use of BCDI. Neither has yet resulted in a publication due to various difficulties with this class of materials. BCDI really shines with *operando* measurements, but we were unfortunately not able to measure a single crystal for more than a single scan due to concerns of X-ray beam damage. The existing results with several comments are summarized below.

Summary of pristine perovskite measurements

- $CsPbBr_3$ (both with and without 30 nm Au) on SiO_2 beam stable over at least one measurement
- $CsPbBr_{2.4}I_{0.6}$ unstable in beam (constant irradiation destroys crystallinity)
- Using gas flow cell with uncovered Br-based sample – did not find as good of a signal as the Au-covered sample. May be due to different size distribution of crystals on sample.
- Pristine $CsPbBr_3$ in N_2 atmosphere always yielded the highest-quality diffraction patterns

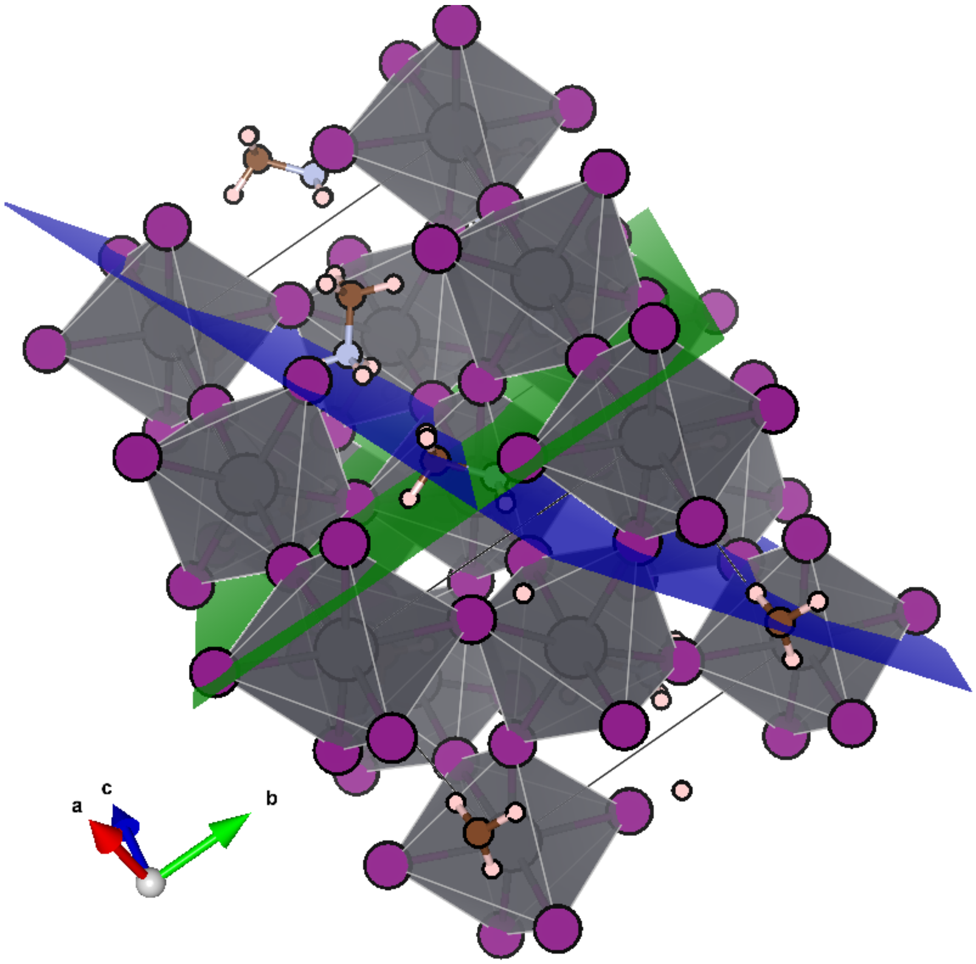

Figure 7.1: Tetragonal $CH_3NH_3PbI_3$, with the (101) Bragg coherent diffractive imaging, and X-ray photon correlation spectroscopy. Carbon atoms are brown, nitrogen light blue, hydrogen pink, iodine purple, and lead (with the surrounding tetrahedrons shown) in gray. Singular units cells of the three phases are shown in Figures 1.8 and 1.9.

with isolated crystals.

- Unsuccessfully tried to measure $CsPbBrI_2$ sample. The crystals on the sample appeared to be more dispersed as compared to previous $CsPbBr_3$ samples.
- For our size range, scan time, and X-ray flux, noticeable X-ray radiation damage on $CsPbBr_3$ occurs when measuring for more than two 15-minute scans. By this I mean more than a 10% loss in overall intensity and a visual change in the pattern shape.

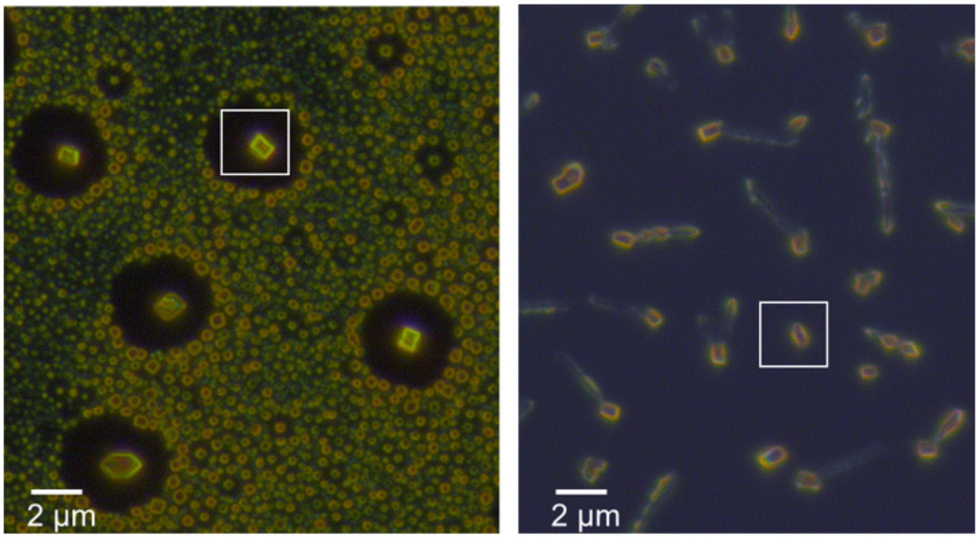

Figure 7.2: Optical images of synthesized $CsPbBr_3$ nanocrystals on a silicon dioxide substrate. Both have the same synthesis and plasma treatment, but in the leftmost image one waits for a longer period of time before spin coating the solution. A single $CsPbBr_3$ crystal is highlighted in each white box.

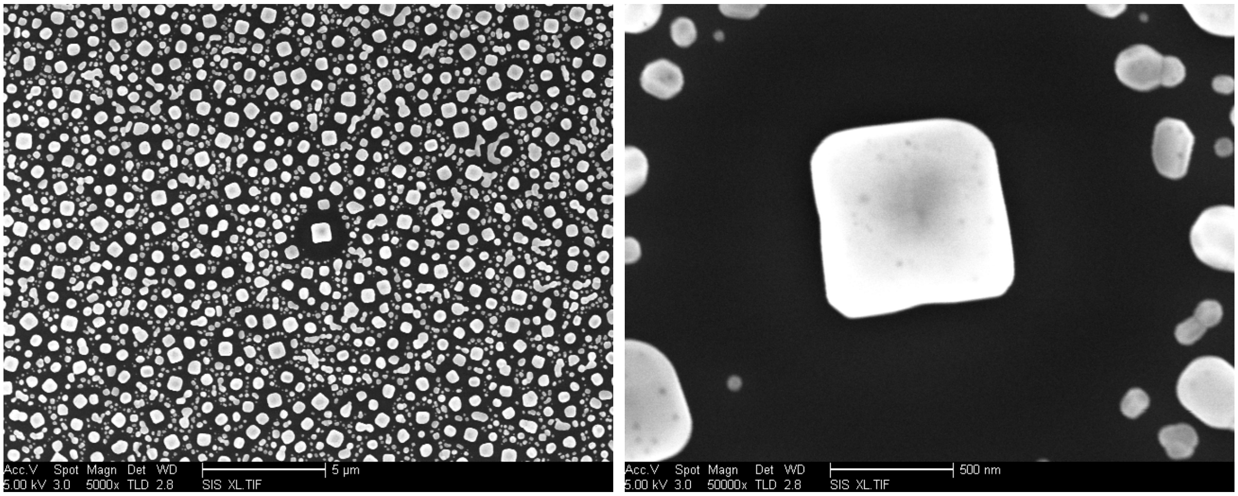

Figure 7.3: SEM of $CsPbBr_3$, close to the center of a spin coated sample. The distribution of crystals is very tightly-packed.

- Of the few reconstructions, pristine $CsPbBr_3$ particles often show strain on two ends of the particle.

Summary of humidity-exposed perovskite measurements

- Strain tends to increase after humidity exposure (found after measurements between 17-69%

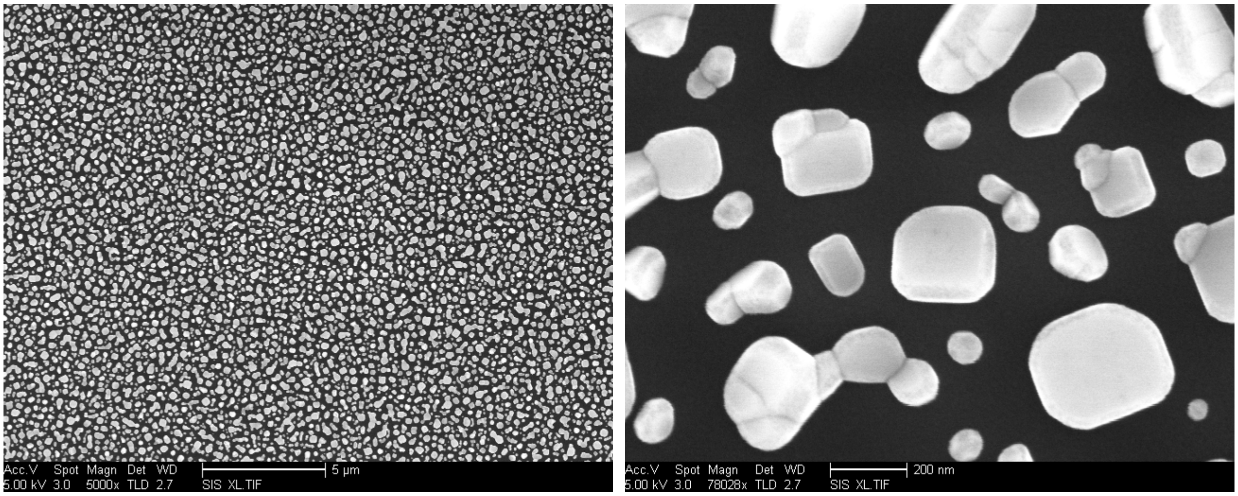

Figure 7.4: SEM of $CsPbBr_3$, close to the edge of a spin coated SiO_2 substrate. The distribution of crystals is much more disperse compared to the center.

relative humidity (RH) at 25° C in N_2 environment).

- During high humidity diffracted intensity decreases (pointing to a loss of crystallinity).
- At a high enough flow rate with humid N_2, and with a focused beam (for single-particle BCDI measurements) the particles are much more likely to rotate out of the X-ray beam.
- At the same flow rate and humidity with an unfocused X-ray beam, there is a slower loss of diffracted intensity, and no noticeable physical rotation of the crystals
- Scanned (101) and (202) Bragg peaks after humidity exposure. No phaseable diffraction patterns were found.
- When the humidity was turned on, we could not locate previously measured particles. This continued when the humidity was turned off, even for particles we had measured only once before in the low humidity state.
- Voltage-induced ion migration
- The samples used had unsuitable morphologies, vastly increasing the time to find suitable crystals.

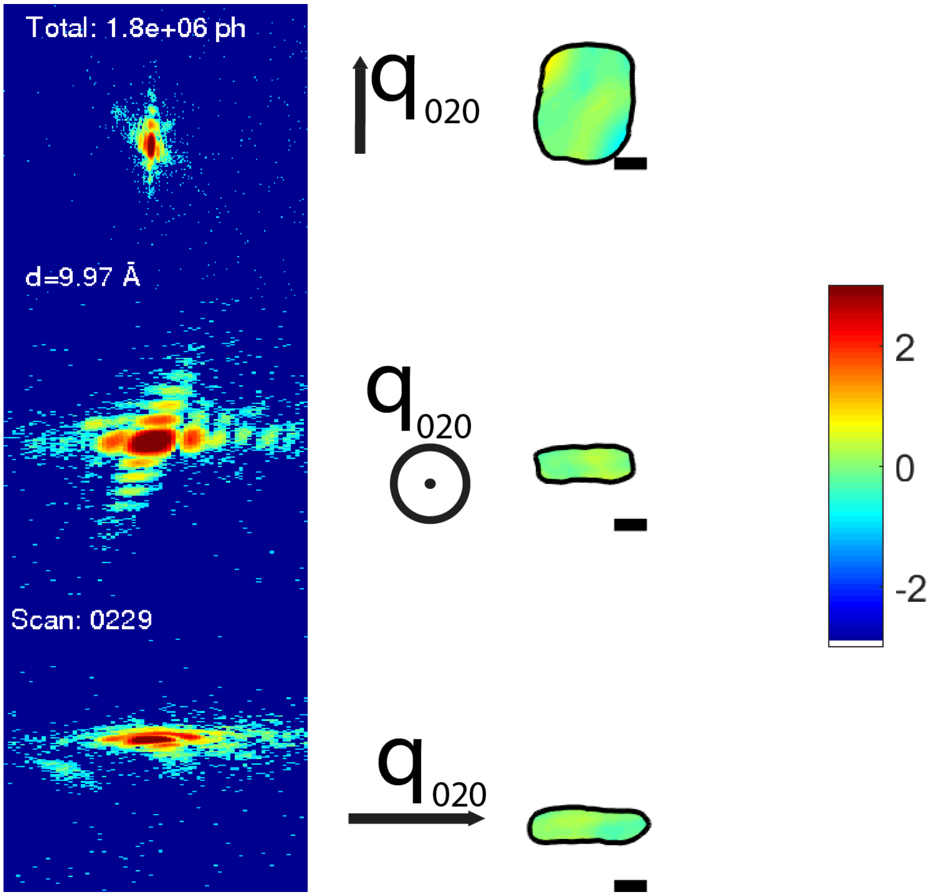

Figure 7.5: The three panels at the left are a preliminary diffraction pattern of $CsPbBr_3$, where the top image is a central slice of the Bragg peak as seen on the detector and the second and third images are orthogonal to this axis. At the middle are three central slices through the reconstructed particle showing displacement, the results of 200 correlated reconstructions of 1000 iterations each of this diffraction pattern. Color bar is in angstroms and reveals a low displacement in this pristine material at room temperature and low humidity. Continuous beam exposure on samples both covered with 30 nm gold, uncovered, in ambient conditions or inert nitrogen atmosphere revealed that the solar material was stable for time scales beyond the time scale of each measurement. See Figure 7.1 to see the corresponding (121) lattice plane.

- It could still be possible to perform measurements on voltage-induced ion migration, but the sample morphology has to be consistently and precisely formulated to improve the ease of finding suitable nanocrystals.

Figure 7.6: Multiple $CsPbBr_3$ crystals show strain at particle edges. Its consistency across scans suggests that it is not an artifact of the reconstruction, but a property of the crystal or substrate. The direction of the scattering vector $\mathbf{q}_{121}$ is indicated. See Figure 7.1 to see the corresponding lattice plane. It is unclear what the source of the tensile strain is for these crystals. One possibility is that since the crystals are likely to agglomerate together in multiples of two or three (see Figures 7.2, 7.7, and 7.8), the strain is due to another physically touching or connected nanocrystal.

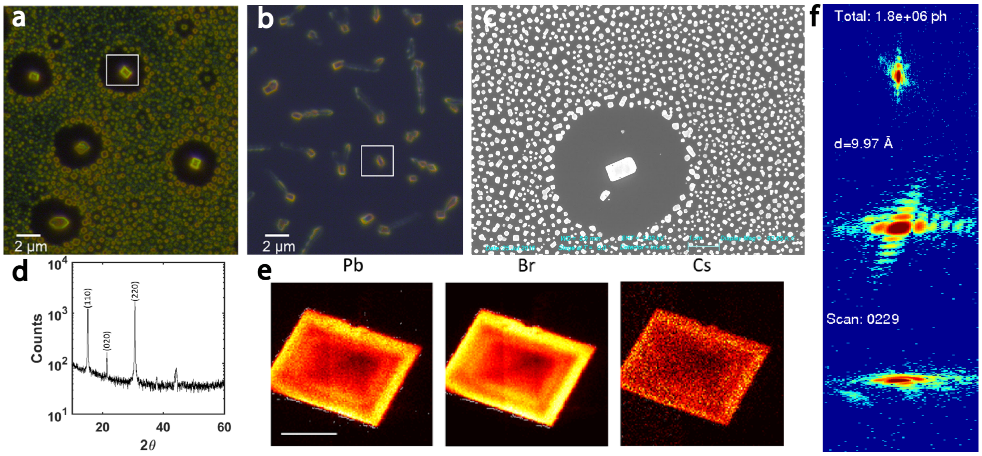

Figure 7.7: (a,b) Optical images of synthesized $CsPbBr_3$ nanocrystals on silicon dioxide substrate. Both have the same synthesis and plasma treatment, but in the leftmost image one waits for a longer period of time before spin coating the solution. The single $CsPbBr_3$ crystal is highlighted in the white box. (c) Scanning electron microscopy image of $CsPbBr_3$ crystals. The $CsPbBr_3$ solution was spin coated at 4000 rpm and annealed at 135° C for 2 min. (d) X-ray diffraction characterization (e) X-ray fluorescense image of $CsPbBr_3$ single crystal at APS Sector 2ID-D under focused X-ray nanoprobe, with 10 μm scale bar. (f) Collected diffraction pattern, where the top image is a central slice as seen on the detector and the second and third images are orthogonal.

7.1.1 Strain change in perovskite nanocrystals due to voltage

The device hysteresis has been theorized to be due to ion migrations, with spectroscopic impedance studies suggest that methylammonium lead iodide may be both an ionic and electronic conductor, similar to a number of inorganic perovskites.[29] Observation of a giant switchable photovoltaic effect can be understood through the creation of reversible P-I-N junctions created by ion drift.[126]

Computational modeling with density functional theory predicts low defect formation energies and diffusion barriers. Kinetic measurements using chronophotoamperometry provide a calculated activation energy that matches with predictions of iodide vacancy diffusion.[127] This is also supported by studies of the elasto-mechanical properties of these halide perovskites.[128] In addition to ion diffusion, several research groups believe that there is a slow ferroelectric ordering due to the dipolar cation within the inorganic lattice, or that there is a charge trapping/de-trapping occurring due to defects at interfaces between the perovskite semiconductor and other layers.[129]

There is a significant strain and change in lattice constants due to the presence of an iodine vacancy. A naïve density functional theory calculation of a 2×2×2 cubic $CH_3NH_3PbI_3$ supercell with a single neutral defect was performed to estimate the magnitude of the changes in the unit cell. I used the generalized gradient approximation with the revised Perdew-Burke-Ernzerhof GGA pseudopotential. A 530 eV plane wave energy cutoff was set in a 4×4×4 grid of k-points centered at the Γ point. Comparison between a complete and defective structure show that the average iodine-lead bond length changes by over a tenth of an angstrom, corresponding to a 2.7% average difference in the lattice parameters of a single unit cell. Therefore I anticipated that Bragg CDI would yield important insight into the defect diffusion in perovskite solar cells, would help to resolve open questions, and provide crucial data for further theoretical studies.

The perovskite samples were primarily prepared by Grace Luo in the group of David Fenning. We began with a simple model solar cell consisting of the active perovskite superconductor sandwiched with between the FTO layer and a gold top electrode. Applying a voltage across the film initiates ion vacancy diffusion, resembling solar cell operation.

The material consists of crystalline nanoparticles about 100–1000 nm in size (see Figure 7.7 for an SEM image of the perovskite material). In each measurement we focus the X-ray beam on a single nanoparticle, and by rocking the crystal are able to record the reciprocal space around a single Bragg peak, generally (101) and (121), depending on the type of sample. The plan was to reconstruct the collected rocking curves and measure strain maps of single nanoparticles during applied voltage. The partial orientation of the particles on the sample allows us to isolate a single Bragg peak for a single nanoparticle. The samples were prepared on a glass substrate for use in the reflection geometry.

After we have identified a single nanoparticle and established the experimental parameters to reliably record its strain field, we will apply a voltage across the sample and observe the modification of the strain field due to vacancy mediated diffusion. The diffusion length of an iodide vacancy at the timescale of a photocurrent relaxation at room temperature (approximately 10 s) using an estimated diffusion coefficient of 10^{-12} cm^2/s is approximately 30 nm. The drift distance for this time scale due to the fields commonly found in these devices (1 V over 500 nm, or 100 kV/cm) is about 80 nm.[29] We anticipated that an observable accumulation of vacancies at the interfaces would occur within several minutes. We expected that a few rocking curves could be recorded during that time, allowing us to monitor this build up.[127]

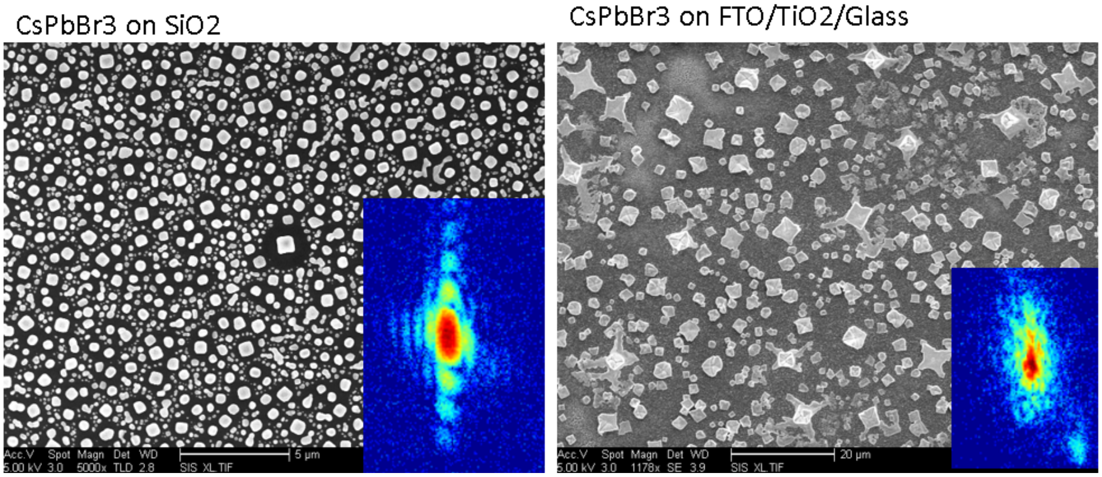

Figure 7.8: $CsPbBr_3$ BCDI diffraction patterns and SEM for two different sample preparations. The particle morphology was unsuitable for both, as a complete coverage of crystals is preferred to prevent shorting of the solar cell, and yet crystals must also be isolated in reciprocal space.

In this project, we tried two types of samples. In the first (see Figure 7.8), $CsPbBr_3$ was spin coated onto an FTO-covered glass substrate, and a gold electrode was evaporated on top of this. Even without uniform film coverage, we expected that some current would still flow through the perovskite crystals. Two different synthesis methods were attempted for this. However, it was found that the morphology was still unsuitable for measurement. In one, it was too difficult to find an isolated crystal, and in another two difficult to find any with sufficient diffraction intensity. The second type of sample (see Figure 7.19a)was actually prepared for a previous experiment using X-ray photon correlation spectroscopy which was attempting to measure the same changes but on a longer timescale (see Section 7.2 for more details).

7.1.2 A study of thermal and moisture stability

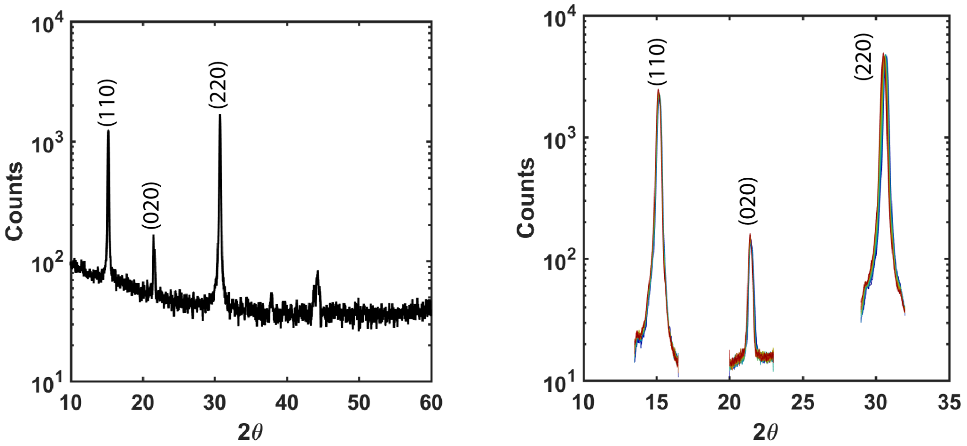

Figure 7.9: XRD and temperature-dependent XRD characterization of the $CsPbBr_3$ nanocrystals on silicon dioxide substrate. The temperature ranged from 300 K to 450 K. There is no dramatic change in Bragg peak intensity.

As large-area planar diodes, the performance of solar cells is determined by the sum of local recombination currents across the cell area. As such, the large-area performance of a solar cell is governed by "the weakest link in the chain". Highly-localized defects, such as impurities or single-structural defects, can shunt the diode and cause large recombination currents and losses in efficiency. Synchrotron-based nanoscale characterization of defects in silicon, thin-film, and organic solar cells have led to fundamental understanding of the large-area efficiency losses caused by nanoscale defects.[130–132] Recently, similar insights from synchrotron-based characterization of perovskite solar cell materials have begun to be established.[7, 133] The proposed work seeks to understand the microstructural origins of performance degradation in perovskite solar cell materials. Studies using mixed halide (I, Br) and mixed cation (Cs, FA) substitution in the perovskite framework have found that the mixtures have significantly improved stability compared to using purely an organic cation.[134–136] Knowledge of how these materials thermally degrade, based on both temperature and level of humidity, is unknown at the single-particle level, although it is instrumental to making a truly viable perovskite solar cell.

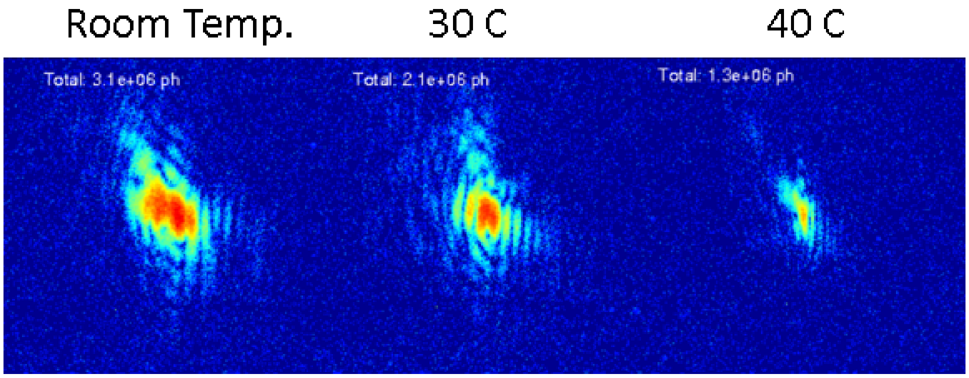

Figure 7.10: $CsPbBr_3$ BCDI diffraction pattern as a function of temperature. X-ray radiation damage strongly skews results. Diffraction patterns look qualitatively unchanged at the end of the heat treatment. Future measurement should only be two scans (at room temperature and an elevated temperature).

Therefore, I anticipated that Bragg CDI will yield important insight into the stability of perovskite solar cells and help to resolve open questions regarding the nanoscopic underpinnings of stability.

Description of Experiment(s)

The solar cell materials were prepared in the group of David Fenning on-site in the days leading up to the experiment in a simple spin coating procedure. A 1:1 ratio of $PbBr_2$ and CsBr are combined with the appropriate amount of DMSO solvent to obtain a 20 wt% solution. The $CsPbBr_3$ solution is spin coated on a plasma treated Si substrate, which is subsequently annealed at 150° C for 3 min.

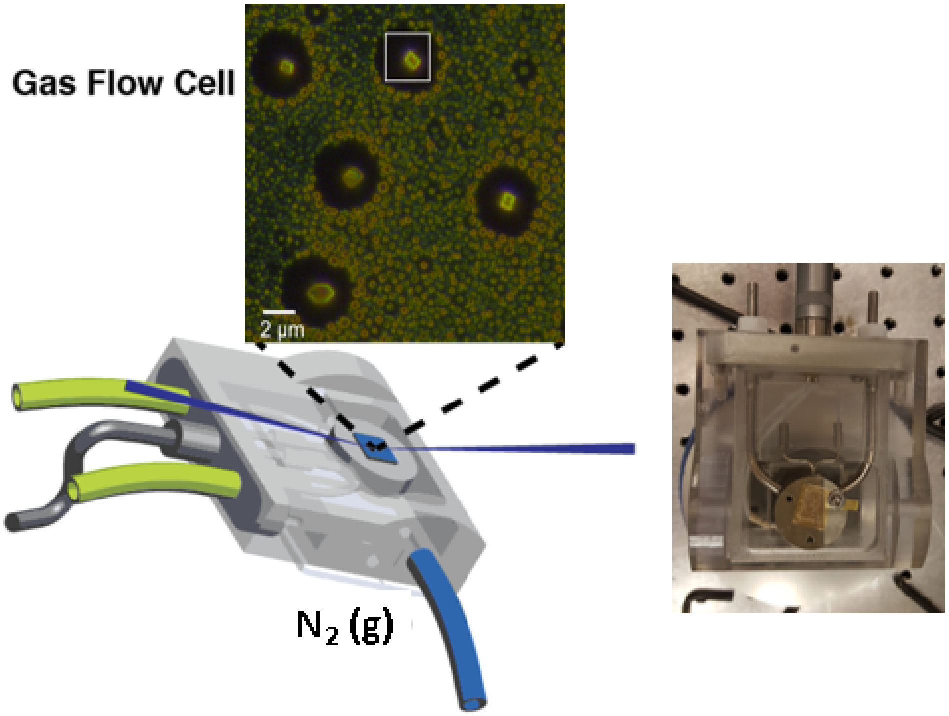

Figure 7.11: Gas flow cell with thermocouple. Not shown is the Kapton sheet sealing the sample from the external environment, or the hygrometer sensor inserted into the cell. This cell was used to pipe in a variety of gases of varying humidities. Figure partially adapted from[137]

The experimental setup was similar to the setup our group used to study structural dynamics in lithium ion batteries.[53,65]

We began with a simplified system consisting of the active perovskite semiconductor crystals on a silicon oxide substrate rather than a full solar cell stack.

The material consisted of cubic nanocrystals about ranging from 500–3000 nm in size (see Figure 7.11 for an optical image of the perovskite material). The XRD and temperature-dependent XRD characterization data of the same sample is provided in Figure 7.9. The material synthesis could be easily modified in order to produce crystals of a specific size to optimize the BCDI signal, and over the course of several visits, we tested several different possibilities (see Figures 7.2, 7.8, and 7.9). In each measurement, we focus the X-ray beam on a single nanoparticle and by rocking the crystal will record the reciprocal space around a single Bragg peak (*e.g.* (101) and (121), which showed preferred orientation depending on the nanocrystal morphology and

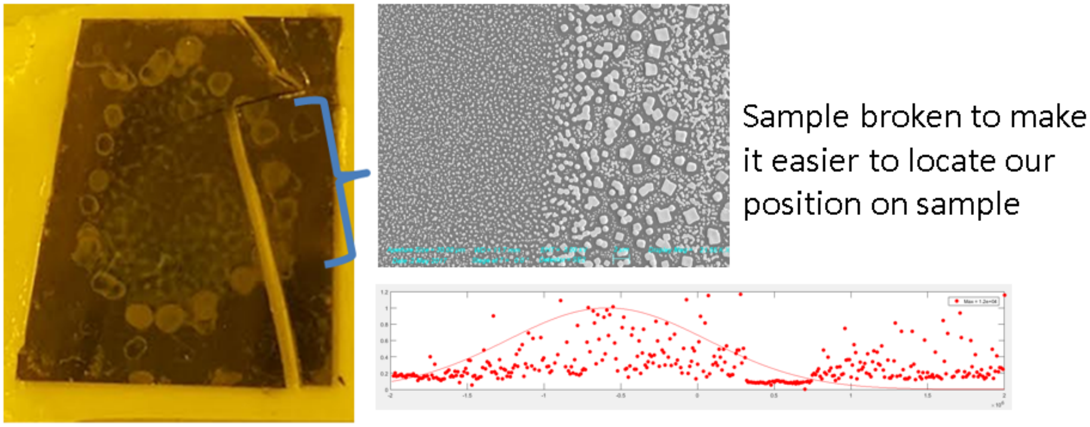

Sample broken to make it easier to locate our position on sample

Figure 7.12: Photograph of $CsPbBr_3$ sample, along with optical image and diffraction intensity linescan. The linescan is between the two differing size distributions. These differing distributions exist due to the spin coating process.

substrate). These rocking scans will be later reconstructed to yield the strain maps of single nanoparticles. We relied on a combination of spatial separation of the particles in the sample as well as a variation on the exact crystal orientation, allowing us to isolate a single Bragg peak for a single nanoparticle, similar to our works on batteries.[53, 138] After we have identified a single

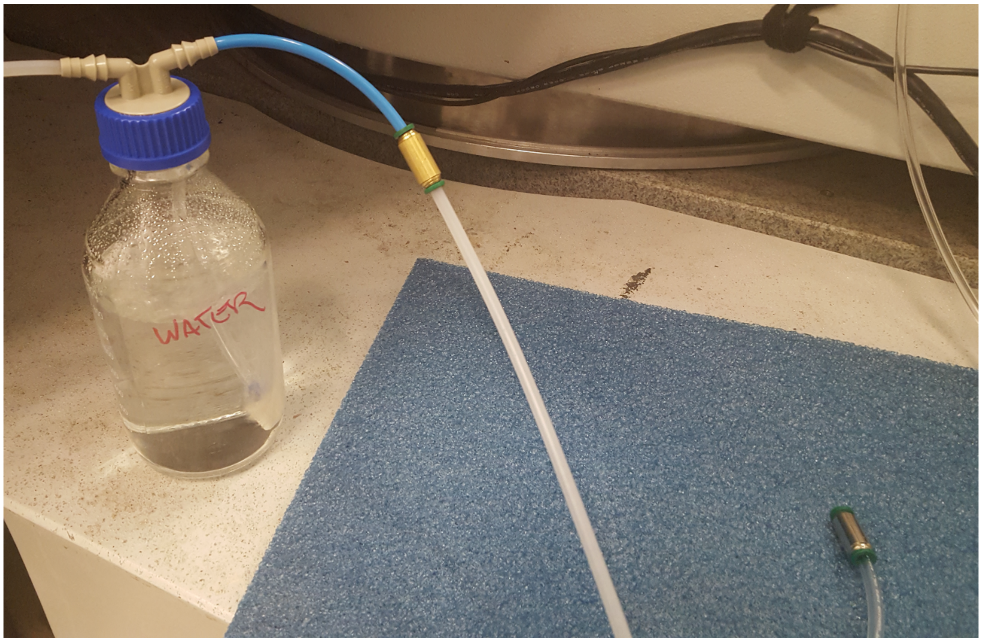

Figure 7.13: A distilled water bubbler was used for humidity control. This could be connected to the main N_2 flow control with the use of two valves. This allowed for **on** (high humidity) and **off** (low humidity) states.

nanoparticle and established the experimental parameters to reliably record its strain field, we will begin to pump moist air into the sealed temperature stage and observe the modification of the strain field. This measurement was first performed at room temperature for a variety of perovskite analogues. In subsequent weeks the plan was to test the same parameters at both decreased and increased temperatures (0° C, 85° C), and low and high relative humidity (see Figures 7.10 and 7.14, respectively). The former would rely on a sealed temperature stage already in place, while the latter will rely on using a bubbler (shown in Figure 7.13) and increasing the temperature to create a state of high humidity. The temperature and humidity range to be covered included the temperature and moisture required for the IEC standardized damp heat test (85° C, 85% relative humidity).

7.2 Time-resolved study of ion dynamics using X-ray photon correlation spectroscopy (XPCS)

7.2.1 Introduction to XPCS

The autocorrelation function is given by:

$$\frac{\langle I(\mathbf{q},t)I(\mathbf{q},t+\tau)\rangle}{\langle I(\mathbf{q})^2\rangle} = 1 + A(\mathbf{q})|g_1(\mathbf{q},\tau)|^2 \tag{7.1}$$

where $A(\mathbf{q})$ is a contrast factor and

$$g_1(\mathbf{q},\tau) \approx e^{-(\tau/\tau_q)^\beta} \tag{7.2}$$

is a stretched exponiential with stretching factor β and relaxation time τ_q.

XPCS experiments can measure the $\mathbf{q}$ dependence of the relaxation time. XPCS has previously been used, for example, in measuring the rate of interchange jumps in a Cu-Au alloy

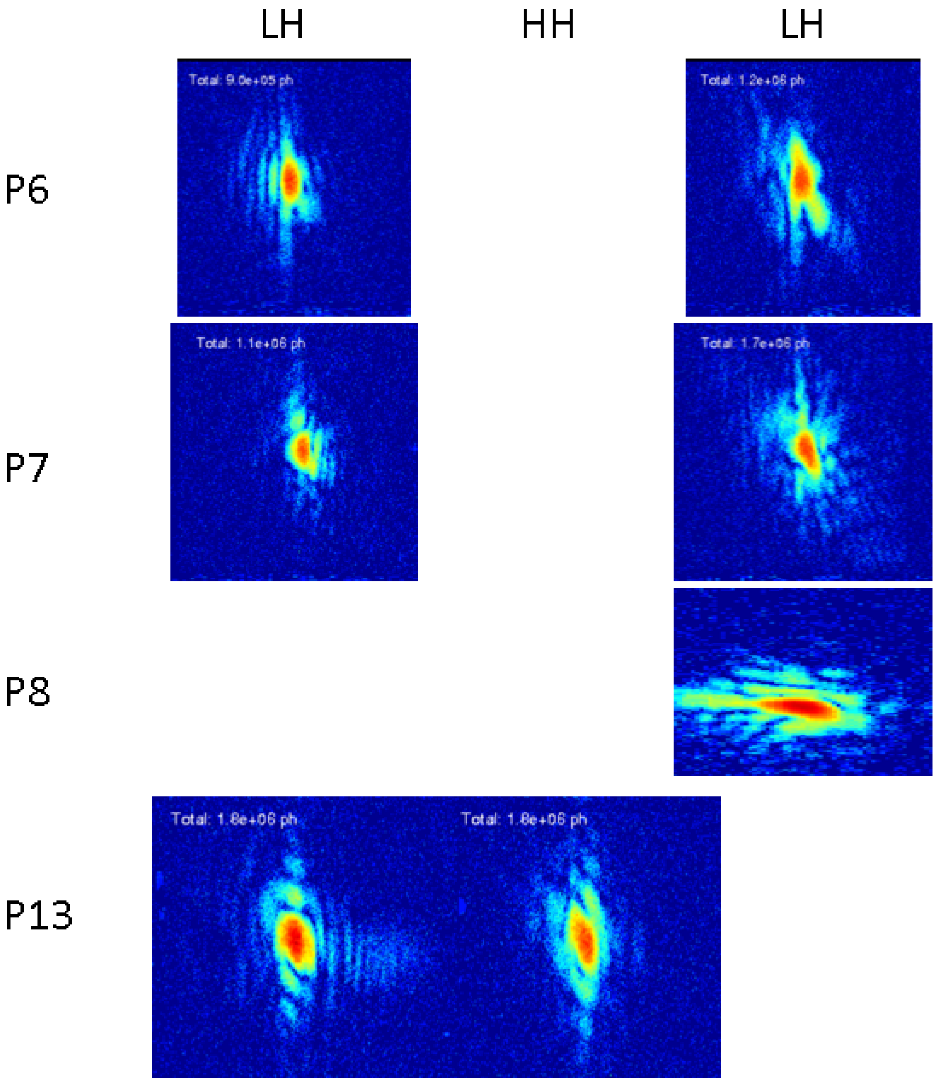

Figure 7.14: $CsPbBr_3$ BCDI diffraction patterns as seen on the detector as a function of temperature. X-ray radiation damage strongly skews results (as always). Strain tends to increase after humidity exposure. During high humidity signal decreases and starts to become disordered. These measurements were done between 17-69% relative humidity (RH) at 25° C in nitrogen environment. Under high gas flow, the crystals are also much more likely to rotate out of the X-ray beam (by being physically pushed). Each row refers to a different measured crystal. Each column refers to a different humidity level (with time increasing to the right).

single crystal on a time scale of minutes.[139, 140]

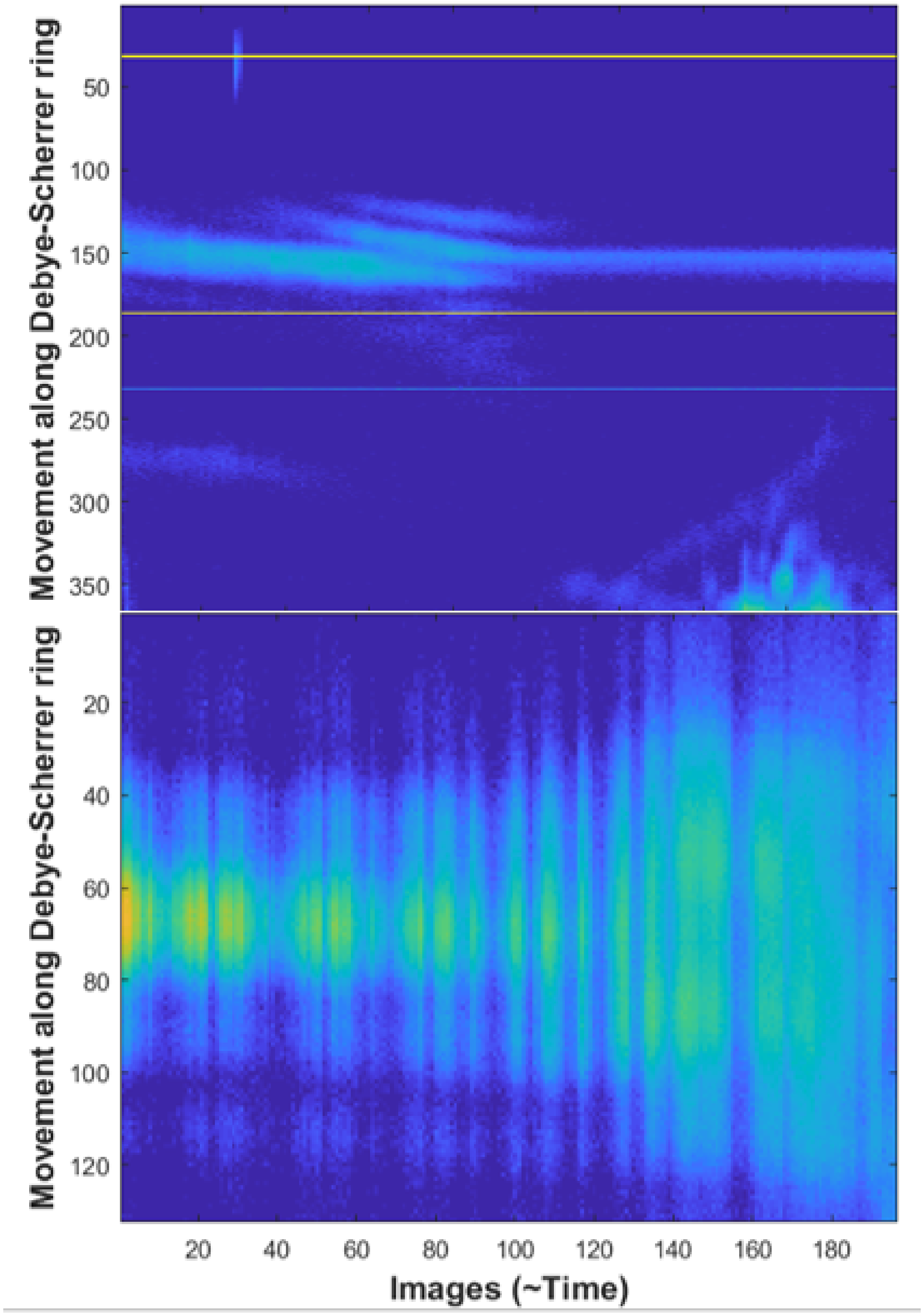

Figure 7.15: Two different $CsPbBr_3$ BCDI stability scans from PETRA after increasing humidity level. These images were taken in an N_2 environment. Once the humidity was turned on, we could not align to previously measured particles. Once it was turned off, we could not even align to other particles

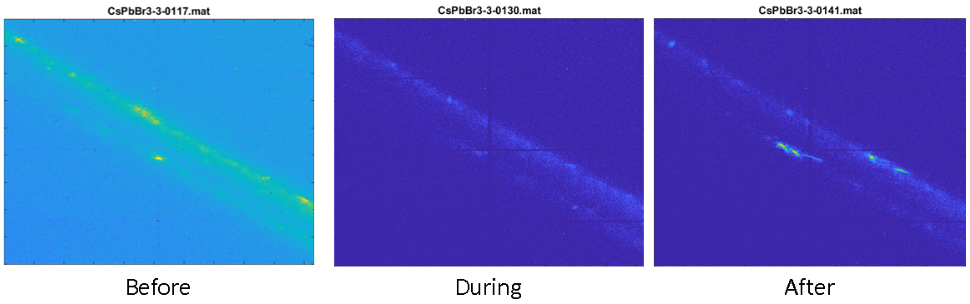

Figure 7.16: $CsPbBr_3$ ensemble powder diffraction as a function of humidity level. These images were taken in an N_2 environment. These scans were able to capture a larger part of the Debye-Scherrer ring compared to single-particle imaging, and reveal additional strain information that might not be visible with traditional powder diffraction. There were mobility issues with unfocused beam due to lower flux. The particle crystallinity was lower during high humidity conditions. There is a secondary peak at lower **q** (consistent with a measured (101) peak)

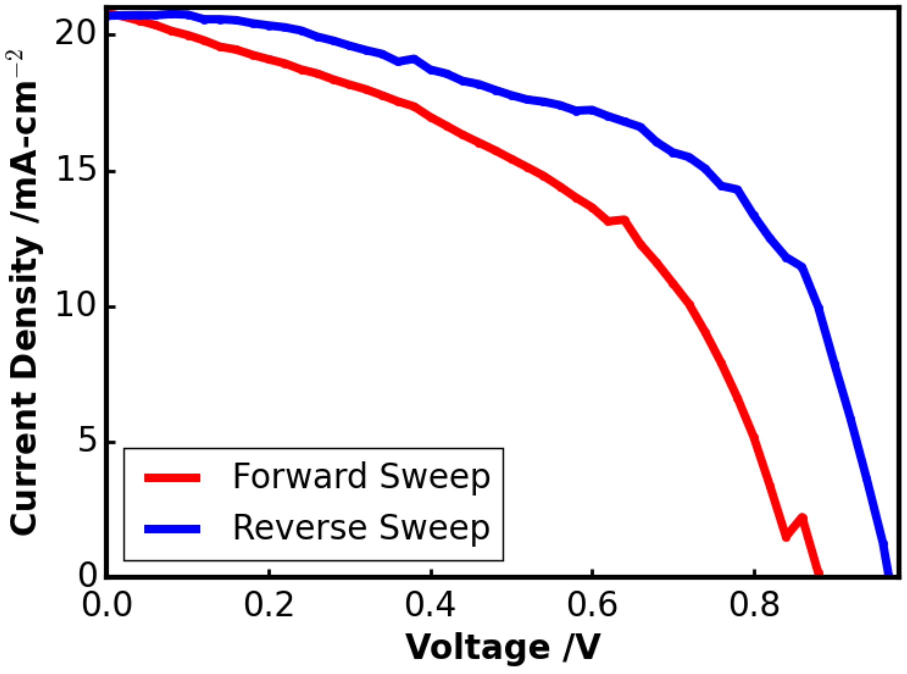

Figure 7.17: Representative $J-V$ curves of one of our standard perovskite solar cells measured at a scan rate of 0.1 V/s in both the forward and reverse sweeps.

7.2.2 Theoretical justification

A complete understanding of the causes of hysteresis in perovskite solar cells will allow us to intelligently modify the material properties to improve performance and stability.

In perovskite solar cells there is a dynamic polarization that builds up in the perovskite semiconductor layer (typically made of methylammonium lead iodide, or $CH_3NH_3PbI_3$) that will impede the flow of electron-hole pairs to their respective electrodes. The amount of hysteresis present depends on a number of factors including the intensity of incident light, sweep rate of the applied voltage, age of the device, temperature, and the exact architecture used. A number of experiments and theoretical simulations have revealed that ion movement likely plays an important role in limiting the overall efficiency. However, it is still unclear how exactly this happens and how it can be prevented.

The device hysteresis has been theorized to be due to ion migration, and evidence continues to grow. Spectroscopic impedance studies suggest that methylammonium lead iodide may be both an ionic and electronic conductor, similar to a number of inorganic perovskites.[29] Observation of a giant switchable photovoltaic effect can be understood through the creation of reversible P-I-N junctions created by ion drift.[126]

Computational modeling with density functional theory predicts low defect formation energies and diffusion barriers, and kinetic measurements using chronophotoamperometry provide a calculated activation energy that matches with predictions of iodide vacancy diffusion.[127] This is also supported by studies of the elasto-mechanical properties of these halide perovskites, which show that their densities and linear thermal expansion coefficients are between those of soft metals, polymers, and composite materials, allowing for easy creation and movement of ion defects.[128]

In addition to ion diffusion, several research groups believe that there is a slow ferroelectric ordering due to the dipolar cation within the inorganic lattice, or that there is a charge trapping/de-trapping occurring due to defects at interfaces between the perovskite semiconductor and other layers.[129] Although it is unlikely that ferroelectric effects dominate the observed hysteresis given recent quasielastic neutron scattering experiments, it is likely that there are multiple effects occurring simultaneously.[141] For example, the use of additional fullerene-based additives to the perovskite material has been shown to reduce (but not eliminate) the charge-voltage hysteresis.[142]

The APS Sector 8-ID-E has both the angular resolution and energy resolution in order to access the relevant Bragg peak of our sample. The geometry of the beamline allows adequate sampling of the speckles as shown in Figure 7.18.

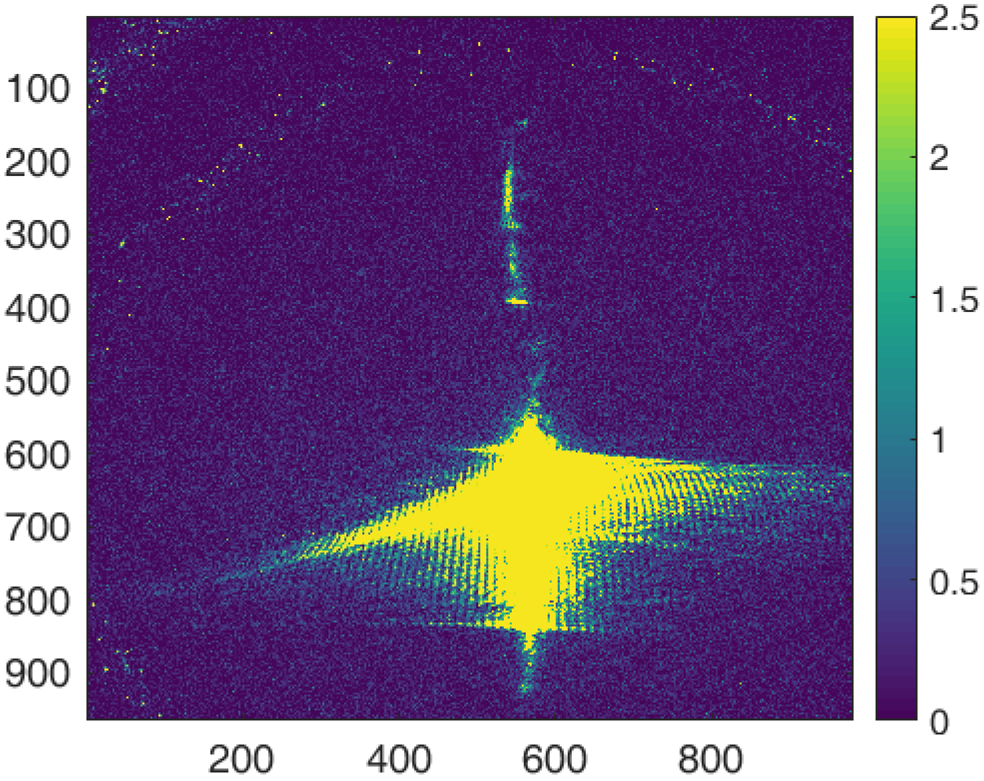

Figure 7.18: An example $CsPbI_3$ X-ray speckle pattern taken at APS Sector 8, as seen on the detector. The values on each axes are pixel numbers, with the horizontal axis approximately parallel to the wave vector $\mathbf{q}_{121}$ and the vertical axis corresponding to crystal rotation perpendicular to the beam (in the angle χ), a portion of the Debye-Scherrer ring.

We propose to use XPCS to examine the in-situ response of iodine vacancy concentration to an applied bias voltage, and to see how this response is dependent on temperature, sample composition, and sample age.

There is a significant strain and change in lattice constants due to the presence of an iodine vacancy. A density functional theory calculation of a 2×2×2 cubic $CH_3NH_3PbI_3$ supercell with a single neutral defect (corresponding to a ∼4% vacancy concentration, the theoretical upper estimate of vacancy concentration) was performed to estimate the magnitude of the changes in the unit cell. We used the generalized gradient approximation with a PBEsol pseudopotential. A 530 eV plane wave energy cutoff was set in a 4×4×4 grid of k-points centered at the Γ-point. Comparison between a complete and defective structure show that the average iodine-lead bond length changes by over a tenth of an angstrom, corresponding to a 2.7% average difference in the lattice parameters of a single unit cell.

The ion vacancy-mediated diffusion is monitored by measuring the intensity of the Bragg peak as a function of time. These measurements should tell us whether the iodine movement is diffusive or ballistic in nature. The higher order correlation functions, and the autocorrelation function, will give insight into whether the motion is collective or a localized phenomena, and how the differences in thermal energy change the effects of bias voltage. These questions reduce to mapping the dynamic phase diagram of dislocations as a function of external voltage and temperature.

There are two complementary tuning parameters we have to modify and induce the dynamics of ion movement: a DC voltage supply and a global temperature control. Beginning at a set temperature without an applied bias, we will scan the sample to identify ion vacancy density using the coherent beam. If the identified vacancies are static over a timescale of roughly minutes, we will gradually ramp up the voltage until we observe dynamics. We expect timescales on the order of minutes for

This measurement will be repeated for the same sample at multiple temperatures, as well as for multiple samples of a different age in order to confirm the effects of aging on defect concentration. We will use the two-time correlation function and higher order correlation analysis of XPCS data to determine if the dynamics are intermittent or continuous, and whether or not they show aging, divergent relaxation timescales, and glassy dynamics. Finally we will repeat the above measurements on different parts of the sample to get better statistics and eliminate outliers.

We aim to understand the effect of our tuning parameters, which are voltage and temperature, on the dynamics of ion movement. Specifically, we will address questions of the rate of vacancy diffusion and the time to come to equilibrium.

7.2.3 Experimental results

Grace Luo of David Fenning's group provided the main samples and optical images, shown in Figures 7.19a and 7.23a. X-ray diffraction was used to characterize the samples in Figure 7.19b. The perovskite nanocrystals were spin coated onto glass containing two sets of electrodes with 5 nm Pt and 30 nm Au; a larger rectangular pad, and an identical pad with smaller finger electrodes emanating towards the other electrode.

Pritesh Parekh of Shirley Meng's research group provided a separate set of samples along with SEM images and X-ray diffraction, shown in Figures 7.20a and 7.20b, respectively. The crystals in these samples were extracted from a larger perovskite single crystal and hand-placed using a focused ion beam (FIB). Unfortunately, due to the much larger particle size for many of these samples, we were unable to use them for XPCS or BCDI, although diffraction rocking curves were collected for posterity.

The entire experiment was performed at room temperature, as time did not allow for additional testing of parameters.

Several crystals which had landed with solid connections to both electrodes, and without too many additional nearby crystals in the detector's field of view, were picked for measurement. For each sample, if multiple crystals suitable, we would connect only one at a time using the wire bonding. Copper tape was stuck to the large part of each gold and platinum electrode, and copper wire is soldered onto the Cu tape. Wire bonds are connected between a finger electrode and the larger pad, or the Cu tape itself if needed.

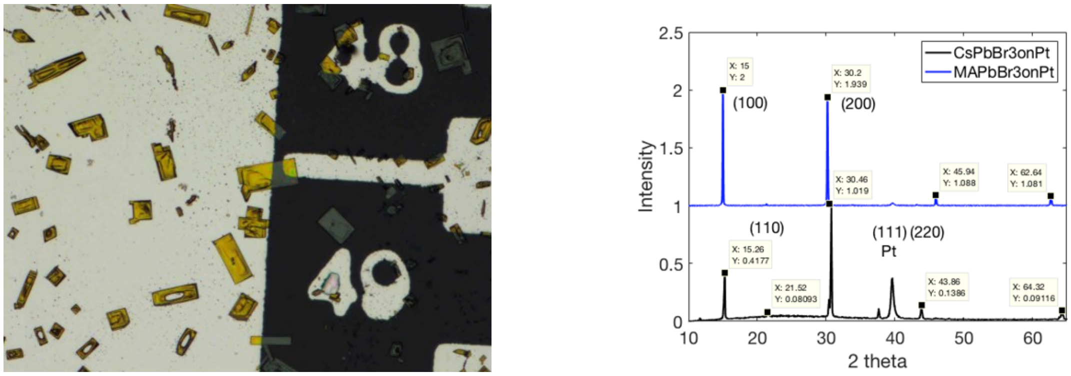

(a) Optical image of $CsPbBr_3$ crystals used during XPCS experiment.

(b) $CsPbBr_3$ and $CH_3NH_3PbBr_3$ X-ray diffraction on Pt finger electrodes. Only the fully-inorganic sample was used for this set of samples.

Figure 7.19: $CsPbBr_3$ XPCS sample information. The crystals were prepared by a spin coating method, with an element of randomness as to whether a crystal lines up between two electrode pads.

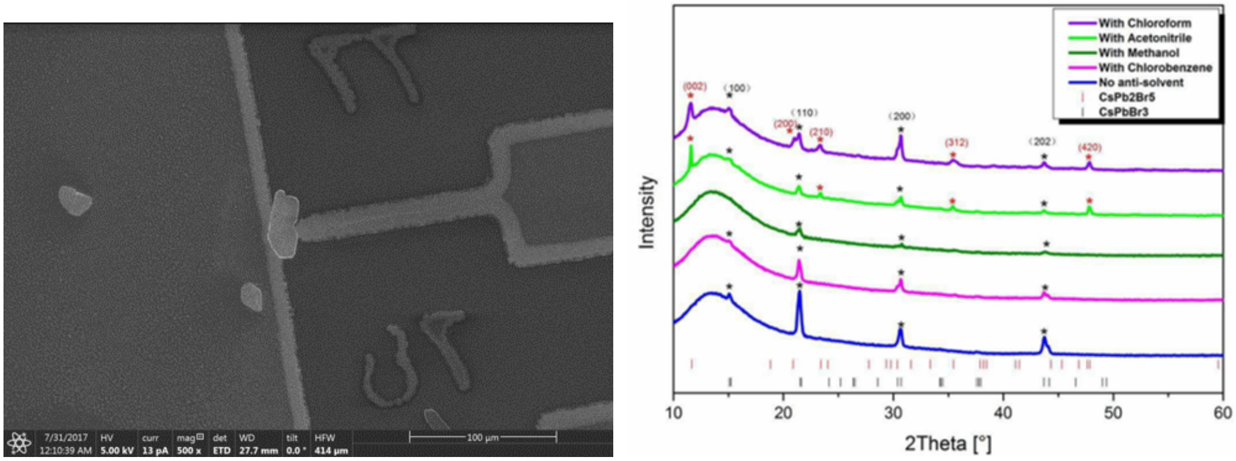

(a) SEM of $CsPb_2Br_5$ on Pt finger electrodes.

(b) $CsPb_2Br_5$ and $CsPbBr_3$ X-ray diffraction on Pt finger electrodes. Also shown is the effects of having specific solvents used during synthesis.

Figure 7.20: $CsPb_2Br_5$ and $CsPbBr_3$ XPCS sample information. The crystals were prepared by using a focused ion beam (FIB) to cut out small chunks, which were then hand-placed onto the connecting electrodes.

In order to locate the correct perovskite nanocrystals after wire bonding, we first took long linescans of the entire electrode using an X-ray fluorescence detector aligned to the platinum peak, one of the two components of our electrodes. The resulting sinusoidal pattern (see Figure

7.22) was used to move to a particular finger electrode that had been predetermined using the optical images and contained the crystal connected to the larger electrode pads.

After moving to the specific finger electrode, we mapped the surrounding area using the same X-ray fluorescence technique. This was compared to the optical images taken prior to the experiment to ensure we had picked the correct crystal. Additional smaller mesh scans (not shown) were taken to map out angular dimensions to locate the final diffraction peak.

Summary of procedure for each sample

1. Solder Cu wire onto Cu tape with pin connectors
2. Attach Cu tape onto adjacent to Au pads
3. Wire bond 2 wires from electrodes to Cu pad (and 3rd safety bond shorting the crystal)
4. Use combination of linescans and mesh scans of Pt peak to map out finger electrodes
5. Locate crystal using optical images, Pt peak maps, as well as mapping perovskite location along both χ and θ directions.

As with many of the X-ray measurements, stability under the beam was the biggest issue. Two factors were found to be relevant. Firstly, larger crystals maintained a stable X-ray speckle intensity for longer (with the largest appearing stable overnight). This is not unexpected, and reflected our results with BCDI measurements on smaller versions of the same material. Secondly, crystals that were physically connected to the metallic electrodes also fared significantly better compared to crystals resting solely on the glass. This may have been due to their being somewhat electrically grounded.

Chapter 7 is not currently being prepared for publication. Thanks to my collaborators G. Luo, P. Parekh, S. Wang, A. Shabalin, J. Wingert, J. Ruby, N. Hua, S. Hrkac, S. Hy, R. Harder, E. Maxey, J. Masser, D. Fenning, Y.S. Meng, and O.G. Shpyrko.

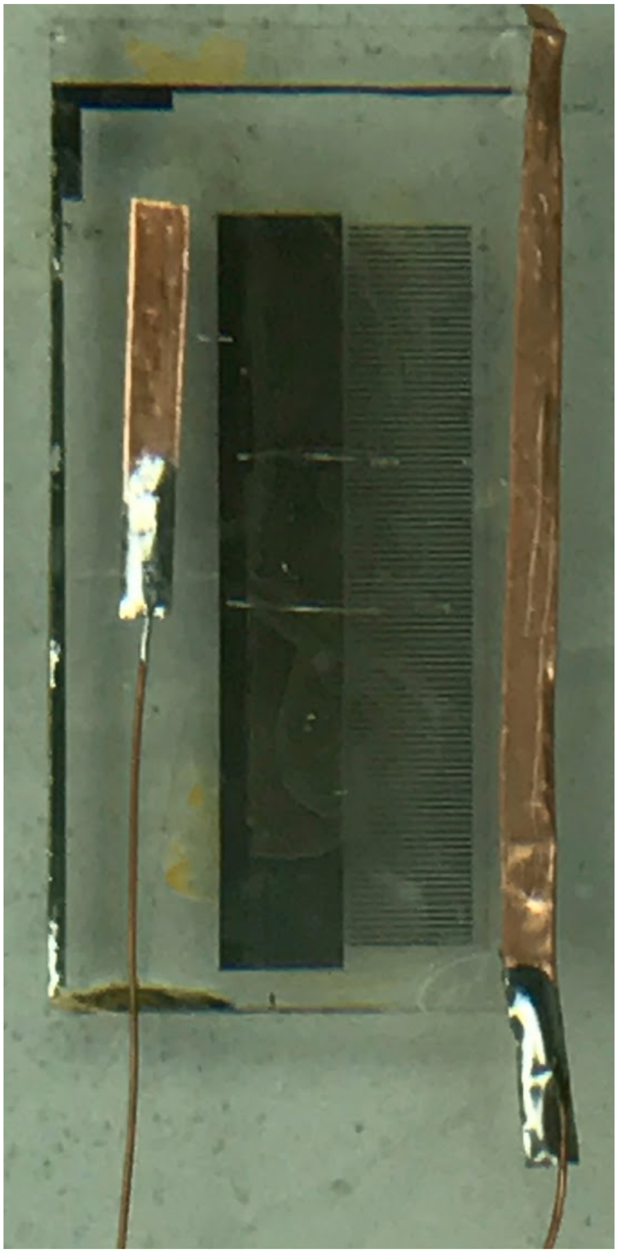

(a) A wire-bonded perovskite sample for XPCS. The wire bonds are visible as thin vertical strands near the center of the image. The Cu tape is stuck to the large part of each Au/Pt electrode, and wire is soldered onto the Cu tape. Wire bonds are connected between the finger electrodes and the larger pad, or the Cu tape itself if needed. The wires are soldered to a BNC connector which allows for a sealed sample chamber while applying a voltage across the sample.

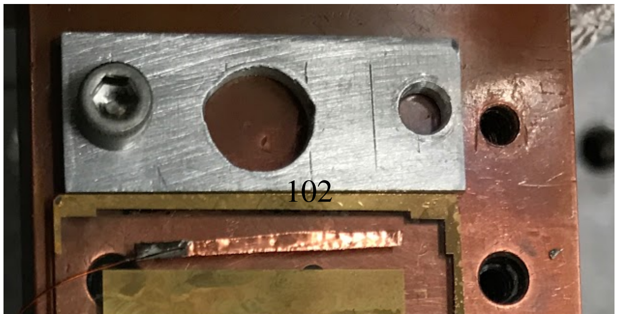

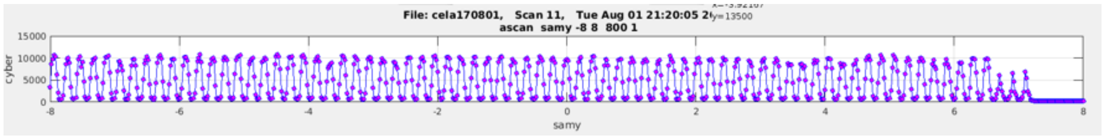

Figure 7.22: X-ray fluorescence linescan of Pt finger electrodes. This was used to determine where the finger electrode containing the wire bonded perovskite crystal was located on the sample.

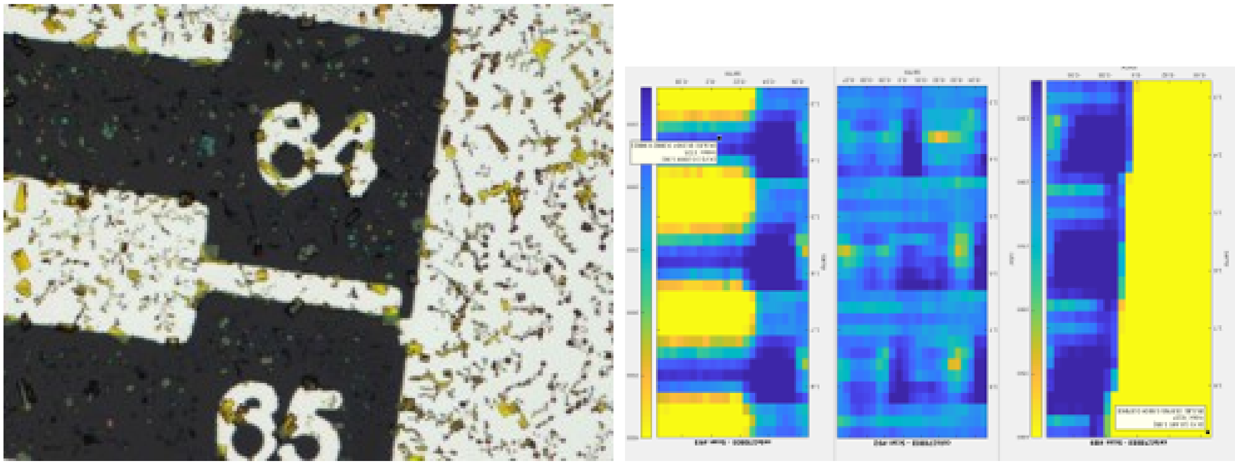

(a) Optical image of $CsPbBr_3$ crystals used during experiment.

(b) X-ray fluorescence mesh scan of Pt finger electrodes. This, along with the corresponding optical images and the linescan seen in Figure 7.22, was used to locate the precise location of the wire bonded perovskite nanocrystal

Figure 7.23: In order to locate the correct perovskite nanocrystals, we mapped the surrounding area using X-ray fluorescence scans of platinum, a thin layer making up the finger electrodes. This was compared to the optical images until we were certain that we had picked the correct crystal. Additional smaller mesh scans (not shown) were taken to map out angular dimensions to locate the final diffraction peak.

Appendix A

$CH_3NH_3PbBr_3$ hybrid perovskite solar cell synthesis and cell design

More than 150 solar cells were fabricated in the process of learning the fabrication procedure optimized by the group of Shirley Meng. Ambient conditions were found to play a critical role in the final efficiency, as high levels of humidity quickly degrade the perovskite material and reduce performance. The NanoEngineering building's modern open-concept spaces may look nice, but was detrimental to this work.

All materials, unless stated otherwise, were purchased from Sigma Aldrich and used as received. Spiro-MeOTAD was purchased from Merck KGaA.

A.1 Synthesis of CH_3NH_3I

CH_3NH_3I was synthesized with the following steps. 14 mL methylamine (40% in methanol, TCI) and 15 mL hydroiodic acid were mixed at 0° C and stirred for one hour. The solution was evaporated at 90° C for one hour to obtain the deep-brown primary product. The product was re-dissolved in ethanol at 70° C, precipitated and washed with diethyl ether several times. Finally, the product was dried at 60° C in a vacuum oven for 24 hr.

A.2 Device Fabrication

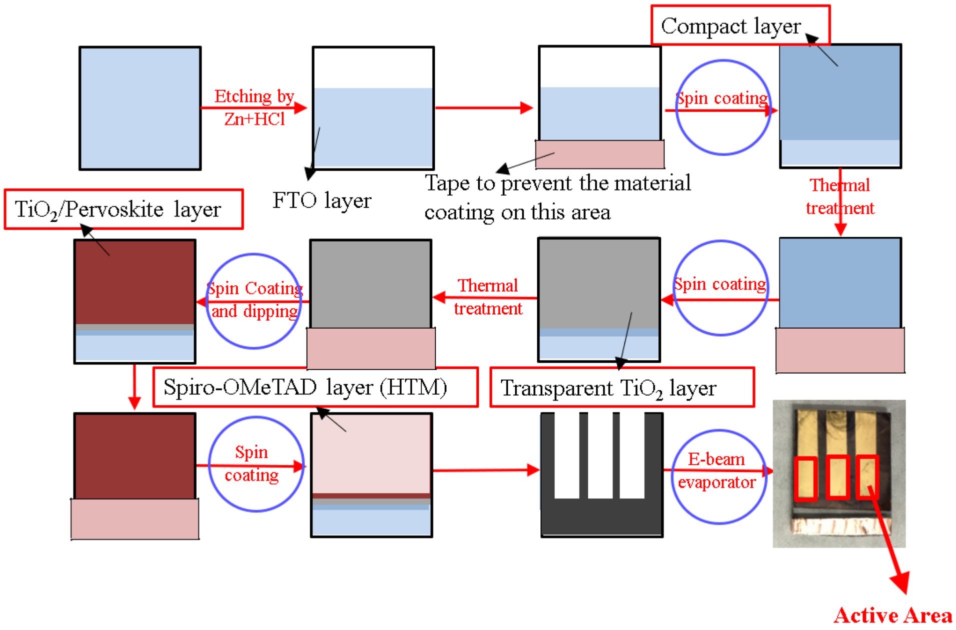

Figure A.1: Fabrication procedure for $CH_3NH_3PbI_3$ outlining the steps to create a full perovskite solar cell.

Perovskite solar cells were fabricated using the sequential deposition method[143] also shown in Figure A.1. FTO glasses (Pilkington, TEC-15) were cleaned by an ultrasonic bath with detergent water, alkaline ethanol solution, and deionized water, sequentially; each cleaning step lasted for 15 min. Then, the oxygen plasma cleaning step was applied for 10 min to remove the last traces of organic residues on the slides.

The TiO_2 compact layer was spin coated on the FTO substrates at 800 rpm for one minute using 0.24 M titanium isopropoxide in 5 mL ethanol solution. The films were annealed at 500° C for 30 min. After cooling down to room temperature, the films were immersed in 0.03 M aqueous TiCl 4 solution at 70° C for 40 min and then gradually heated at 500° C for 40 min after washing with deionized water. Commercial TiO_2 paste (Dyesol 18-NRT) diluted in ethanol (2:7 weight ratio) was spin-coated on the films at 5,000 rpm for 30 s and the film was annealed at 450° C for 40 min to form the mesoporous TiO_2 layer.

The PbI_2 solution (1 M) was prepared by dissolving 462 mg PbI_2 in 1 mL N,N-dimethylformamide (DMF) stirring at 80° C. The solution was spin coated on the films at 5000 r.p.m. for 90 s. After spinning, the films were dried at 80° C for 30 min and dipped in 2-propanol for 2 s. Then the pre-wetted films were dipped in a solution of CH_3NH_3I in 2-propanol (10 mg/ml) for 2 min and dried at 80° C for 30 min.

The 2,2,7,7-teterakis(N,N-di-p-methoxyphenylamine)-9,9-spirobifluorene (Spiro-OMeTAD) solution was prepared by 100 mg of Spiro-OMeTAD, 28.8 μL 4-tert-butyl pyridine (tBP) and 17.7 μL lithium bis(trifluoromethanesulfonyl)imide (LiTFSI) solution (520 mg LiTFSI in 1 mL acetonitrile) in 1 mL of chlorobenzene. The solution was spin coated on the $CH_3NH_3PbI_3$ layers at 3,000 rpm for 60 s. Finally, 80 nm of gold was e-beam evaporated on the Spiro-OMeTAD-coated film. Devices for measuring the resistance of the hole conductor were fabricated as follows with the Spiro-OMeTAD solution identical to that used for the PSC fabrication, the solution spin coated on glass substrates with/without perovskite $CH_3NH_3PbI_3$ layer (the perovskite $CH_3NH_3PbI_3$ layer was prepared as the same procedure as the PSC) at 3,000 rpm for 60 s, the Spiro-OMeTAD coated films covered with a 100 μm width spacer, and finally 80 nm of gold evaporated on the sample using an electron beam evaporator..

A.2.1 Itemized fabrication procedure

1. Cut glass into 2-2.5” pieces.
2. Etch the FTO layer(0.5”) with Zn powder and HCl (16.5 mL HCl/ 33.5 mL DI water) and clean it.
3. Cleaning glass:

   Hand wash with detergent and water for 10 min

Sonicate with EtOH/KOH solution for 10 min

Sonicate with DI water for 10 min

Sonicate with fresh DI water for 10 min

4. Dry the clean glass with N_2 air-gun then do plasma treatment for 10 min
5. Compact Layer: 5 mL EtOH, 350 μL TTIP, 5.81 μL HCl Spin coat at 800 rpm/60s.
6. Sinter in box furnace:

   Increase to 100° C over 10 min, maintain for 10 min

   Increase to 200° C over 10 min, maintain for 10 min

   Increase to 300° C over 10 min, maintain for 10 min

   Increase to 400° C over 10 min, maintain for 10 min

   Increase to 450° C over 10 min, maintain for 30 min
7. $TiCl_4$ treatment: 3% $TiCl_4$ solution (1 M) in DI water. Heat at 70° C in oven for 40 min, then washed gently by water.
8. Sinter with the same conditions used for the compact layer.
9. Plasma treatment for 10 min
10. TiO_2 mesoporous layer: 2:7 weight ratio (TiO_2 18 NR-T : EtOH), 5000 rpm/30 s
11. Sinter in box furnace:

    Increase to 80° C over 10 min, maintain for 30 min

    Increase to 200° C over 10 min, maintain for 10 min

    Increase to 300° C over 10 min, maintain for 10 min

    Increase to 400° C over 10 min, maintain for 10 min

Increase to 450° C over 10 min, maintain for 30 min

12. Plasma treatment for 10 min
13. PbI_2 layer: 0.472 g/mL DMF heat at 100° C, keep heating during spin coating. Spin coat PbI_2: 5000 rpm/90 s, heat at 80° C for 30 min
14. Dip in the solution of CH_3NH_3I (10 mg/mL normally prepare 1 g CH_3NH_3I in 100 mL IPA) in IPA for 2 min. Use air gun to blow away residual material ASAP. Heat at 80° C for 30 min
15. Spiro-OMeTAD layer: 122.5 mg Spiro in 1 mL CB with 17.7 μL LiTFSI (520 mg/mL in AN) heat at 100° C and then add 28.8 μL tBP before spin. When spinning, wait 40 s to ensure the precursor has infiltrated to TiO_2. (3000 rpm/60 s).
16. Electrode layer: Use electron-beam evaporator to create an 80 nm-thick gold electrode (rate of 1 Å/s).

A.3 Device Characterization

Photocurrent density and voltage (J-V) were measured with a solar simulator with a 150 W xenon lamp (Solar Light SL07265, equipped with an AM1.5G filter, calibrated with a standard Si solar cell to simulate AM1.5 illumination at 100 mW/cm^2) and a Keithley 2400 source meter. Before the J-V test, the solar simulator was marked with a 450 nm long pass filter to illuminate the perovskite solar cell for one hour and test its efficiency at 0 min, 10 min, 30 min, and 60 min.

Electrochemical Impedance Spectra (EIS) were conducted using a Solartron 1287 electrochemical interface coupled with a Solartron 1455A frequency response analyzer. A 10 mV perturbation was applied, and the frequency was from 1 MHz to 1 Hz. The solar cell was illuminated by the solar simulator which was integrated with the 450 nm long pass filter for 60 min, and the solar cell was tested by the EIS at 0 min, 10 min, 30 min, and 60 min respectively.

Resistance of the hole conductor was tested by four-point probe (Jandel Four-Point Probe with RM3000 Test Unit) measurement with the devices mentioned before in dark condition. The curves on the devices, which were created by the 100 μm spacer, were set between the second and third probe during the test. Before testing, the devices were illuminated on solar simulator with full light, 380 nm long pass filter and 450 nm long pass filter for 0 min, 10 min, 20 min, 30 min, 40 min and 60 min, respectively.

Appendix B

Proposed inelastic neutron scattering experiment of $CH_3NH_3PbI_3$ with phonon mode simulations

B.1 Goal of Experiment

Inelastic neutron scattering experiment in combination with *in situ* electrochemical impedance spectroscopy (EIS) in order to see possible phonon modes responsible for ionic defect movement in these hybrid perovskites.

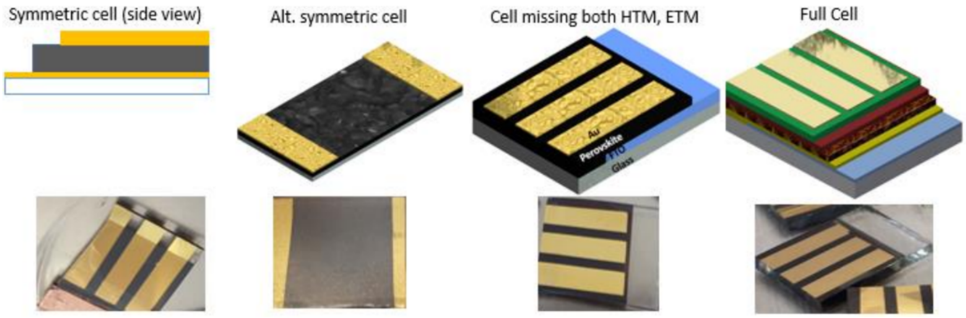

Figure B.1: Several cell architectures that were used in the EIS study.

B.2 Theoretical justification: Density functional theory (DFT) and density functional perturbation theory (DFPT) of hybrid perovskites

B.2.1 Geometrical relaxation

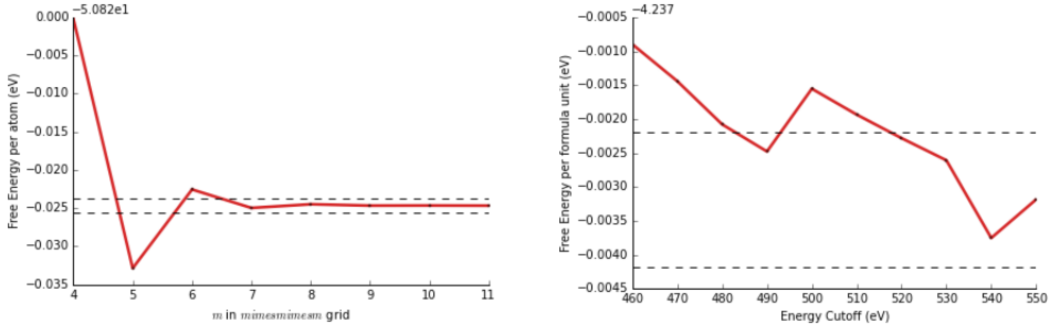

(a) k-point grid convergence (b) Cutoff energy convergence

Figure B.2: The energy was converged to 530 eV, and the *k*-point grid converged at a 7×7×7 grid density for the cubic structure, with the larger tetragonal and orthorhombic structures using a 7×5×7 grid

VASP was used to perform a density functional theory (DFT) calculation with the generalized gradient approximation (GGA). The plane wave cutoff energy was converged to 530 eV, and a 7×7×7 Γ-centered *k*-point grid was used with the PAW-PBE ultrasoft pseudopotentials.

The bond angles for the fully relaxed structures were all within 5% of the experimental values.

Comparison of relaxed and fixed organic cation

I performed both a full relaxation as well as a selective relaxation of the inorganic lattice around a fixed organic methylammonium cation. For the general lattice parameters, it was found that keeping relaxing the inorganic lattice around a fixed organic methylammonium cation resulted

Table B.1: A comparison of the lattice vectors between experimental neutron diffraction data[24] and our DFT-GGA calculations.

Experimental	**a** (Å)	**b** (Å)	**c** (Å)	α	β	γ
Orthorhombic (100 K)	8.87	8.58	12.62	90	90	90
Tetragonal (180 K)	8.80	8.80	12.71	90	90	90
Cubic (352 K)	6.32	6.32	6.32	90	90	90
DFT-GGA						
Orthorhombic	8.51	9.24	12.92	90.58	90.12	90.14
(with fixed MA)	8.42	9.16	12.79	90.54	91.39	91.18
Tetragonal	8.85	8.87	13.08	89.57	89.49	89.97
(with fixed MA)	8.76	8.78	12.92	89.44	89.31	89.98
Cubic	6.41	6.39	6.44	90.00	90.40	90.00
(with fixed MA)	6.36	6.31	6.35	90.00	90.34	90.00

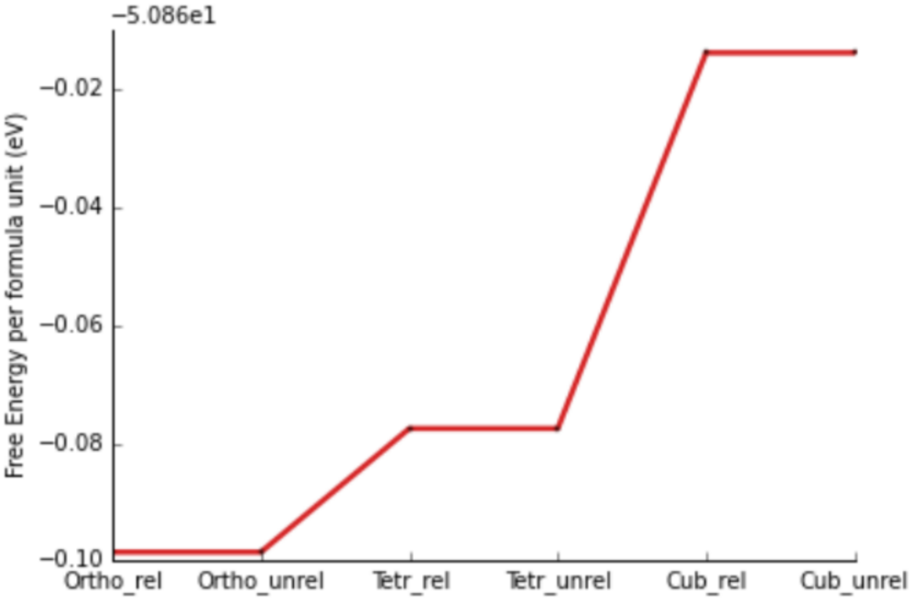

Figure B.3: The final free energy of the three phases, with both a completely relaxed structure and a fixed organic cation shown next to each other.

in more accurate lattice parameters.

A second relaxation was performed for each calculation to ensure that it was fully relaxed, as seen in Figure B.4.

Table B.2: A comparison of the Pb-I-Pb bond lengths and angles between experimental neutron diffraction data[24] and our DFT-GGA calculations, for the fully relaxed structures. The average angle and bond length were taken for the DFT calculations.

Experimental	**Pb-I-Pb Bond Length** (Å)	**Pb-I-Pb Bond Angle** (degrees)
Orthorhombic	3.20	161.94
	3.19	150.75
Tetragonal	3.17	157.92
	3.17	180
Cubic	3.16	180
DFT-GGA		
Orthorhombic	3.26	167.35
	3.24	150.43
Tetragonal	3.22	151.75
	3.28	175.10
Cubic	3.23	171.29

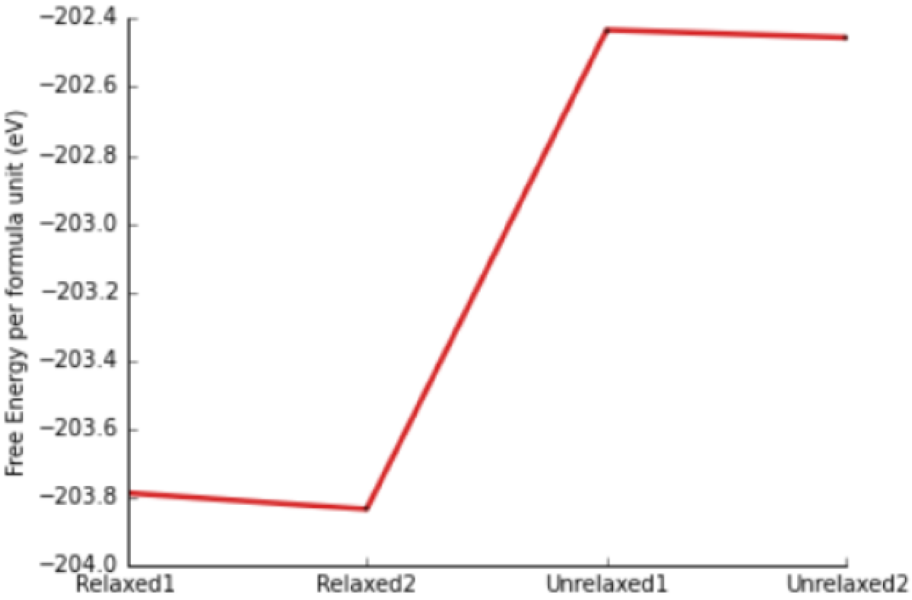

Figure B.4: This plot uses data from the relaxation of the orthorhombic structure. The first two data points are the energies of the first and second relaxation, with all atoms allowed to move. The last two data points are the energies of the first and second relaxation when the MA cation is fixed.

Table B.3: The same comparisons, using a fixed MA cation in the DFT calculation. Again, the average angle and bond length were taken for the DFT calculations.

Experimental	**Pb-I-Pb Bond Length** (Å)	**Pb-I-Pb Bond Angle** (degrees)
Orthorhombic	3.20	161.94
	3.19	150.75
Tetragonal	3.17	157.92
	3.17	180
Cubic	3.16	180
DFT-GGA		
Orthorhombic	3.22	166.89
	3.23	148.68
Tetragonal	3.16	151.03
	3.24	173.45
Cubic	3.19	174.08

B.2.2 Phonon calculations using density functional perturbation theory

There are two main methods for calculation of the Hessian matrix of force constants, the finite difference method and DFPT. The two methods will typically yield similar results at high-symmetry points such as the Γ-point. However, as the wave vector increases there are significant differences. At high frequencies small inaccuracies in force field models become greatly magnified, compared to the DFPT results which have no anharmonic contributions. The finite difference method, however, can be useful if you want to create force field models for use in ab-initio molecular dynamics simulations.

The first method uses the so-called frozen phonon approximation. This method is generally quicker and computationally cheaper than using the linear response approximation, which utilizes density functional perturbation theory to calculate forces. One drawback of the frozen-phonon method is that large supercells are needed to accurately calculate the force constant matrix. The periodic boundary conditions used in DFT calculations can cause problems for the frozen phonon method. Displacing one atom in a small unit cell creates forces on all the atoms in the same unit cell, but also on the periodic images of these atoms. The frozen-phonon method can be restricted in application as compared to DFPT: for example, it cannot readily be used to calculate the response of crystalline systems to electric field perturbations, and cannot, without large computational effort, calculate phonon responses at arbitrary wavevector. DFPT also includes the long-range polarization fields due to optical phonons.

The second method relies on density functional perturbation theory (DFPT). DFPT is a very powerful and accurate method for computing the vibrational and dielectric properties of extended systems, as well as of any other properties expressed in terms of low-order derivatives of the electronic ground state energy. The dynamical matrix of the crystal gives the forces acting on individual atoms due to the displacements from equilibrium of other atoms. In the harmonic approximation (which we take) this force is the integral of the electron charge-density response to the displacement form equilibrium of one atom, times the variation of the ionic potential due to the displacement of another. The "meat" of the calculation of the dynamical matrix is the electron density response to linear atomic displacements from equilibrium. This linear response is what is calculated within DFPT.

The self-consistent equations from DFT can be rewritten as a large linear system with a dimension equal to the number of plane waves in the basis set times the number of occupied states. For each independent atomic displacement in the crystal, this huge linear system is solved using a conjugate-gradient algorithm. The number of linear systems to be solved is three times (the number of independent polarizations) as large as the number of inequivalent atoms. Symmetry considerations can reduce this number. A last linear system, corresponding to the perturbation due to the application of a homogeneous electric field, is solved in order to calculate the polarizability.[144, 145]

B.3 Vibrational properties of $CH_3NH_3PbI_3$

The Generalized Gradient Approximation (GGA) by Perdew Burke and Ernzerhof adjusted for use in solids (PBEsol) as implemented in the Vienna Ab-initio Simulation Package (VASP) was used.[146, 147] We tested the cubic phase of a hybrid perovskite in Stampede using density functional perturbation theory (DFPT), implemented in VASP. The plane wave cutoff energy was converged to 530 eV, and a 7×7×7 Γ-centered *k*-point grid was used with the PAW-PBE ultrasoft pseudopotentials. The forces were relaxed below 1 meV/Å.

Initial DFPT calculations of all three phases of methylammonium lead iodide (the orthorhombic, tetragonal, and cubic phase) reveal that they have significant computational expense. Since the DFPT calculations cannot be continued using a half-completed job, the number of cores must be increased in order to keep the calculation shorter than 48 hours. Calculations using the finite difference method, on the other hand, are more readily optimized as each calculation may be submitted separately. However, as mentioned previously, FDM cannot easily calculate the phonon responses at arbitrary wavevector as well as the long-range polarizations due to optical phonons. One can also use DFPT results to easily calculate the IR spectrum of the material.

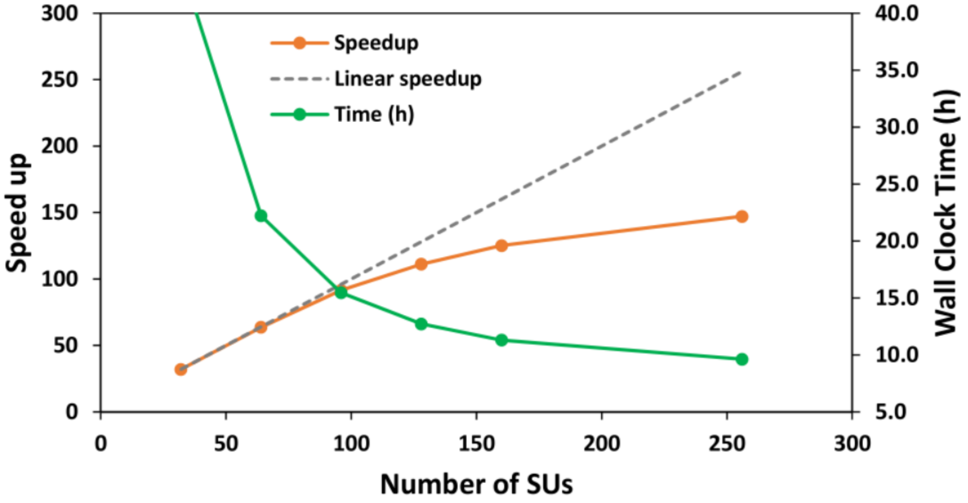

Figure B.5: Scaling performance of VASP calculations for bulk hybrid perovskite composed of 96 atoms ∼12.5 Å per side in a cubic supercell.

We tested the scaling performance of a cubic perovskite supercell of 96 atoms, ∼12.5 Åper side. In order to measure the efficiency of a calculation as a function of the number of cores, we define the speed up as (the expected time of a calculation / the wall clock time) × the number of cores. The expected time of a calculation is measured from (32 cores × 44.2 hours) / the number of cores, since we set (32 cores × 44.2 hours) as the reference which is the total amount of SUs required in $CH_3NH_3PbI_3$ calculation. We conclude that the optimized number of cores in this test is 96.

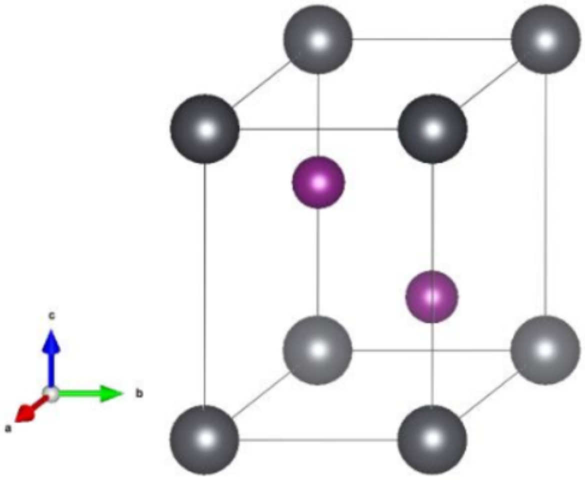

Figure B.6: Crystal structure of a single unit cell of lead iodide. The lead is gray, and iodine purple.

The structure and vibrational modes of lead iodide was first used, both as a comparison to the hybrid perovskite, as well as to test the accuracy of the DFPT method, since there are published works on single-crystal PbI_2 to compare to (see Figure B.7).

After successful simulation of simpler structures such as lead iodide and silicon metal, I moved on to the hybrid perovskites (see Figures B.8 and B.9).

The tetragonal $CH_3NH_3PbI_3$ structure is ∼1 meV/atom higher free energy than the orthorhombic structure, and the cubic phase is ∼6 meV/atom higher energy than the tetragonal structure. The three have very distinct energies when comparing the fully relaxed phases. The bond lengths and angles were within a few percent of experimental values.

Theoretical predictions place the activation energy for ion movement (either methylammonium or iodide vacancies) between 0.1–0.7 eV. In a working perovskite solar cell with a

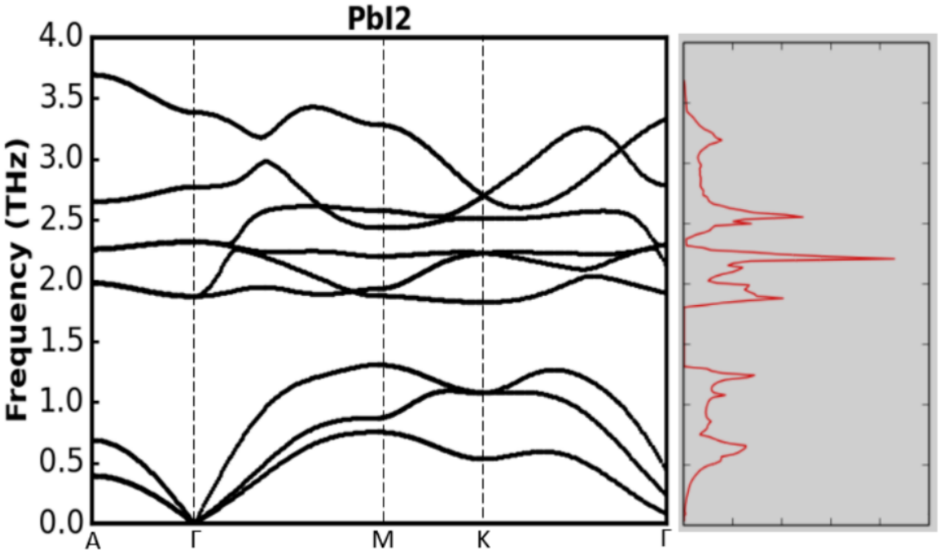

Figure B.7: Calculation of phonon bandstructure and density of states in lead iodide, using the finite difference method with a 4×4×2 supercell. Summing the phonon bandstructure at each frequency yields the density of states.

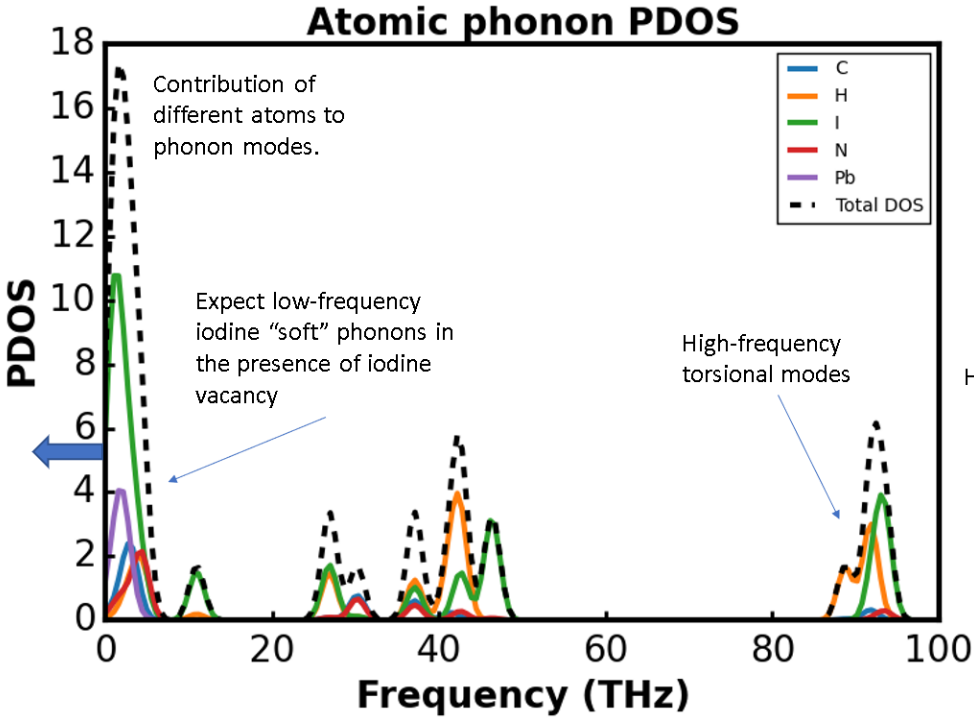

Figure B.8: Orthorhombic $CH_3NH_3PbI_3$ atomic phonon density of states

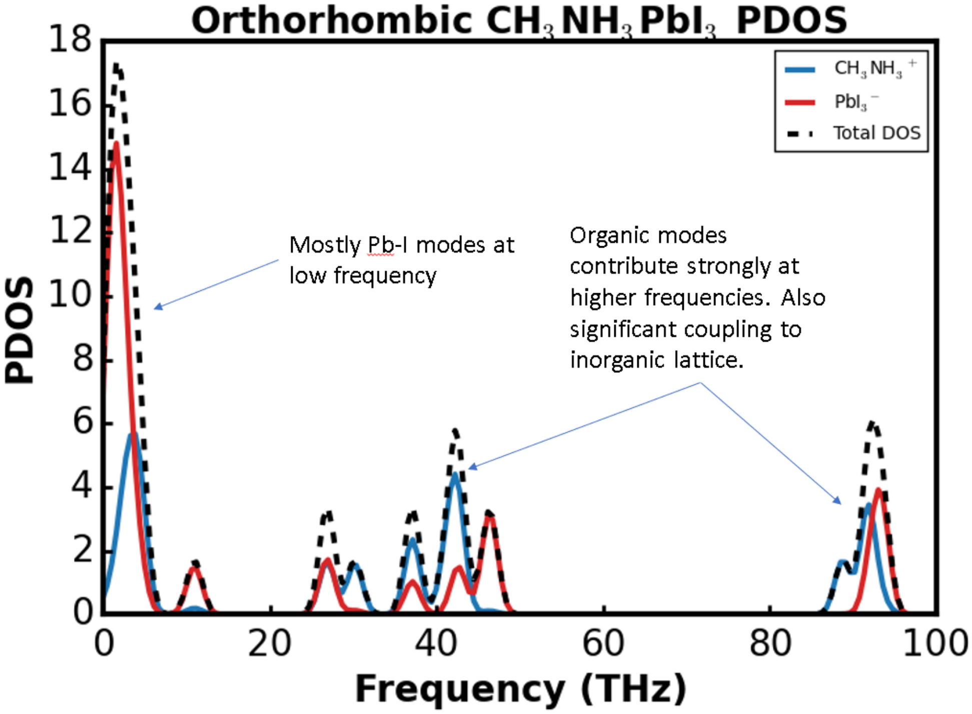

Figure B.9: Orthorhombic $CH_3NH_3PbI_3$ phonon density of states, separating the organic and inorganic vibrational components

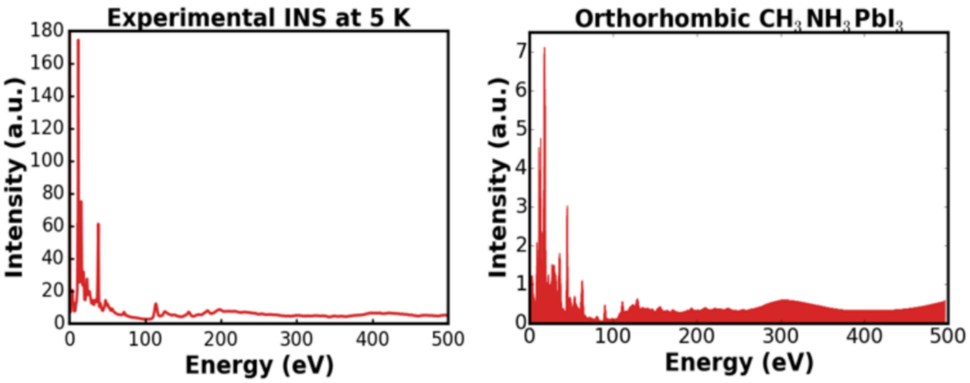

Figure B.10: Experimental (left) and simulated (right) neutron scattering spectrum of orthorhombic phase of perovskite. The experimental spectrum was a 5 min measurement time at the VISION instrument, at 5 K.

300 nm-thick layer of perovskite semiconductor and a 1 V open circuit voltage, the electric field is roughly 3 V/μm. This places severe limitations on our device architecture, particularly the separation of electrodes. As the Solartron is limited to below 75 V, we can have at most a 30 μm

thick layer of perovskite, making it difficult to use pellets. The alternative symmetric cell, seen in Figure B.1, is thus impractical without a high-voltage power supply.

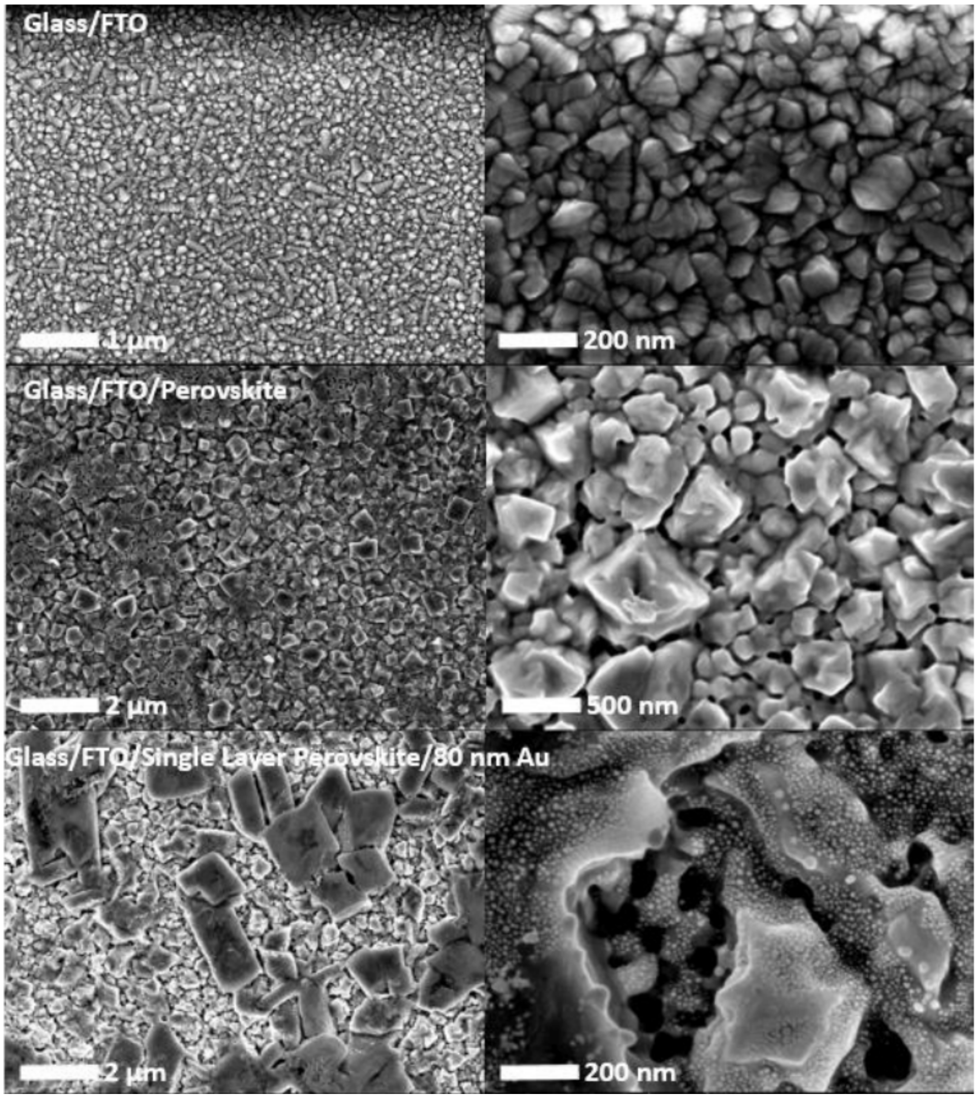

Figure B.11: With only a single layer of perovskite on FTO, the perovskite grain size has a wider distribution and the gold has incomplete coverage on the top layer.

Scanning electron micrographs of the individual layers in the first and third architectures of Figure B.1 are shown in Figures B.11 and B.12, respectively. The coverage of the gold layer on the perovskite is highly improved when the particle size distribution is narrower and on average larger.

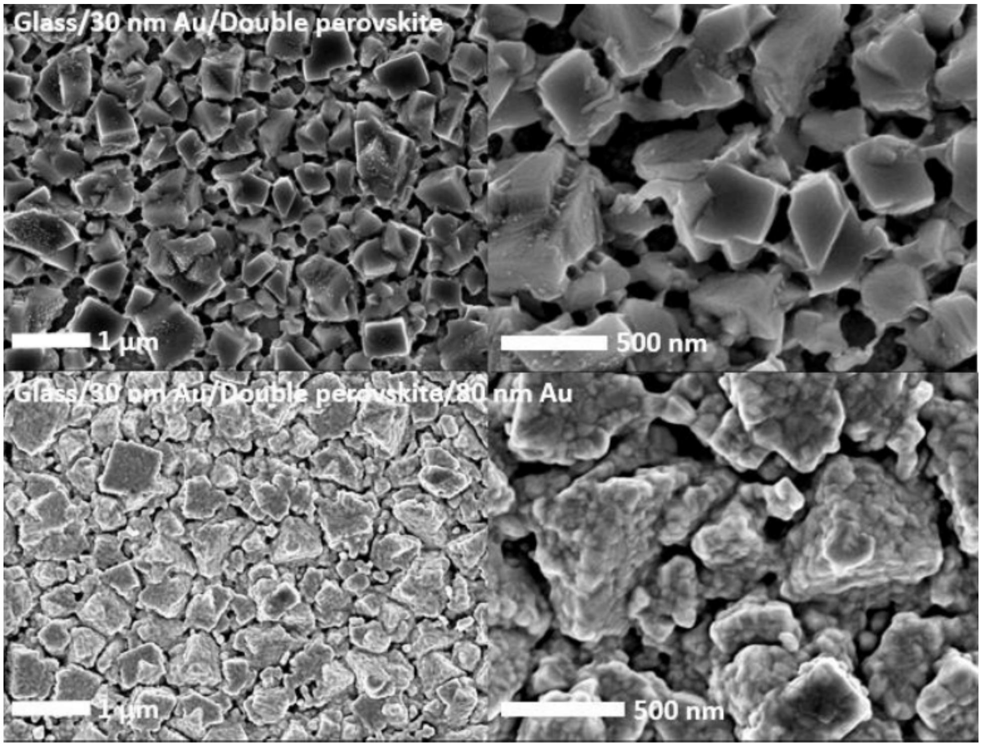

Figure B.12: With a double layer of perovskite on gold, the average grain size is higher and most grains are the same size. Due to the better coverage of the perovskite, the top gold electrode can fully coat the perovskite..

B.4 Precedent for experiment and expected results

Theoretically, the changes in the neutron spectrum due to defect scattering is possible and is used regularly in quasielastic neutron scattering.[148]

Experimentally, Luke Daemen, the beamline scientist I was working with, has recently used inelastic neutron scattering (INS) with *in situ* electrochemical impedance specroscopy (EIS) in studying both Li-ion battery electrolytes as well as hydrogen fuel cell materials. He has also helped users to perform more traditional INS measurements on hybrid perovskite powders.[149–152]

During our measurements, one can tune the EIS instrument frequency near a “hopping” frequency characteristic to defect movement. As a defect diffuses through the structure, they will cause an instability in the crystal structure, leading to a softening of specific phonon modes (*i.e.* reduction of frequency for particular peaks).

The phonons related to iodine (or any other ion) movement can be extracted from the theoretical spectrum and compared to the experimental one.

Some research have observed a Warburg-like diffusion in the low frequency range between 0.01 and 50 Hz. It has been ascribed to ionic transport or ferroelectric effects. The low-frequency EIS features tend to become obscured and finally disappear at lower temperatures.[153] Due to the Debye-Waller factor and the amount of hydrogen in our system, measurements at room temperature will be difficult.

B.5 Preparation (before experiment)

- Use same synthesis as below, only small amount necessary
- Use XRD to check purity
- Pellet testing

  2 g powder, pressed into 10-12 mm pellet in glovebox

  Placed into coin cell and crimped

- Synthesis (one example, used by Shen and I previously)

  One molar solution containing PbI_2 and MAI was prepared in GBL. The iodide solution was heated up to 60° C. The solutions were filtered using PTFE filter with 0.2-mm pore size. Two mL of the filtrate were placed in a vial and the vial was kept in an oil bath undisturbed at 110° C. All procedures were carried out under ambient conditions and humidity of 55–57%. The crystals used for measurements were grown for 3 hr. The reaction yield for $CH_3NH_3PbI_3$ was calculated to be 11 wt %, respectively.

B.6 Experimental Plan

1. Solder leads to either side of electrode
2. Load into sample holder (sealed vanadium canister, opaque, Ar environment)
3. Temperatures to be used: 5 K, 160 K, 300 K, 450 K.
4. Apply ~3 V/mm bias, 100 mV AC voltage.
5. Measure at 7 frequencies for each temperature (0.01 Hz, 0.1 Hz , 1 Hz, 10 Hz, 100 Hz, 1 kHz, 1 MHz) for 30 min-2hr each, dependent on size of pellet. Focus will be placed on low-frequency features.

B.7 Questions and Challenges

Which ion is actually moving? In the literature there are a number of theoretical and experimental works that disagree with each other on both the activation energy for ionic diffusion as well as the ions in question. The leading contenders right now are iodide vacancies, proton interstitials, and $CH_3NH_3^+$ vacancies (they have been shown to quickly exchange with $CH(NH_2)_2^+$ cations, showing that they can be quite mobile).[153–157]

Does particle size have an effect on the results? Signal due to surface phonon effects is typically small as well as separated in frequency from their bulk phonon counterparts. It is more important to confirm that there is good electrical contact between particles and that the particle size is similar to that used in functioning perovskite solar cells.

How strong of a shift can we expect? This depends on the ion in question as well as how each will interact with the lattice. Although this question is well understood with respect to quasielastic neutron scattering, it is less so with INS. The peak shift is affected both by the fraction of material that has defects as well as the material temperature. (which will slow down the dynamics at the low temperatures we typically would want to use with INS)

How does this translate to a working perovskite solar cell? This technique will probe bulk phonons and not account for grain boundary effects. Although many of these ion defects will be first present at the grain boundaries, they will move through the structure itself (and this is and assumption of all theoretical calculations done in the literature). Besides indirectly confirming the identity of the diffusing defect(s), showing how it moves through the structure could lead to later improvements by modification of the crystal structure itself. For example, MA^+ movement could mean that an alternative central cation could decrease ion movement and hysteresis. Later work using different perovskite structures ($CH(NH_2)_2PbI_3$, PbI_3, $CH_3NH_3PbBr_3$, $CsPbI_3$, etc.) was planned. simulator with a 150 W xenon lamp (Solar Light SL07265, equipped with an AM1.5G filter, calibrated with a standard Si solar cell to simulate AM1.5 illumination at 100 mW/cm^2) and a Keithley 2400 source meter. Before the J-V test, the solar simulator was marked with a 450 nm long pass filter to illuminate the perovskite solar cell for one hour and test its efficiency at 0 min, 10 min, 30 min, and 60 min.

Electrochemical Impedance Spectra (EIS) were conducted using a Solartron 1287 electrochemical interface coupled with a Solartron 1455A frequency response analyzer. A 10 mV perturbation was applied, and the frequency was from 1 MHz to 1 Hz. The solar cell was illuminated by the solar simulator which was integrated with the 450 nm long pass filter for 60 min, and the solar cell was tested by the EIS at 0 min, 10 min, 30 min, and 60 min respectively.

Resistance of the hole conductor was tested by four-point probe (Jandel Four-Point Probe with RM3000 Test Unit) measurement with the devices mentioned before in dark condition. The curves on the devices, which were created by the 100 μm spacer, were set between the second and third probe during the test. Before testing, the devices were illuminated on solar simulator with full light, 380 nm long pass filter and 450 nm long pass filter for 0 min, 10 min, 20 min, 30 min, 40 min and 60 min, respectively.

Appendix C

General advice for *operando* BCDI measurements of battery cathodes at Sector 34-ID-C of the Advanced Photon Source

This section will use lithium-ion batteries as an example for how to prepare and perform BCDI measurements. The majority of measurements were taken at the Argonne National Laboratory (ANL) Advanced Photon Source (APS) using Sector 34-ID-C. In general, we focus the beam to a size of about 1×1 square microns to illuminate a single nanoparticle that remains in the Bragg condition. The detector is positioned more than a meter downstream of the sample to resolve the interference fringes due to a finite-sized the particle, which must be smaller than the X-ray beam. Normally we use a photon energy of around 9 keV and rotate the detector to a 2θ angle of 17° to capture the (003) Bragg reflection. The particles are randomly distributed and randomly oriented throughout the cathode and a scan across the sample area will be performed to find a single isolated particle satisfying the Bragg condition (see Figure 1.5). We will then record rocking curves around the Bragg angle (a rotation in the θ angle) in the range of 0.4° to obtain 3D reciprocal space maps (see Figure 2.7), which later will be reconstructed using a phase retrieval algorithm. We can perform the phasing on a GPU cluster at UCSD almost in real time, which allows for on-the-fly analysis. After a single isolated particle is found and a rocking curve in the pristine state is recorded we will start the first cycle (charging and discharging) of the battery with a charge rate of C/10 (10 hours for a full charge/discharge) and simultaneously record rocking curves while *operando*. We will then repeat a full cycle with the same battery on the same particle. In many battery materials the first and second cycles differ significantly; an effect called activation. By comparing the strain dynamics during different cycles one might elucidate the fundamental processes underlying the activation mechanism.

I made use of four different methods of sample mounting. The most basic is an *ex situ* measurement of cathode powder attached to a layer of Kapton tape. One method involves using a normal coin cell (such as might be found in a watch battery) and poking a hole through the stainless steel casing and covering this aperture with Kapton tape. This is mounted in the sample holder shown in Figure C.5. For the majority of my measurements, I used Argonne's multi-purpose *in situ* X-ray cell (AMPIX) sample holder. This is similar to a battery coin cell but with an amorphous carbon window to allow X-rays to penetrate the rest of the stack easily (shown in Figures C.7, C.8).

C.1 Detectors

C.1.1 Software commands to switch to CCD detector

- Medipix
- ad_off
- ad_setup

- 34idcTIM2
- 512
- 0.055
- 512
- 0.055
- ad_on
- shon 2
- ad_save_on

C.1.2 Software commands to switch to Medipix detector

- ad_off
- ad_setup
- 34idcPRI
- 1340
- 0.025
- 1300
- 0.025
- ad_on
- shon 0
- ad_save_on

C.1.3 CCD

The CCD is typically used with an unfocused X-ray beam, with $\mathbf{H}_{gap}$ and $\mathbf{V}_{gap}$ set to 0.1 (100 μm) and **KB** $\mathbf{H}_{pos} = 572$, **KB** $\mathbf{V}_{pos} = 5716$. The CCD should be 260 mm from the table to the bottom of the kinematic mount. The distance from the back of the CCD to the middle of the sample should be approximately 55 cm..

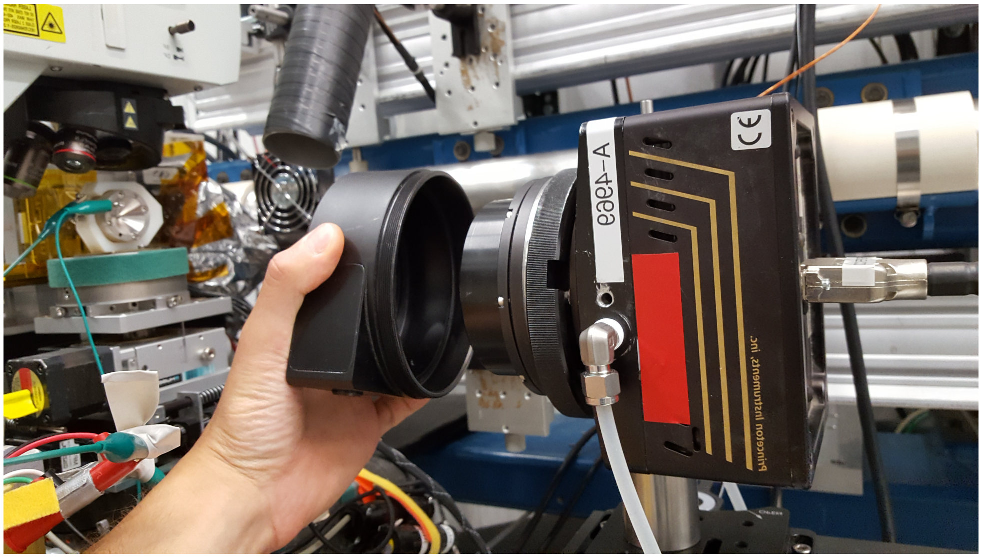

Figure C.1: A photograph of the mounted CCD detector.

It is important to be careful with the Be window of the CCD detector, and to use the cover when working in the vicinity as shown in Figure C.1. The shutter control for the background does not work for macros with ”for” loops, therefore the suggested method is to move the sample out of view of the beam and detector at the end of each loop and record empty beam images as a background.

C.1.4 Medipix

To switch back to the MEDIPIX detector signal integrated over the region of interest (ROI) use the command: plotselect imtot; ad_on.

The detector is made up of four 256×256 pixel panels. The ROI within the 512×512 pixel region can be set by modifying the numbers at the end of the following commands:

- epics_put("34idcTIM2:ROI5:MinX", 0)
- epics_put("34idcTIM2:ROI5:MinY", 0)
- epics_put("34idcTIM2:ROI5:SizeX", 512)
- epics_put("34idcTIM2:ROI5:SizeY", 512)

C.2 Tips for beamline control

- If the ImageJ plugin is not working and showing weird numbers click **focus**.
- If the diode window is not working, close it, go to desktop, click **openvcap** shortcut and then press **Later**.
- To use the visible light microscope go to TV and bring the sample to the focus using z-motor. Then switch to CF and check that for 5× magnification the height is set to approximately 3757.5, and 3847.4 for 20× magnification. Bring your sample to the cross and focal plane. The positional accuracy is about 1 μm.
- Submitting two separate macros within the same line does not work.
- It is good practice to close the shutter when you are not taking measurements.

C.3 Alignment of the sample rotation axis

1. Roughly align Z, then **X**, then θ and **X** again.
2. Decrease θ as low as possible, but enough to see the peak. Align **X**.

3. Increase θ as high as possible, but enough to see the peak. $\delta\theta$ is how much you increased θ.
4. Move **X** to observe the highest intensity. δX is how much you increased **X**.
5. Increase **Y** by $\delta Y = -\delta X / \sin(\delta\theta)$. Increase Z by $\delta Z = \delta Y \cdot \sin(\phi)$.
6. Decrease θ by $\delta\theta/2$ (original position), adjust **X**, then θ.

C.4 Searching for particles

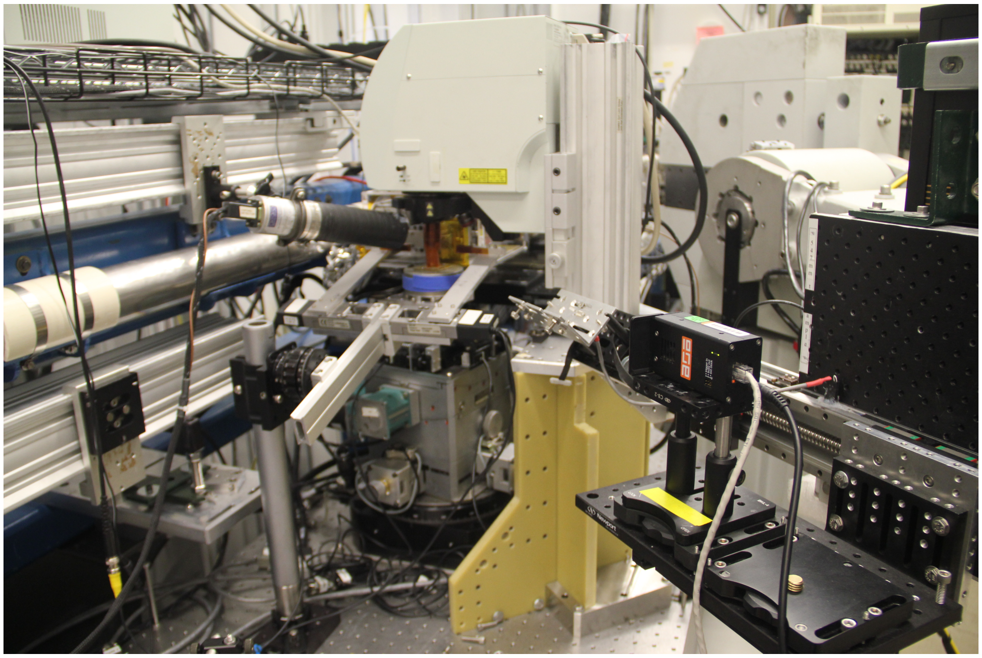

Figure C.2: Detector setup at the APS Sector 34-ID-C.

1. Move detector to 450 mm, open slits, set **X**, **Y**, **labx**, **laby**, **labz**, θ to 0.
2. Find a particle nearby, bring it to the center of rotation.
3. Increase sample-to-detector distance until diffraction intensity fills your region of interest, insert flight tube of appropriate length.

4. Set **X** to 0, save this position as “line1” perform **X** line scan from 0 to 1000 μm.
5. Scroll through images, noting promising particles one by one. Align each particle. For the first particle in each line scan check if it is on the center of rotation.
6. Go to the next particle as soon as you see that the present one cannot work.
7. Starting from 10th particle use abbreviation N_s, N_g, N_f, where N is the number of particle, *a*-super (best of 10), *b*-good(best of 3), *c*-fair.
8. For super particles reduce slits, realign and make a short rocking scan. Record in the logbook the number of maximum counts, how many fringes, and size.
9. Useful to take single shot 5 sec. duplicate image with the name of this particle and minimize this window. Later on it will be much easier to compare particles visually, also you don’t have to estimate and write down intensity level.
10. When you are satisfied with number of particles go through the first ten ones and assign letters to them.

C.5 Estimate BCDI scan parameters

If you have a diffraction pattern of N_{full} number of pixels in size and you need to measure a cube in reciprocal space enfolding this pattern use the following equation: $\theta_{range} = N_{full} \times 0.055/CamDist/\sin(2\theta)$ in radians. Here 0.055 mm is the Medipix pixel size, *CamDist* is in mm.

Similarly, if you want to have same sampling in all the directions number of steps should be equal N_{full}. In practice however it makes sense to use smaller range in order to reduce acquisition time and dose (measurements near the peak position are much more efficient than measurement at large angular derivations). There is also a limit on spherical aberrations (at least when the reconstruction is performed before the coordinate transformation). The maximum angular range can be calculated using the equation $\theta_{max\ range} = \sqrt{0.055 \times n_s/CamDist/\sin(theta)}$.

C.6 *Ex situ* sample mounting

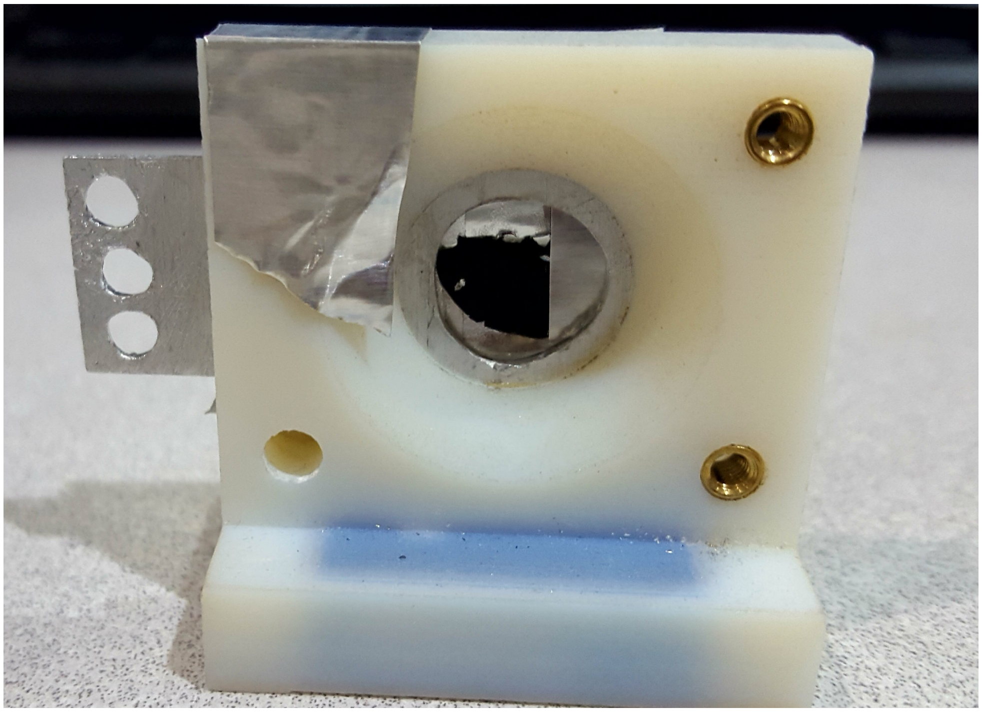

Figure C.3: A prepared *ex situ* sample.

For *ex situ* measurements, cathode powder is epoxied to a flat X-ray transparent surface (such as Kapton tape) that is then vertically mounted in the transmission geometry, as in Figure C.3.

C.7 Coin cells

A 1 mm diameter hole is drilled through the stainless steel casing, and a small piece of Kapton tape is epoxied around the hole. The coin cell is then prepared normally. As Kapton is not airtight nor does it apply any stacking pressure to the cell components, this setup is best prepared only a day or two ahead of time, and stored in a N_2 glovebox until needed (see Figure C.4a).

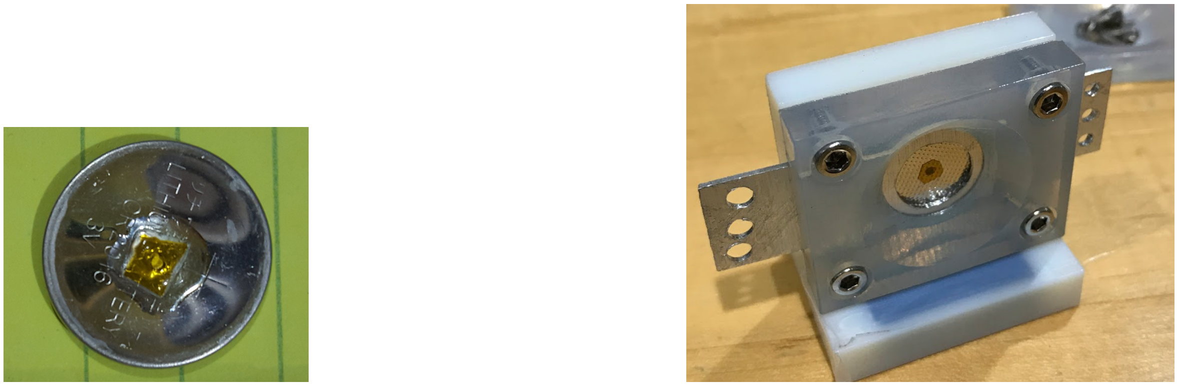

(a) A battery coin cell prepared for *operando* measurements.

(b) Photograph of coin cell holder used for BCDI measurement with mounted lithium ion battery coin cell. See Figure C.5 for a 3D rendering.

Figure C.4: Mounting coin cells at APS Sector 34

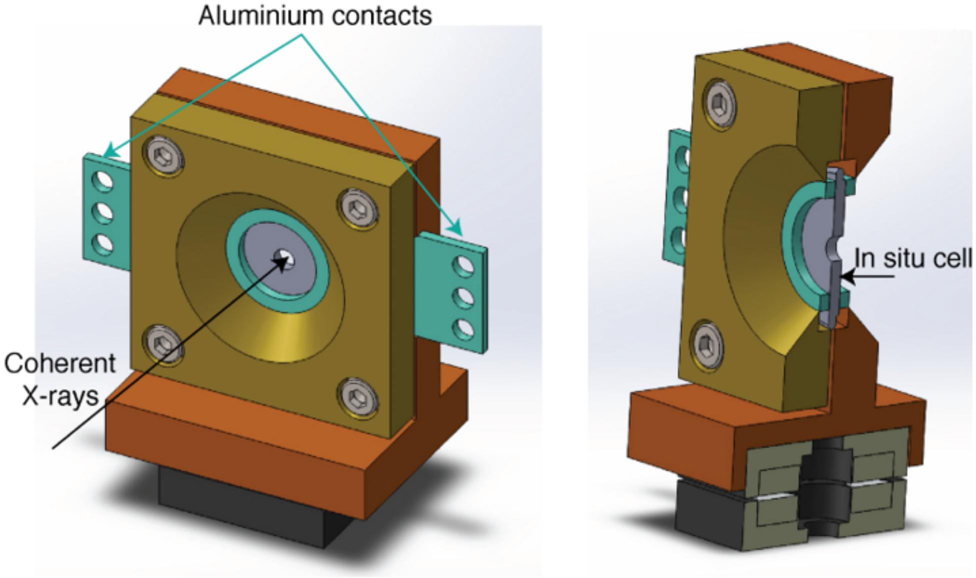

Figure C.5: 3D rendering of the coin cell holder used for BCDI measurement, designed by Evan Maxey. See Figure C.4b for a photograph of a mounted sample.

They often fail but are more convincing for publishing papers, as they are very similar to what will be used in working batteries. They are very easy to short-circuit!

C.7.1 How to mount the coin cell

1. Measure the voltage first.
2. Unscrew the holder, use tape to secure the metal contacts in the plastic parts.
3. Put the bigger part horizontally then put a piece of plastic foil on top to block the metal contact completely and secure it with tape.
4. Put the coin cell facing down on the plastic. Put the second part on top and partially tighten 3 of the screws.
5. Gently slide the plastic foil out holding the coin with your thumb. Insert the remaining screw and tighten it and the others.
6. Check if the voltage is the same. Generally, if you short circuit the coin cell the voltage drops down by about 0.5 V and then slowly recovers within next 15-20 minutes.

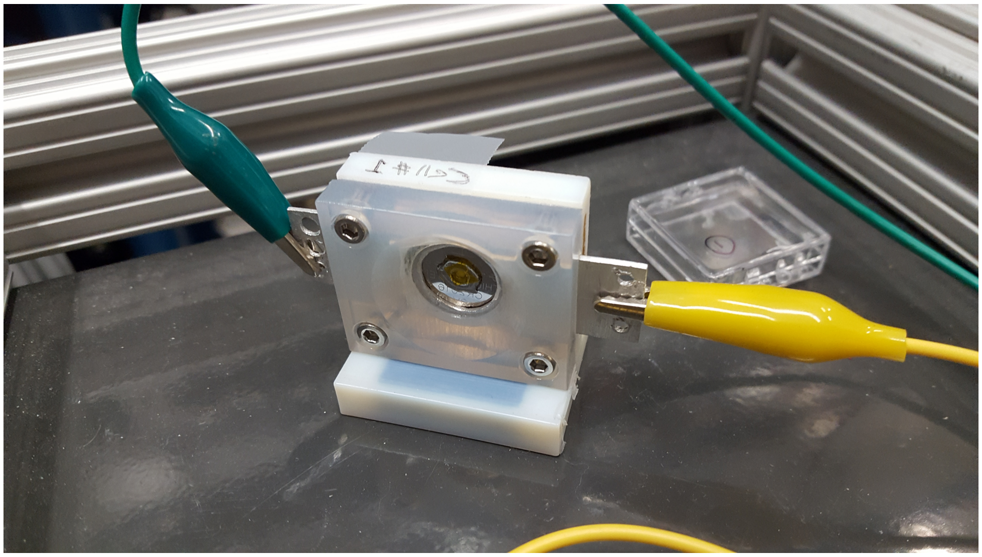

Figure C.6: A coin cell holder connected to leads for cycling.

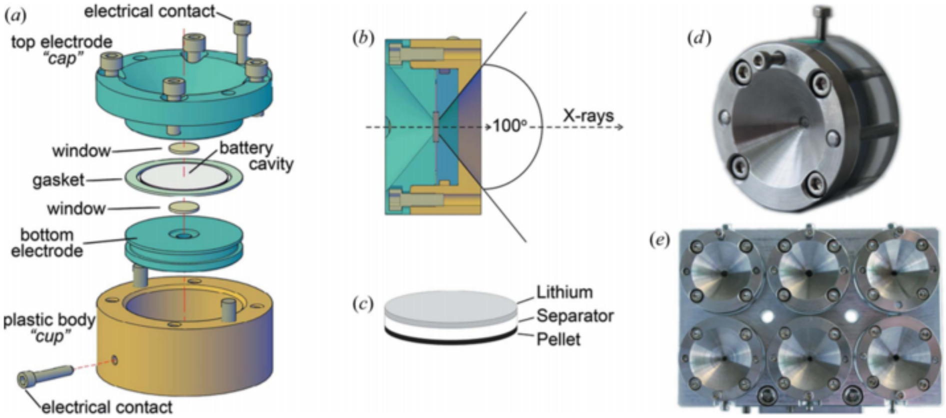

Figure C.7: Diagram of AMPIX cell holder[111]

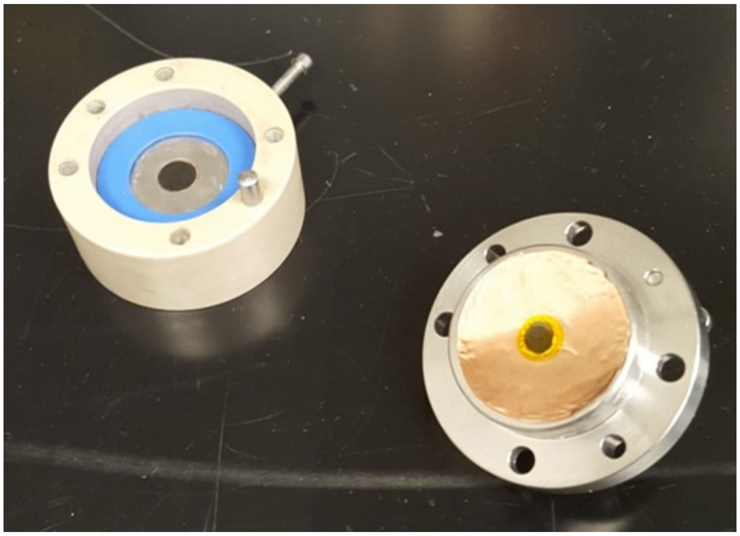

Figure C.8: Photograph of AMPIX cell holder

C.8 AMPIX cells

They normally work better than the coin cells which often leak especially after couple of days.

C.8.1 Preparing AMPIX cells

1. Put all the parts except of the screws into the glovebox.

2. Cut the separation pads of required size. It should fit very well in the cell.
3. Cut a piece of lithium foil of the same size and polish it to remove any possible contamination and make it flat.
4. Weight the cathode and put it inside in the cell, so the active material is facing up
5. Put the separation pads on top of the cathode and add 7-9 drops of electrolyte. It should wet all the pad.
6. Put the lithium on top and close the cell. One of the holes is bigger which leaves you only one possible way to do it.
7. Slightly tighten the screws going one by one going around the circle. Continue until all of them are secured.
8. Write down the cell number, cathode material and weight, type of electrolyte also voltage
9. Calculate required current using equation: $I = (M_T - M_{Al}) \times \eta \times C_s/R$, where M_T is the total electrode mass, M_{Al} is the mass of the aluminum foil, η is the decimal percentage of active material, C_s is the specific capacity, and R is the desired time to fully charge.

C.8.2 Cleaning AMPIX cells

1. Unscrew all the screws, remove the Li foil and put in the vial for used Li.
2. The separation pad and the cathode go into special plastic bag.
3. Write chemical composition and type of the electrolyte on it and leave it on the table.
4. Clean the AMPIX cell parts with isopropanol and some tissue.
5. Put the part to a special tray on the table.

C.8.3 Sample holder for AMPIX cells:

1. Use one of the screws below the cylinder (wrapped by green tape), and take it off.
2. Unscrew two screws to remove the metal plate with the kinematic mount
3. Unscrew axial screw to disassemble the mount, remove the Al cylinder and use shorter screw to attach 3D-printed plastic holder for the AMPIX cell.
4. Mount the metal plate back to the cylinder and put mount the cylinder back on the sample stage.

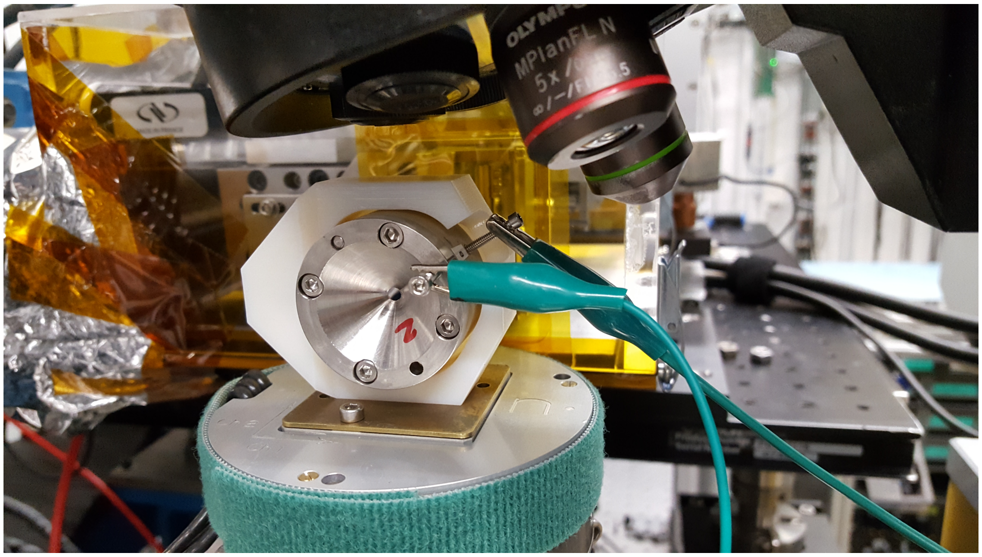

Figure C.9: The mounted AMPIX cell holder with voltage leads connecting to the cycler.

C.9 MACCOR battery cycler

The battery cyclers are reserved from APS Sector 11. Some of them do not support negative voltage, so it is always important to check if you connect the buttery with proper polarity. Positive contact is the red cable. Sometimes you might experience problems running the procedures. In that case go to ”Current control problem” and try to connect the ethernet cable to a different outlet. Rebooting the software also helps. Remember to write down the offset between real time and the MACCOR time, if any. At the end of the beamtime, save data as text files and transfer all the data using a USB stick.

C.10 Useful links

- https://wiki.aps.anl.gov/s34id/index.php/34ID-C_Coherent_x-ray_diffraction_experimental_hutch
- https://wiki-ext.aps.anl.gov/s34idc/index.php/Main_Page

Bibliography

[1] BP, "BP Statistical Review of World Energy 2018," tech. rep., British Petroleum, London, 2018.

[2] W. J. Ripple, C. Wolf, T. M. Newsome, M. Galetti, M. Alamgir, E. Crist, M. I. Mahmoud, W. F. Laurance, and . s. s. f. . c. 15, "World Scientists' Warning to Humanity: A Second Notice," *BioScience*, vol. 67, pp. 1026–1028, 11 2017.

[3] U. Nations, "United nations population division home page." http://www.un.org/en/development/desa/population/.

[4] C. B. Field, *Climate change 2014–Impacts, adaptation and vulnerability: Regional aspects*. Cambridge University Press, 2014.

[5] A. D. Barnosky, N. Matzke, S. Tomiya, G. O. Wogan, B. Swartz, T. B. Quental, C. Marshall, J. L. McGuire, E. L. Lindsey, K. C. Maguire, B. Mersey, and E. A. Ferrer, "Has the earth's sixth mass extinction already arrived?," *Nature*, vol. 471, no. 7336, pp. 51–57, 2011.

[6] B. J. De Vries, D. P. Van Vuuren, and M. M. Hoogwijk, "Renewable energy sources: Their global potential for the first-half of the 21st century at a global level: An integrated approach," *Energy Policy*, vol. 35, no. 4, pp. 2590–2610, 2007.

[7] Y. Luo, S. Gamliel, S. Nijem, S. Aharon, M. Holt, B. Stripe, V. Rose, M. I. Bertoni, L. Etgar, and D. P. Fenning, "Spatially heterogeneous chlorine incorporation in organic–inorganic perovskite solar cells," *Chemistry of Materials*, vol. 28, no. 18, pp. 6536–6543, 2016.

[8] D. Andre, S.-J. Kim, P. Lamp, S. F. Lux, F. Maglia, O. Paschos, and B. Stiaszny, "Future generations of cathode materials: an automotive industry perspective," *Journal of Materials Chemistry A*, vol. 3, no. 13, pp. 6709–6732, 2015.

[9] B. Kumar, J. Kumar, R. Leese, J. P. Fellner, S. J. Rodrigues, and K. M. Abraham, "A Solid-State, Rechargeable, Long Cycle Life Lithium–Air Battery," *Journal of The electrochemical society*, vol. 157, no. 1, p. 50, 2010.

[10] B. Scrosati, J. Hassoun, and Y.-K. Sun, "Lithium-ion batteries. A look into the future," *Energy & Environmental Science*, vol. 4, no. 9, pp. 3287–3295, 2011.

[11] B. L. Ellis, K. T. Lee, and L. F. Nazar, “Positive electrode materials for Li-Ion and Li-batteries,” *Chemistry of Materials*, vol. 22, no. 3, pp. 691–714, 2010.

[12] M. A. Pfeifer, G. J. Williams, I. A. Vartanyants, R. Harder, and I. K. Robinson, “Three-dimensional mapping of a deformation field inside a nanocrystal,” *Nature Letters*, vol. 442, no. 7098, pp. 63–66, 2006.

[13] M. Sathiya, G. Rousse, K. Ramesha, C. P. Laisa, H. Vezin, M. T. Sougrati, M.-l. Doublet, D. Foix, D. Gonbeau, W. Walker, A. S. Prakash, M. B. Hassine, and L. Dupont, “high-capacity layered-oxide electrodes,” *Nature Materials*, vol. 12, no. 9, pp. 827–835, 2013.

[14] M. Sathiya, A. M. Abakumov, D. Foix, G. Rousse, K. Ramesha, M. Saubanère, M. L. Doublet, H. Vezin, C. P. Laisa, A. S. Prakash, D. Gonbeau, G. VanTendeloo, and J.-M. Tarascon, “Origin of voltage decay in high-capacity layered oxide electrodes,” *Nature Materials*, vol. 14, pp. 230–238, Feb 2015.

[15] H. Yu and H. Zhou, “High-Energy Cathode Materials (Li2MnO3–LiMO2) for Lithium-Ion Batteries,” *The Journal of Physical Chemistry Letters*, vol. 4, pp. 1268–1280, April 2013.

[16] S. Hy, H. Liu, M. Zhang, D. Qian, B.-J. J. Hwang, Y. S. Meng, M. Zhang, B.-J. J. Hwang, Y. S. Meng, D. Qian, B.-J. J. Hwang, Y. S. Meng, M. Zhang, B.-J. J. Hwang, Y. S. Meng, D. Qian, B.-J. J. Hwang, and Y. S. Meng, “Performance and Design Considerations For The lithium Excess Layered Oxide Positive Electrode Materials For Lithium Ion Batteries,” *Energy Environ. Sci.*, vol. 2, no. 6, pp. 1931–1954, 2016.

[17] P. Yan, J. Zheng, M. Gu, J. Xiao, J.-G. Zhang, and C.-M. Wang, “Intragranular cracking as a critical barrier for high-voltage usage of layer-structured cathode for lithium-ion batteries,” *Nature Communications*, vol. 8, p. 14101, 2017.

[18] M. D. Radin, S. Hy, M. Sina, C. Fang, H. Liu, J. Vinckeviciute, M. Zhang, M. S. Whittingham, Y. S. Meng, and A. Van der Ven, “Narrowing the gap between theoretical and practical capacities in li-ion layered oxide cathode materials,” *Advanced Energy Materials*, vol. 7, no. 20, p. 1602888, 2017.

[19] C. Genevois, H. Koga, L. Croguennec, M. Ménétrier, C. Delmas, and F. Weill, “Insight into the atomic structure of cycled lithium-rich layered oxide Li1.20Mn0.54Co0.13Ni0.13O2 using haadf stem and electron nanodiffraction,” *The Journal of Physical Chemistry C*, vol. 119, no. 1, pp. 75–83, 2014.

[20] K. Chang, “The grim story of maya blue.” http://www.nytimes.com/2008/02/29/science/29bluew.html?

[21] P. Gómez-Romero and C. Sanchez, *Functional hybrid materials*. John Wiley & Sons, 2006.

[22] C. Reyes-Valerio, *De Bonampak al Templo Mayor: el azul maya en Mesoamérica*. Siglo XXI Editores, 1993.

[23] "Best research-cell efficiency chart." https://www.nrel.gov/pv/cell-efficiency.html. Accessed: 2019-04-30.

[24] M. T. Weller, O. J. Weber, P. F. Henry, A. M. Di Pumpo, and T. C. Hansen, "Complete structure and cation orientation in the perovskite photovoltaic methylammonium lead iodide between 100 and 352 K," *Chemical Communications*, vol. 51, pp. 4180–4183, Feb 2015.

[25] C. Bernal and K. Yang, "First-principles hybrid functional study of the organic–inorganic perovskites CH3NH3SnBr3 and CH3NH3SnI3," *The Journal of Physical Chemistry C*, vol. 118, no. 42, pp. 24383–24388, 2014.

[26] J. M. Frost, K. T. Butler, and A. Walsh, "Molecular ferroelectric contributions to anomalous hysteresis in hybrid perovskite solar cells," *APL Materials*, vol. 2, p. 081506, May 2014.

[27] M. A. García and J. Balenzategui, "Estimation of photovoltaic module yearly temperature and performance based on nominal operation cell temperature calculations," *Renewable Energy*, vol. 29, no. 12, pp. 1997–2010, 2004.

[28] K. Leo, "Perovskite photovoltaics: Signs of Nano Letters," *Nature Nanotechnology*, vol. 10, pp. 574–575, 2015.

[29] A. Dualeh, T. Moehl, N. Tetreault, J. Teuscher, P. Gao, M. K. Nazeeruddin, and M. Grätzel, "Impedance spectroscopic analysis of lead iodide perovskite-sensitized solid-state solar cells," *ACS Nano*, vol. 8, no. 1, pp. 362–373, 2013.

[30] X. Li, M. Tschumi, H. Han, S. S. Babkair, R. A. Alzubaydi, A. A. Ansari, S. S. Habib, M. K. Nazeeruddin, S. M. Zakeeruddin, and M. Grätzel, "Outdoor Performance and Nano Letters under Elevated Temperatures and Long-Term Light Soaking of Triple-Layer Mesoporous Perovskite Photovoltaics," *Energy Technology*, vol. 3, no. 6, pp. 551–555, 2015.

[31] Editorial, "Due credit," *Nature*, vol. 496, no. 86, p. 270, 2013.

[32] A. Rose, *Vision: Human and Electronic*. IBM Research Symposia Series, Plenum Press, 1973.

[33] K. Shin and J. Hammond, *Fundamentals of signal processing for sound and vibration engineers*. John Wiley & Sons, 2008.

[34] A. R. Thompson, J. M. Moran, and G. W. Swenson, *Van Cittert–Zernike Theorem, Spatial Coherence, and Scattering*, pp. 767–786. Cham: Springer International Publishing, 2017.

[35] S. Henderson and A. P. S. U. Project, "Status of the Aps Upgrade Project * Aps-U Conceptual Design," *Proceedings of IPAC*, vol. 2, no. 2, pp. 1791–1793, 2015.

[36] P. Thibault, *Algorithmic Methods in Diffraction Microscopy*. Phd, Cornell University, 2007.

[37] F. P. Thibault, Pierre Martin Dierolf, AndreasMenzel, Oliver Bunk, Christian David, "High-Resolution Scanning X-ray Diffraction Microscopy," *Science*, vol. 379, no. July, pp. 379–383, 2008.

[38] J. R. Fienup, "Reconstruction of an object from the modulus of its Fourier transform," *Optics Letters*, vol. 3, p. 27, July 1978.

[39] V. Elser, "Phase retrieval by iterated projections," *Journal of the Optical Society of America A*, vol. 20, no. 1, pp. 40–55, 2002.

[40] H. H. Bauschke, P. L. Combettes, and D. R. Luke, "Phase retrieval, error reduction algorithm, and Fienup variants: a view from convex optimization," *Journal of the Optical Society of America A*, vol. 19, p. 1334, July 2002.

[41] K. Van Overveld and B. Wyvill, "Shrinkwrap: An efficient adaptive algorithm for triangulating an iso-surface," *The Visual Computer*, vol. 20, no. 6, pp. 362–379, 2004.

[42] H. N. Chapman, A. Barty, S. Marchesini, A. Noy, S. P. Hau-Riege, C. Cui, M. R. Howells, R. Rosen, H. He, J. C. H. Spence, U. Weierstall, T. Beetz, C. Jacobsen, and D. Shapiro, "High-resolution ab initio three-dimensional X-ray diffraction microscopy," *Journal of the Optical Society of America A*, vol. 23, no. 5, p. 1179, 2006.

[43] J. Lee, A. Urban, X. Li, D. Su, G. Hautier, and G. Ceder, "Unlocking the potential of cation-disordered oxides for rechargeable lithium batteries.," *Science*, vol. 343, pp. 519–22, Feb 2014.

[44] M. Sathiya, G. Rousse, K. Ramesha, C. P. Laisa, H. Vezin, M. T. Sougrati, M.-L. Doublet, D. Foix, D. Gonbeau, W. Walker, A. S. Prakash, M. Ben Hassine, L. Dupont, and J.-M. Tarascon, "Reversible anionic redox chemistry in high-capacity layered-oxide electrodes.," *Nature Materials*, vol. 12, no. 9, pp. 827–35, 2013.

[45] K. Luo, M. R. Roberts, R. Hao, N. Guerrini, D. M. Pickup, Y.-S. Liu, K. Edstrom, J. Guo, A. V. Chadwick, L. C. Duda, and P. G. Bruce, "Charge-compensation in 3d-transition-metal-oxide intercalation cathodes through the generation of localized electron holes on oxygen," *Nature Chemistry*, vol. 8, 2016.

[46] D.-H. Seo, J. Lee, A. Urban, R. Malik, S. Kang, and G. Ceder, "The structural and chemical origin of the oxygen redox activity in layered and cation-disordered Li-excess cathode materials," *Nature Chemistry*, vol. 8, no. 7, pp. 692–697, 2016.

[47] W. Wei, L. Chen, A. Pan, and D. G. Ivey, "Roles of surface structure and chemistry on electrochemical processes in lithium-rich layered oxide cathodes," *Nano Energy*, vol. 30, no. 9, pp. 580–602, 2016.

[48] Z. Liu, L. Zou, J. Zheng, Y. Yang, H. Jia, C. Wang, G. Wang, W. Zhao, and J.-G. Zhang, "Solid–Liquid Interfacial Reaction Trigged Propagation of Phase Transition from Surface

into Bulk Lattice of Ni-Rich Layered Cathode," *Chemistry of Materials*, vol. 30, no. 20, pp. 7016–7026, 2018.

[49] B. Xu, C. R. Fell, M. Chi, and Y. S. Meng, "Identifying surface structural changes in layered Li-excess nickel manganese oxides in high voltage lithium ion batteries: A joint experimental and theoretical study," *Energy & Environmental Science*, vol. 4, p. 2223, June 2011.

[50] A. Boulineau, L. Simonin, J. F. Colin, C. Bourbon, and S. Patoux, "First evidence of manganese-nickel segregation and densification upon cycling in Li-rich layered oxides for lithium batteries," *Nano Letters*, vol. 13, no. 8, pp. 3857–3863, 2013.

[51] F. Lin, I. M. Markus, D. Nordlund, T. C. Weng, M. D. Asta, H. L. Xin, and M. M. Doeff, "Surface reconstruction and chemical evolution of stoichiometric layered cathode materials for lithium-ion batteries," *Nature communications*, vol. 5, p. 3529, 2014.

[52] H. Yu, Y.-G. G. So, A. Kuwabara, E. Tochigi, N. Shibata, T. Kudo, H. Zhou, and Y. Ikuhara, "Crystalline Grain Interior Configuration Affects Lithium Migration Kinetics in Li-Rich Layered Oxide," *Nano Letters*, vol. 16, no. 5, pp. 2907–2915, 2016.

[53] A. Singer, M. Zhang, S. Hy, D. Cela, C. Fang, T. A. Wynn, B. Qiu, Y. Xia, Z. Liu, A. Ulvestad, N. Hua, J. Wingert, H. Liu, M. Sprung, A. V. Zozulya, E. Maxey, R. Harder, Y. S. Meng, O. G. Shpyrko, M. Zhang, D. Cela, C. Fang, B. Qiu, Y. Xia, Z. Liu, S. Hy, D. Cela, C. Fang, T. A. Wynn, B. Qiu, Y. Xia, Z. Liu, A. Ulvestad, N. Hua, J. Wingert, H. Liu, M. Sprung, A. V. Zozulya, E. Maxey, R. Harder, Y. S. Meng, and O. G. Shpyrko, "Nucleation of dislocations and their dynamics in layered oxide cathode materials during battery charging," *Nature Energy*, vol. 3, no. 8, pp. 1–7, 2018.

[54] M. Gu, I. Belharouak, A. Genc, Z. Wang, D. Wang, K. Amine, F. Gao, G. Zhou, S. Thevuthasan, D. R. Baer, J. G. Zhang, N. D. Browning, J. Liu, and C. Wang, "Conflicting roles of nickel in controlling cathode performance in lithium ion batteries," *Nano letters*, vol. 12, no. 10, pp. 5186–5191, 2012.

[55] A. Genc, L. Kovarik, M. Gu, H. Cheng, P. Plachinda, L. Pullan, B. Freitag, and C. Wang, "XEDS STEM tomography for 3D chemical characterization of nanoscale particles," *Ultramicroscopy*, vol. 131, pp. 24–32, 2013.

[56] M. Gu, A. Genc, I. Belharouak, D. Wang, K. Amine, S. Thevuthasan, D. R. Baer, J. G. Zhang, N. D. Browning, J. Liu, and C. Wang, "Nanoscale phase separation, cation ordering, and surface chemistry in pristine Li1.2Ni0.2Mn0.6O2 for Li-ion batteries," *Chemistry of Materials*, vol. 25, no. 11, pp. 2319–2326, 2013.

[57] J. Zheng, M. Gu, A. Genc, J. Xiao, P. Xu, X. Chen, Z. Zhu, W. Zhao, L. Pullan, C. Wang, and J. G. Zhang, "Mitigating voltage fade in cathode materials by improving the atomic level uniformity of elemental distribution," *Nano Letters*, vol. 14, no. 5, pp. 2628–2635, 2014.

[58] A. Devaraj, M. Gu, R. Colby, P. Yan, C. M. Wang, J. M. Zheng, J. Xiao, A. Genc, J. G. Zhang, I. Belharouak, D. Wang, K. Amine, and S. Thevuthasan, “Visualizing nanoscale 3D compositional fluctuation of lithium in advanced lithium-ion battery cathodes,” *Nature Communications*, vol. 6, 2015.

[59] P. Emma, R. Akre, J. Arthur, R. Bionta, C. Bostedt, J. Bozek, a. Brachmann, P. Bucksbaum, R. Coffee, F.-J. Decker, Y. Ding, D. Dowell, S. Edstrom, a. Fisher, J. Frisch, S. Gilevich, J. Hastings, G. Hays, P. Hering, Z. Huang, R. Iverson, H. Loos, M. Messerschmidt, a. Miahnahri, S. Moeller, H.-D. Nuhn, G. Pile, D. Ratner, J. Rzepiela, D. Schultz, T. Smith, P. Stefan, H. Tompkins, J. Turner, J. Welch, W. White, J. Wu, G. Yocky, and J. Galayda, “First lasing and operation of an ångstrom-wavelength free-electron laser,” *Nature Photonics*, vol. 4, no. 9, pp. 641–647, 2010.

[60] A. K. Shukla, Q. M. Ramasse, C. Ophus, H. Duncan, F. Hage, G. Chen, F. Hage, H. Duncan, A. K. Shukla, Q. M. Ramasse, C. Ophus, H. Duncan, F. Hage, and G. Chen, “Unravelling structural ambiguities in lithium- and manganese-rich transition metal oxides,” *Nature Communications*, vol. 6, no. 5, pp. 1–9, 2015.

[61] H. Liu, Y. Chen, S. Hy, K. An, S. Venkatachalam, D. Qian, M. Zhang, and Y. S. Meng, “Operando Lithium Dynamics in the Li-Rich Layered Oxide Cathode Material via Neutron Diffraction,” *Advanced Energy Materials*, p. 1502143, Feb 2016.

[62] I. Robinson and R. Harder, “Coherent X-ray diffraction imaging of strain at the nanoscale.,” *Nature Materials*, vol. 8, no. 4, pp. 291–298, 2009.

[63] W. Cha, N. C. Jeong, S. Song, H.-j. Park, T. C. Thanh Pham, R. Harder, B. Lim, G. Xiong, D. Ahn, I. McNulty, J. Kim, K. B. Yoon, I. K. Robinson, and H. Kim, “Core-shell strain structure of zeolite microcrystals.,” *Nature Materials*, vol. 12, no. 8, pp. 729–34, 2013.

[64] A. Ulvestad, A. Singer, J. N. Clark, H. M. Cho, J. W. Kim, R. Harder, J. Maser, Y. S. Meng, and O. G. Shpyrko, “Topological defect dynamics in operando battery nanoparticles,” *Science*, vol. 348, pp. 1344–1347, June 2015.

[65] A. P. Ulvestad, A. Singer, H.-M. M. Cho, J. N. Clark, R. Harder, J. Maser, Y. S. Meng, and O. G. Shpyrko, “Single particle nanomechanics in operando batteries via lensless strain mapping,” *Nano letters*, vol. 14, pp. 5123–5127, Sep 2014.

[66] A. Singer, A. Ulvestad, H.-m. Cho, J. W. Kim, J. Maser, R. Harder, Y. S. Meng, and O. G. Shpyrko, “Nonequilibrium Structural Dynamics of Nanoparticles in LiNi1/2Mn3/2O4Cathode under Operando Conditions,” *Nano letters*, vol. 14, pp. 5295–5300, 2014.

[67] D. McMorrow and J. Als-Nielsen, *Elements of modern X-ray physics*. Hoboken, NJ: Wiley, 2nd ed., 2011.

[68] C. C. Chen, J. Miao, C. W. Wang, and T. K. Lee, "Application of optimization technique to noncrystalline X-ray diffraction microscopy: Guided hybrid input-output method," *Physical Review B*, vol. 76, no. 6, pp. 1–5, 2007.

[69] R. C. Buck, *Advanced Calculus*. Long Grove: Waveland Press, 3 ed., 2003.

[70] K. Lai, M. Nakamura, W. Kundhikanjana, M. Kawasaki, Y. Tokura, M. A. Kelly, and Z.-X. Shen, "Mesoscopic percolating resistance network in a strained manganite thin film," *Science*, vol. 329, no. 5988, pp. 190–193, 2010.

[71] A. S. McLeod, E. Van Heumen, J. G. Ramirez, S. Wang, T. Saerbeck, S. Guenon, M. Goldflam, L. Anderegg, P. Kelly, A. Mueller, M. K. Liu, I. K. Schuller, and D. N. Basov, "Nanotextured phase coexistence in the correlated insulator v 2 O 3 - supplement," *Nature Physics*, vol. 13, no. 1, pp. 80–86, 2017.

[72] H. S. Jung and N.-G. Park, "Solar Cells: Perovskite Solar Cells: From Materials to Devices," *Small*, vol. 11, p. 2, Feb 2015.

[73] B. Delaunay, "Sur la sphère vide. A la memoire de Georges Voronoi," *Otdelenie Matematicheskih i Estestvennyh Nauk*, vol. 7, no. 6, pp. 793–800,, 1934.

[74] H. Hahn, R. Chen, S. Ren, V. Shapovalov, O. Dolotko, D. Wang, M. Fichtner, A. A. Guda, and E. Maawad, " Improved Voltage and Cycling for Li+ Intercalation in High-Capacity Disordered Oxyfluoride Cathodes ," *Advanced Science*, vol. 2, no. 10, p. 1500128, 2015.

[75] Y. Lyu, N. Zhao, E. Hu, R. Xiao, X. Yu, L. Gu, X. Q. Yang, and H. Li, "Probing Reversible Multielectron Transfer and Structure Evolution of Li1.2Cr0.4Mn0.4O2 Cathode Material for Li-Ion Batteries in a Voltage Range of 1.0-4.8 V," *Chemistry of Materials*, vol. 27, no. 15, pp. 5238–5252, 2015.

[76] L. Ma, L. Mao, X. Zhao, J. Lu, F. Zhang, P. Ding, L. Chen, and F. Lian, "Improving the Structural Stability of Li-Rich Layered Cathode Materials by Constructing an Antisite Defect Nanolayer through Polyanion Doping," *ChemElectroChem*, vol. 4, no. 12, pp. 3068–3074, 2017.

[77] H. Dixit, W. Zhou, J. C. Idrobo, J. Nanda, and V. R. Cooper, "Facet-dependent disorder in pristine high-voltage lithium-manganese-rich cathode material," *ACS Nano*, vol. 8, no. 12, pp. 12710–12716, 2014.

[78] H. Zhang, B. M. May, J. Serrano-Sevillano, M. Casas-Cabanas, J. Cabana, C. Wang, and G. Zhou, "Facet-Dependent Rock-Salt Reconstruction on the Surface of Layered Oxide Cathodes," *Chemistry of Materials*, vol. 30, no. 3, pp. 692–699, 2018.

[79] P. Yan, J. Zheng, J. Zheng, Z. Wang, G. Teng, S. Kuppan, J. Xiao, G. Chen, F. Pan, J. G. Zhang, and C. M. Wang, "Ni and Co Segregations on Selective Surface Facets and Rational Design of Layered Lithium Transition-Metal Oxide Cathodes," *Advanced Energy Materials*, vol. 6, no. 9, pp. 26–28, 2016.

[80] K. Park, D. Yeon, J. H. Kim, J. H. Park, S. Doo, and B. Choi, “Spinel-embedded lithium-rich oxide composites for Li-ion batteries,” *Journal of Power Sources*, vol. 360, pp. 453–459, 2017.

[81] B. Xiao and X. Sun, “Surface and Subsurface Reactions of Lithium Transition Metal Oxide Cathode Materials: An Overview of the Fundamental Origins and Remedying Approaches,” *Advanced Energy Materials*, vol. 8, no. 29, pp. 1–27, 2018.

[82] D. Qian, B. Xu, M. Chi, and Y. S. Meng, “Uncovering the roles of oxygen vacancies in cation migration in lithium excess layered oxides,” *Physical Chemistry Chemical Physics*, vol. 16, pp. 14665–14668, Oct 2014.

[83] T. Hastie, R. Tibshirani, and J. Friedman, *The Elements of Statistical Learning Data Mining, Inference, and Prediction (12th printing)*. Springer, 2009.

[84] F. Pfeiffer, T. Weitkamp, O. Bunk, and C. David, “Phase retrieval and differential phase-contrast imaging with low-brilliance X-ray sources,” *Nature Physics*, vol. 2, no. 4, pp. 258–261, 2006.

[85] H. Liang and L. Mahadevan, “The shape of a long leaf,” *Proceedings of the National Academy of Sciences*, vol. 106, no. 52, pp. 22049–22054, 2009.

[86] J. W. Hutchinson, M. D. Thouless, and E. G. Liniger, “Growth and configurational Nano Letters of circular, buckling-driven film delaminations,” *Acta Metallurgica Et Materialia*, vol. 40, no. 2, pp. 295–308, 1992.

[87] K. Li, S. P. Yan, Y. Ni, H. Y. Liang, and L. H. He, “Controllable buckling of an elastic disc with actuation strain,” *Europhysics Letters*, vol. 92, no. 1, 2010.

[88] B. Audoly and A. Boudaoud, “Self-Similar Structures near Boundaries in Strained Systems,” *Physical Review Letters*, vol. 91, no. 8, pp. 3–6, 2003.

[89] E. Cerda, K. Ravi-Chandar, and L. Mahadevan, “Thin films: Wrinkling of an elastic sheet under tension,” *Nature*, vol. 419, no. 6907, pp. 579–580, 2002.

[90] A. Davtyan, T. Krause, D. Kriegner, A. Al-Hassan, D. Bahrami, S. M. Mostafavi Kashani, R. B. Lewis, H. Küpers, A. Tahraoui, L. Geelhaar, M. Hanke, S. J. Leake, O. Loffeld, and U. Pietsch, “Threefold rotational symmetry in hexagonally shaped core-shell (In,Ga)As/GaAs nanowires revealed by coherent X-ray diffraction imaging,” *Journal of Applied Crystallography*, vol. 50, no. 3, pp. 673–680, 2017.

[91] D. C. Ghiglia and M. D. Pritt, *Two-Dimensional Phase Unwrapping: Theory, Algorithms and Software*. New York: Wiley-Interscience, 1998.

[92] J. N. Clark, L. Beitra, G. Xiong, D. M. Fritz, H. T. Lemke, D. Zhu, M. Chollet, G. J. Williams, M. M. Messerschmidt, B. Abbey, R. J. Harder, A. M. Korsunsky, J. S. Wark, D. A. Reis, and I. K. Robinson, “Imaging transient melting of a nanocrystal using an X-ray

laser.," *Proceedings of the National Academy of Sciences of the United States of America*, vol. 112, no. 24, pp. 7444–7448, 2015.

[93] B. Kang and G. Ceder, "Battery materials for ultrafast charging and discharging.," *Nature*, vol. 458, no. 7235, pp. 190–193, 2009.

[94] S. K. Martha, O. Haik, E. Zinigrad, I. Exnar, T. Drezen, J. H. Miners, and D. Aurbach, "On the Thermal Nano Letters of Olivine Cathode Materials for Lithium-Ion Batteries," *Journal of The electrochemical society*, vol. 158, no. 10, p. A1115, 2011.

[95] M. M. Thackeray, W. I. F. David, P. G. Bruce, and J. B. Goodenough, "Lithium insertion into manganese spinels," *Materials Research Bulletin*, vol. 18, no. 4, pp. 461–472, 1983.

[96] A. K. Padhi, K. S. Nanjundaswamy, and J. B. Goodenough, "Phospho-olivines as Positive-Electrode Materials for Rechargeable Lithium Batteries," *Journal of The Electrochemical Society*, vol. 144, no. 4, pp. 1–7, 1997.

[97] P. Barpanda, M. Ati, B. C. Melot, G. Rousse, J.-N. Chotard, M.-L. Doublet, M. T. Sougrati, S. a. Corr, J.-C. Jumas, and J.-M. Tarascon, "A 3.90 V iron-based fluorosulphate material for lithium-ion batteries crystallizing in the triplite structure," *Nature Materials*, vol. 10, no. 10, pp. 772–779, 2011.

[98] Y. Itou and Y. Ukyo, "Performance of LiNiCoO2 materials for advanced lithium-ion batteries," *Journal of Power Sources*, vol. 146, no. 1-2, pp. 39–44, 2005.

[99] R. Kostecki and F. McLarnon, "Local-probe studies of degradation of composite LiNi0.8Co0.15Al0.05O2 cathodes in high-power lithium-ion cells," *Electrochemical and Solid-State Letters*, vol. 7, no. 10, pp. 380–383, 2004.

[100] C. H. Chen, J. Liu, M. E. Stoll, G. Henriksen, D. R. Vissers, and K. Amine, "Aluminum-doped lithium nickel cobalt oxide electrodes for high-power lithium-ion batteries," *Journal of Power Sources*, vol. 128, no. 2, pp. 278–285, 2004.

[101] Tesla, "Tesla — electric cars, solar panels & clean energy storage." https://www.tesla.com/. Accessed: 2016-06-20.

[102] S. Watanabe, M. Kinoshita, T. Hosokawa, and K. Morigaki, "Capacity fading of LiAlyNi1-x-y CoxO2 cathode for lithium-ion batteries during accelerated calendar and cycle life tests (effect of depth of discharge in charge-discharge cycling on the suppression of the micro-crack generation of LiAlyNi1-x-y CoxO2 parti," *Journal of Power Sources*, vol. 258, pp. 210–217, 2014.

[103] S. Watanabe, T. Hosokawa, K. Morigaki, M. Kinoshita, and K. Nakura, "Prevention of the micro cracks generation in LiNiCoAlO2 cathode by the restriction of DOD," *ECS Transactions*, vol. 41, no. 41, pp. 65–74, 2012.

[104] A. Ulvestad, H.-m. M. Cho, R. Harder, J. W. Kim, S. H. Dietze, E. Fohtung, Y. S. Meng, O. G. Shpyrko, A. Singer, A. Ulvestad, H.-m. M. Cho, J. W. Kim, J. Maser, R. Harder, Y. S. Meng, and O. G. Shpyrko, "Nanoscale strain mapping in battery nanostructures," *Nano Letters*, vol. 104, no. 7, pp. 5295–5300, 2014.

[105] I. Robinson and I. R. Obinson, "Nanoparticle Structure by Coherent X-ray Diffraction," *Journal of the Physical Society of Japan*, vol. 82, pp. 1–7, 2013.

[106] B. Abbey, "From grain boundaries to single defects: A review of coherent methods for materials imaging in the X-ray sciences," *JOM*, vol. 65, no. 9, pp. 1183–1201, 2013.

[107] M. Nye, J.F. and Berry, "Dislocations in Wave Trains," *Proceedings of the Royal Society A*, vol. 336, pp. 165–190, 1974.

[108] M. Guilmard, C. Pouillerie, L. Croguennec, and C. Delmas, "Structural and electrochemical properties of LiNi0.70Co0.15Al0.15O2," *Solid State Ionics*, vol. 160, no. 1-2, pp. 39–50, 2003.

[109] X. Zhao, F. Zhou, and J. R. Dahn, "Phases formed in Al-doped Ni1/3Mn1/3Co1/3(OH)2 prepared by coprecipitation: Formation of layered double hydroxide," *Journal of The electrochemical society*, vol. 155, no. 9, pp. A642–A647, 2008.

[110] R. Robert, C. Bunzli, E. J. Berg, and P. Novak, "Activation Mechanism of LiNi0.80Co0.15Al0.05O2: Surface and bulk operando electrochemical, differential electrochemical mass spectrometry, and X-ray diffraction analyses," *Chemistry of Materials*, vol. 27, no. 2, pp. 526–536, 2015.

[111] O. J. Borkiewicz, B. Shyam, K. M. Wiaderek, C. Kurtz, P. J. Chupas, and K. W. Chapman, "The ampix electrochemical cell: a versatile apparatus for in situ x-ray scattering and spectroscopic measurements," *Journal of Applied Crystallography*, vol. 45, pp. 1261–1269, 2012.

[112] D. Hull and D. Bacon, *Introduction to Dislocations*. Elsevier, 2011.

[113] J. Weertman, "Helical dislocations," *Physical Review*, vol. 107, no. 5, pp. 1259–1261, 1957.

[114] M. Kuzmina, M. Herbig, D. Ponge, S. Sandlobes, S. Sandlobes, and D. Raabe, "Linear complexions: Confined chemical and structural states at dislocations," *Science*, vol. 349, no. 6252, pp. 1080–1083, 2015.

[115] Y. Qi, L. G. Hector Jr., C. James, K. J. Kim, L. G. Hector, C. James, K. J. Kim, L. G. Hector Jr., C. James, K. J. Kim, L. G. Hector, C. James, K. J. Kim, L. G. Hector Jr., C. James, and K. J. Kim, "Lithium Concentration Dependent Elastic Properties of Battery Electrode Materials from First Principles Calculations.," *Journal of The electrochemical society*, vol. 161, no. 11, pp. F3010–F3018, 2014.

[116] G. K. Williamson and W. H. Hall, “X-ray Line Broadening from Filed Aluminium and Wolfram,” *Acta Metallurgica*, vol. 1, no. 1, pp. 22–31, 1953.

[117] K. Hoang and M. Johannes, “Defect Physics and Chemistry in Layered Mixed Transition Metal Oxide Cathode Materials: (Ni,Co,Mn) vs (Ni,Co,Al),” *Chemistry of Materials*, vol. 28, no. 5, pp. 1325–1334, 2016.

[118] T. Ohzuku, A. Ueda, and M. Nagayama, “Electrochemistry and Structural Chemistry of LiNiO2 (R3m) for 4 Volt Secondary Lithium Cells,” *Journal of The electrochemical society*, vol. 140, no. 7, p. 1862, 1993.

[119] J. B. Bates, N. J. Dudney, B. Neudecker, A. Ueda, and C. D. Evans, “Thin-film lithium and lithium-ion batteries,” *Solid State Ionics*, vol. 135, no. 1-4, pp. 33–45, 2000.

[120] B. H. Toby, R. B. V. Dreele, and R. B. Von Dreele, “GSAS-II: The genesis of a modern open-source all purpose crystallography software package,” *Journal of Applied Crystallography*, vol. 46, no. 2, pp. 544–549, 2013.

[121] P. Thompson, D. E. Cox, and J. B. Hastings, “Rietveld Refinement of Debye-Scherrer Synchrotron X-ray Data from Al2O3,” *Journal of Applied Crystallography*, vol. 20, no. 2, pp. 79–83, 1987.

[122] X. Ning, I. W. Selesnick, and L. Duval, “Chromatogram baseline estimation and denoising using sparsity (BEADS),” *Chemometrics and Intelligent Laboratory Systems*, vol. 139, pp. 156–167, 2014.

[123] H. Zheng, J. Li, X. Song, G. Liu, and V. S. Battaglia, “A comprehensive understanding of electrode thickness effects on the electrochemical performances of li-ion battery cathodes,” *Electrochimica Acta*, vol. 71, pp. 258–265, 2012.

[124] J. Sander, R. M. Erb, L. Li, A. Gurijala, and Y.-M. Chiang, “High-performance battery electrodes via magnetic templating,” *Nature Energy*, vol. 1, no. 8, p. 16099, 2016.

[125] B.-S. Lee, Z. Wu, V. Petrova, X. Xing, H.-D. Lim, H. Liu, and P. Liu, “Analysis of rate-limiting factors in thick electrodes for electric vehicle applications,” *Journal of The electrochemical society*, vol. 165, no. 3, pp. 525–533, 2018.

[126] Z. Xiao, Y. Yuan, Y. Shao, Q. Wang, Q. Dong, C. Bi, P. Sharma, A. Gruverman, and J. Huang, “Giant switchable photovoltaic effect in organometal trihalide perovskite devices,” *Nature Materials*, vol. 14, no. 2, pp. 193–198, 2015.

[127] C. Eames, J. M. Frost, P. R. Barnes, B. C. O’regan, A. Walsh, and M. S. Islam, “Ionic transport in hybrid lead iodide perovskite solar cells,” *Nature Communications*, vol. 6, 2015.

[128] Y. Rakita, S. R. Cohen, N. K. Kedem, G. Hodes, and D. Cahen, “Mechanical properties of APbX3 (A = Cs or CH3NH3 ; X = I or Br) perovskite single crystals,” *MRS Communications*, vol. 5, no. 4, pp. 623–629, 2019.

[129] H. J. Snaith, A. Abate, J. M. Ball, G. E. Eperon, T. Leijtens, N. K. Noel, S. D. Stranks, J. T.-W. Wang, K. Wojciechowski, and W. Zhang, "Anomalous hysteresis in perovskite solar cells," *The Journal of Physical Chemistry Letters*, vol. 5, no. 9, pp. 1511–1515, 2014.

[130] D. P. Fenning, J. Hofstetter, M. I. Bertoni, S. Hudelson, M. Rinio, J. F. Lelievre, B. Lai, C. Del Caizo, and T. Buonassisi, "Iron distribution in silicon after solar cell processing: Synchrotron analysis and predictive modeling," *Applied Physics Letters*, vol. 98, no. 16, pp. 0–3, 2011.

[131] M. Stuckelberger, B. West, S. Husein, H. Guthrey, M. Al-Jassim, R. Chakraborty, T. Buonassisi, J. M. Maser, B. Lai, B. Stripe, V. Rose, and M. Bertoni, "Latest developments in the X-ray based characterization of thin-film solar cells," *2015 IEEE 42nd Photovoltaic Specialist Conference, PVSC 2015*, pp. 1–6, 2015.

[132] M. P. Nikiforov, B. Lai, W. Chen, S. Chen, R. D. Schaller, J. Strzalka, J. Maser, and S. B. Darling, "Detection and role of trace impurities in high-performance organic solar cells," *Energy & Environmental Science*, vol. 6, no. 5, p. 1513, 2013.

[133] V. L. Pool, A. Gold-Parker, M. D. McGehee, and M. F. Toney, "Chlorine in PbCl2-Derived Hybrid-Perovskite Solar Absorbers," *Chemistry of Materials*, vol. 27, no. 21, pp. 7240–7243, 2015.

[134] H. Choi, J. Jeong, H. B. Kim, S. Kim, B. Walker, G. H. Kim, and J. Y. Kim, "Cesium-doped methylammonium lead iodide perovskite light absorber for hybrid solar cells," *Nano Energy*, vol. 7, pp. 80–85, 2014.

[135] R. E. Beal, D. J. Slotcavage, T. Leijtens, A. R. Bowring, R. A. Belisle, W. H. Nguyen, G. F. Burkhard, E. T. Hoke, and M. D. McGehee, "Cesium lead halide perovskites with improved Nano Letters for tandem solar cells," *Journal of Physical Chemistry Letters*, pp. 746–751, Feb 2016.

[136] Z. Li, M. Yang, J. S. Park, S. H. Wei, J. J. Berry, and K. Zhu, "Stabilizing Perovskite Structures by Tuning Tolerance Factor: Formation of Formamidinium and Cesium Lead Iodide Solid-State Alloys," *Chemistry of Materials*, vol. 28, no. 1, pp. 284–292, 2016.

[137] M. Lorenzon, L. Sortino, Q. A. Akkerman, S. Accornero, J. Pedrini, M. Prato, V. Pinchetti, F. Meinardi, L. Manna, and S. Brovelli, "Three-dimensional imaging of dislocation dynamics during the hydriding phase transformation," *Nature Materials*, vol. 16, no. 5, p. 565, 2017.

[138] A. Singer, A. Ulvestad, H.-M. Cho, J. W. Kim, J. Maser, R. Harder, Y. S. Meng, and O. G. Shpyrko, "Nonequilibrium Structural Dynamics of Nanoparticles in LiNi1/2Mn3/2O4 Cathode under Operando Conditions," *Nano Letters*, vol. 14, pp. 5295–5300, Sep 2014.

[139] M. Leitner, B. Sepiol, L.-M. Stadler, B. Pfau, and G. Vogl, "Atomic diffusion studied with coherent X-rays.," *Nature Materials*, vol. 8, no. 9, pp. 717–20, 2009.

[140] R. Kukreja, N. Hua, J. Ruby, A. Barbour, W. Hu, C. Mazzoli, S. Wilkins, E. E. Fullerton, and O. G. Shpyrko, “Orbital domain dynamics in magnetite below the verwey transition,” *Physical Review Letters*, vol. 121, p. 177601, Oct 2018.

[141] A. M. Leguy, J. M. Frost, A. P. McMahon, V. G. Sakai, W. Kochelmann, C. Law, X. Li, F. Foglia, A. Walsh, B. C. O’Regan, J. Nelson, J. T. Cabral, and P. R.F. Barnes, “The dynamics of methylammonium ions in hybrid organic-inorganic perovskite solar cells,” *Nature Communications*, vol. 6, 2015.

[142] B. R. Sutherland, A. K. Johnston, A. H. Ip, J. Xu, V. Adinolfi, P. Kanjanaboos, and E. H. Sargent, “Sensitive, fast, and stable perovskite photodetectors exploiting interface engineering,” *ACS Photonics*, vol. 2, no. 8, pp. 1117–1123, 2015.

[143] W. S. Yang, J. H. Noh, N. J. Jeon, Y. C. Kim, S. Ryu, J. Seo, and S. I. Seok, “High-performance photovoltaic perovskite layers fabricated through intramolecular exchange,” *Science*, vol. 348, no. 6240, pp. 1234–1237, 2015.

[144] S. Baroni, S. De Gironcoli, A. Dal Corso, and P. Giannozzi, “Phonons and related crystal properties from density-functional perturbation theory,” *Reviews of Modern Physics*, vol. 73, no. 2, p. 515, 2001.

[145] X. Gonze and C. Lee, “Dynamical matrices, born effective charges, dielectric permittivity tensors, and interatomic force constants from density-functional perturbation theory,” *Physical Review B*, vol. 55, no. 16, p. 10355, 1997.

[146] G. Kresse and J. Furthmüller, “Efficient iterative schemes for ab initio total-energy calculations using a plane-wave basis set,” *Physical Review B*, vol. 54, no. 16, p. 11169, 1996.

[147] J. P. Perdew, A. Ruzsinszky, G. I. Csonka, O. A. Vydrov, G. E. Scuseria, L. A. Constantin, X. Zhou, and K. Burke, “Restoring the density-gradient expansion for exchange in solids and surfaces,” *Physical Review Letters*, vol. 100, no. 13, p. 136406, 2008.

[148] S. K. Sinha and D. K. Ross, “Self-consistent density response function method for dynamics of light interstitials in crystals,” *Physica B+C*, vol. 149, no. 1-3, pp. 51–56, 1988.

[149] E. M. Mozur, A. E. Maughan, Y. Cheng, A. Huq, N. Jalarvo, L. L. Daemen, and J. R. Neilson, “Orientational Glass Formation in Substituted Hybrid Perovskites,” *Chemistry of Materials*, vol. 29, no. 23, pp. 10168–10177, 2017.

[150] R. L. Sacci, M. L. Lehmann, S. O. Diallo, Y. Q. Cheng, L. L. Daemen, J. F. Browning, M. Doucet, N. J. Dudney, and G. M. Veith, “Lithium Transport in an Amorphous LixSi Anode Investigated by Quasi-elastic Neutron Scattering,” *Journal of Physical Chemistry C*, vol. 121, no. 21, pp. 11083–11088, 2017.

[151] Z. Wu, Y. Cheng, F. Tao, L. Daemen, G. S. Foo, L. Nguyen, X. Zhang, A. Beste, and A. J. Ramirez-Cuesta, "Direct Neutron Spectroscopy Observation of Cerium Hydride Species on a Cerium Oxide Catalyst," *Journal of the American Chemical Society*, vol. 139, no. 28, pp. 9721–9727, 2017.

[152] X. Han, H. G. Godfrey, L. Briggs, A. J. Davies, Y. Cheng, L. L. Daemen, A. M. Sheveleva, F. Tuna, E. J. McInnes, J. Sun, C. Drathen, M. W. George, A. J. Ramirez-Cuesta, K. M. Thomas, S. Yang, and M. Schröder, "Reversible adsorption of nitrogen dioxide within a robust porous metal–organic framework," *Nature Materials*, vol. 17, no. 8, pp. 691–696, 2018.

[153] H. Zhang, X. Qiao, Y. Shen, T. Moehl, S. M. Zakeeruddin, M. Grätzel, and M. Wang, "Photovoltaic behaviour of lead methylammonium triiodide perovskite solar cells down to 80 K," *Journal of Materials Chemistry A*, vol. 3, no. 22, pp. 11762–11767, 2015.

[154] J. M. Frost and A. Walsh, "What is moving in hybrid halide perovskite solar cells?," *Accounts of Chemical Research*, pp. 1–29, Feb 2016.

[155] Y. Yuan, J. Chae, Y. Shao, Q. Wang, Z. Xiao, A. Centrone, and J. Huang, "Photovoltaic Switching Mechanism in Lateral Structure Hybrid Perovskite Solar Cells," *Advanced Energy Materials*, vol. 5, no. 15, pp. 1–7, 2015.

[156] D. A. Egger, L. Kronik, and A. M. Rappe, "Theory of hydrogen migration in organic-inorganic halide perovskites," *Angewandte Chemie International Edition*, vol. 54, pp. 12437–12441, June 2015.

[157] D. A. Egger, A. M. Rappe, and L. Kronik, "Hybrid Organic-Inorganic Perovskites on the Move.," *Accounts of Chemical Research*, vol. 49, pp. 573–581, Feb 2016.